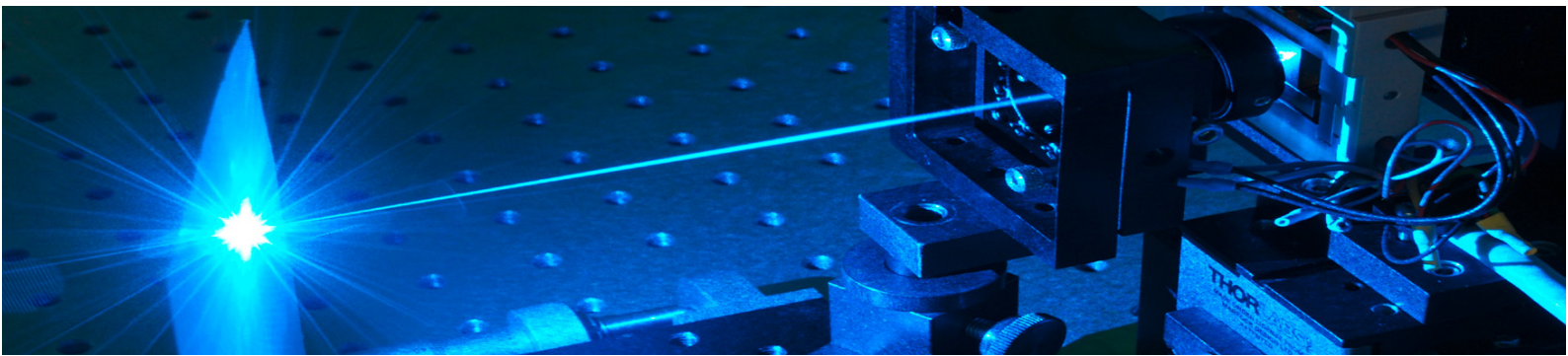# Universität Potsdam

Andreas Jechow

Tailoring the emission of stripe-array diode lasers with external cavities to enable nonlinear frequency conversion

Universitätsverlag Potsdam

Tailoring the emission of stripe-array diode lasers with external cavities
to enable nonlinear frequency conversion

Andreas Jechow

Tailoring the emission of stripe-array diode lasers with external cavities to enable nonlinear frequency conversion

University of Potsdam

Institute of Physics and Astronomy, Photonics Department

Tailoring the emission of stripe-array diode lasers with external cavities to enable nonlinear frequency conversion

Dissertation

zur Erlangung des akademischen Grades

Doktor der Naturwissenschaften

(*doctor rerum naturalium*)

in der Wissenschaftsdisziplin Experimentalphysik

eingereicht an der

Mathematisch-Naturwissenschaftlichen Fakultät

der Universität Potsdam

von Andreas Jechow,

geboren am 28. Januar 1978 in Wolfen.

Potsdam, 03. September 2009

In physics, you don't have to go around making trouble for yourself - nature does it for you.

(Frank Wilczek)

Contents

Chapter 1

Introduction

The invention of the laser in 1960 [1] had a huge impact on science and technology. Since then, new lasers are the driving force for the creation of many unimagined inventions. Two years after the demonstration of the first laser using ruby as active material, coherent emission from semiconductor material was realized [2]. Today, edge emitting diode lasers belong to the most efficient coherent light sources with electro-optical efficiencies of more than 70% [3]. They are ubiquitous in everyday life as we face them e.g. in CD players, printers, displays and product scanners. However, despite the advances made in band gap engineering and manufacturing technologies, diode lasers still face several limitations:

Transversal multi-mode operation: The diffraction-limited output power from a (narrow stripe) diode laser is limited to a few hundred milliwatts. Higher powers can be realized by extending the emitter to a width of 50 μm to 1000 μm to form a broad area (BA) diode laser. BA single emitter diode lasers yield continuous wave (cw) emission with output powers of more than 10 W [4]. Combined in arrays (laser bars) these devices are capable of producing radiation with several hundred Watts of output power [5], while the power level can be increased to several kilowatts by stacking multiple laser bars [6]. The main drawback of a BA diode lasers is the poor spatial beam quality in the direction where the emitter is broad, because transversal multi-mode operation will occur due to the lack of waveguiding.

A second way for power scaling is manufacturing arrays of narrow stripe diode lasers, so called coupled "stripe-arrays". If the emitters are realized in close proximity, coupling between adjacent stripes will occur leading to a global coupling between all emitters. However, the stripe-arrays showed a strong double lobed emission in the far-field, which caused poor beam quality and thus made them unattractive for most applications.

Several approaches to achieve high power emission with improved beam quality from BA and stripe-array diode lasers exist. Off-axis external cavities with mirrors, gratings or phase conjugation [7–10] and injection locking with a master laser [11] were demonstrated.

Longitudinal multi-mode operation: Another drawback of edge emitting diode lasers is longitudinal multimode operation which is owed to the lack of wavelength selectivity of the Fabry-Perot cavity. Thus, the spectral width of the emission of such a diode laser is relatively broad (typically > 1 nm for BA diode lasers). This can be overcome by integrating Bragg reflectors into the laser diode chip, or by setting up an external cavity with wavelength selective elements like diffraction gratings.

Spectral range: Emission from edge emitting diode lasers is available from the ultraviolet to the blue spectral range (from 365 nm to 480 nm) and from the red to the mid infrared spectral range (from 630 nm to 2600 nm) [12, 13]. High power, high brightness devices are only available from 790 nm to 1150 nm. In the visible spectral range from the aquamarine to the red (from 481 nm to 630 nm) [14], a lack of emitters capable to produce efficient radiation exists. Although pulsed operation in the green spectrum [15] has been demonstrated very recently, these diode lasers are still under development and show very low efficiencies.

However, a vast number of applications like medical treatment and diagnostics, spectroscopy, data storage, and display technology demand laser emission within the visible wavelength range. Gas lasers, like the Argon ion laser, show strong emission lines in the blue-green spectral range. But these devices are rather bulky, show short service intervals and suffer from low efficiencies. Thus, a strong need for compact blue-green laser devices exists [16], which motivated this work.

Thesis outline

Frequency conversion like second harmonic generation (SHG) is one technique to generate coherent radiation in wavelength ranges where lasers are not readily available. To achieve efficient frequency conversion in a nonlinear crystal, high intensities are required. Furthermore, the necessary phase-matching demands for narrow bandwidth emission. Although periodically poled materials that enable efficient frequency conversion at moderate pump powers have become broadly available, the key requirements for the pump lasers remain high power emission in combination with high spectral purity and good spatial mode quality.

The primary objective of this dissertation is to realize radiation with such a high brilliance in the near infrared spectral range by utilizing BA or stripe-array diode lasers. To realize the requirements for SHG the diode lasers have to be anti-reflection (AR) coated to realize an amplifier that can be stabilized in an external cavity. Thus, the transversal and longitudinal emission characteristics of such BA and stripe-array amplifiers have to be investigated. The parameters of high-power, stable single-longitudinal and fundamental-transversal operation have to be separated step by step theoretically and experimentally. The external cavity has to be designed appropriately following these investigations.

The second goal of this work is to utilize this external cavity diode laser (ECDL) for efficient frequency doubling to the blue spectral range with periodically poled materials.

This thesis is split into two major parts and structured as follows:

The first part of this thesis describes the strategies to achieve emission with high brilliance from external cavity enhanced BA and stripe-array amplifiers. The second part of this thesis reports on efficient frequency conversion of diode laser emission utilizing periodically poled materials.

In chapter 2, the fundamentals of high power diode lasers are discussed briefly. The theoretical framework to understand the physics of the coupled stripe-array used in this work is given in chapter 3. Numerical simulations have been made as the basis for the design of the external cavity. Transversal mode selection with off-axis external cavities is investigated in chapter 4. Wavelength stabilization and bandwidth narrowing is investigated in chapter 5. As a result, an off-axis stripe-array ECDL is developed that fulfills the requirements for nonlinear applications.

Chapter 6 gives a brief overview of the foundations of second harmonic generation. In

chapter 7, the results of single pass frequency doubling the emission of the off-axis stripe-array ECDL developed in the first part of this thesis are presented. As a benchmark for the performance of this off-axis stripe-array ECDL, two other state of the art diode laser systems have been investigated.

To demonstrate the improvement of the emission quality that is made by stabilizing the stripe-array amplifier in the off-axis external cavity, another application of this device is presented in chapter 8: a tunable all-solid-state biphoton source that provides a record number of generated biphotons per second. The source was explicitly designed for quantum spectroscopy.

Finally, the work is summarized and future ideas are presented in chapter 9.

Part I

High brilliance emission from external cavity diode lasers

Chapter 2

High brilliance emission from diode lasers

Edge emitting diode lasers based on gallium arsenide (GaAs) are key elements for modern laser technology. These compact devices reach outstanding electro-optical efficiencies, high reliability and high output powers. In edge emitters, a Fabry-Perot resonator is formed between the cleaved facets of the semiconductor chip. This manufacturing step is simple, cost effective and can be performed with a high precision. Unfortunately, the low mode selectivity of the Fabry-Perot resonator results in longitudinal and transversal multimode operation.

However, in the last few years the demand for efficient diode laser emission with good transversal beam quality and narrow spectral emission has increased. Thus, new chip and resonator designs have been developed to solve these problems and modern GaAs based diode lasers can produce radiation with high brightness and brilliance, respectively. These developments were mainly driven by spectroscopic applications but have opened the door for diode lasers to be used for nonlinear frequency conversion.

In this chapter, the fundamentals of edge emitting diode lasers with the emphasis on obtaining high power, high brightness and high brilliance emission will be presented.

2.1   Brightness and brilliance

The Gaussian beam is the fundamental transversal eigensolution of the field equation of a propagating electromagnetic wave in paraxial approximation. The shape of a Gaussian beam will remain constant during propagation, just the width and the peak intensity will change. A perfectly Gaussian shaped beam as depicted in Fig. 2.1 is characterized by the beam waist radius w_0, the half far-field angle θ_0 and the wavelength λ. The beam waist radius is defined as the width at the $1/e^2$ value of the peak intensity I_0. If the Gaussian beam is assumed to propagate along the z-axis, one can obtain the beam waist radius at any z-position:

$$w(z) = w_0 \cdot \sqrt{\left(1 + \frac{z}{z_{\mathrm{R}}}\right)^2},$$
(2.1)

with the Rayleigh length z_{R}. The Rayleigh length is defined as the distance from the beam waist position z_0 where the waist radius has increased by a factor of $\sqrt{2}$, $w(z_{\mathrm{R}}) = \sqrt{2} \cdot w_0$. It reads:

$$z_{\mathrm{R}} = \frac{w_0^2 \cdot \pi}{\lambda}.$$
(2.2)
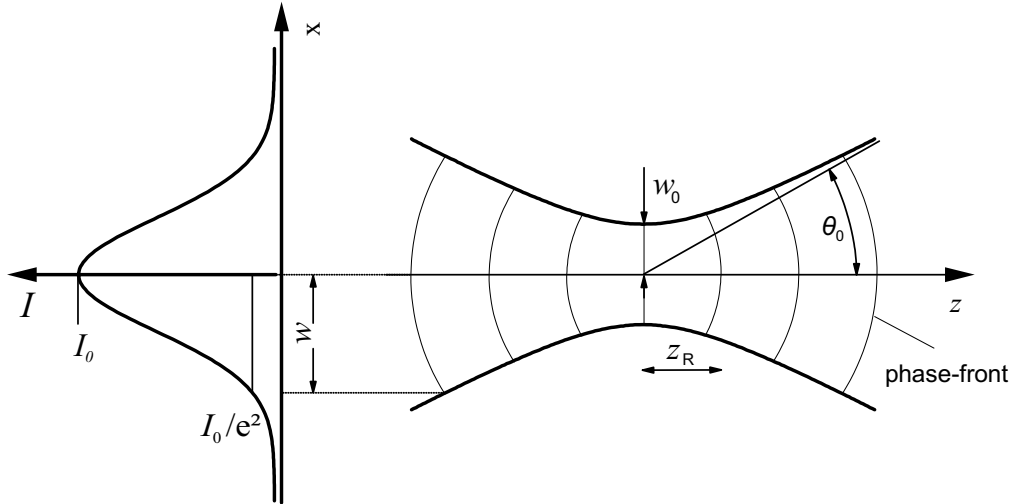
Figure 2.1: Intensity profile and caustic of a Gaussian beam with the beam waist radius w_0.

The divergence angle in the far-field can be calculated for $z \gg z_R$ as:

$$\theta = \lim_{z \to \infty} \frac{w(z)}{z} = \frac{w_0}{z_R} = \frac{\lambda}{\pi \cdot w_0}. \tag{2.3}$$

The beam parameter product *BPP* of an ideal Gaussian beam is the product of the half of the opening angle of the beam θ_0 and the beam radius w_0:

$$BPP = \theta_0 \cdot w_0 = \frac{\lambda}{\pi}. \tag{2.4}$$

The *BPP* remains constant when a laser beam propagates in free space and through media without phase-distortions. Thus, the minimum focus of a Gaussian shaped laser beam is physically limited by the wavelength. An ideal Gaussian beam is also called "diffraction-limited".

For "non-diffraction-limited" laser beams, the beam propagation factor M^2 is introduced. The factor M^2 describes how much a real laser beam deviates from the diffraction limit. It is defined as:

$$\theta_{\text{real}} \cdot w_{\text{real}} = M^2 \cdot \theta_0 \cdot w_0, \tag{2.5}$$

with θ_{real} and w_{real} being the measured beam parameters. Since this is only a one dimensional solution and a propagating laser beam is typically treated as a two dimensional problem, the effective two dimensional beam quality is defined as:

$$M^4 = M_x^2 \cdot M_y^2. \tag{2.6}$$

For non diffraction-limited beams it is very important to have a conclusive definition of the beam waist radius w_0, since the $1/e^2$ method is not suitable. The ISO standard [17] defines w_0 using the second order moments of the intensity distributions. In this work all beam quality measurements are conform with this standard.

In laser technology, the brightness B is defined as the intensity in the focus that is emitted per unit solid angle Ω. With the intensity being the power P emitted per area A the brightness can be calculated using this equation:

$$B = \frac{P}{A \cdot \Omega}. \tag{2.7}$$

For the brightness B_{DL} of a diffraction-limited laser beam in paraxial approximation follows:

$$B_{\mathrm{DL}} = \frac{P}{w_0^2 \cdot \theta_0^2 \cdot \pi^2} = \frac{P}{\lambda^2}. \tag{2.8}$$

For non diffraction-limited beams the brightness B_{NDL} depends inversely proportional on the beam parameter product M^4:

$$B_{\mathrm{NDL}} = \frac{P}{M^4 \cdot \lambda^2}. \tag{2.9}$$

The term brilliance BR is used for the so called spectral brightness or radiance which is the brightness per unit wavelength (or bandwidth):

$$BR = \frac{P}{M^4 \cdot \lambda^2 \cdot \Delta\lambda}. \tag{2.10}$$

2.2 Fundamentals of diode lasers

2.2.1 p-n junction and p-i-n double-heterostructure

The optical gain inside the semiconductor material is provided by radiative recombination between electrons and holes. This can be realized with a p-n junction, a p-i-n double-heterostructure or a quantum well.

If a p-n junction is in thermal equilibrium the Fermi-energies of both materials are at the same Fermi-level. If a biased current is injected, the Fermi levels $E_{F,V}$ of the valence band and $E_{F,C}$ of the conduction band are split into two separate levels. The inversion necessary for stimulated emission is reached with the presence of holes in the valence and electrons in the conduction band in the junction. Thus, amplification of radiation with the wavelength λ corresponding to a photon energy between the direct band gap energy E_G and the energy difference between the two Fermi-energies will occur:

$$E_G \leq h \cdot \frac{c}{\lambda} \leq E_{F,C} - E_{F,V}, \tag{2.11}$$

whereas h is the Planck constant and c is the speed of light. Laser emission from a p-n junction was first demonstrated in 1962 [2]. Later, double-hetero and quantum well structures were realized to achieve lower threshold current densities.
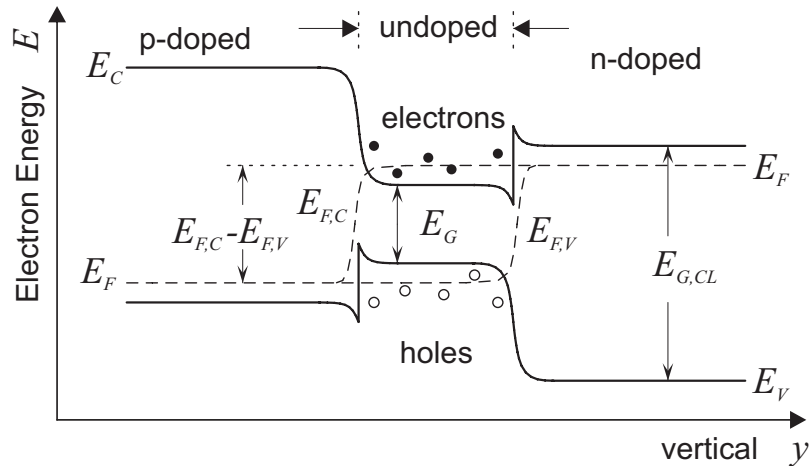
Figure 2.2: Forward-biased double-heterostructure p-i-n junction [18].

A forward biased double-hetero p-i-n structure, where an undoped (intrinsic) semiconductor with a direct band-gap is sandwiched between p- and n-doped materials with higher band-gaps is depicted in Fig. 2.2. When a forward biased current J is injected, the quasi-Fermi levels $E_{F,C}$ and $E_{F,V}$ in the intrinsic layer are located inside the conduction and valence bands. Thus, inversion is present in this region and optical radiation can be amplified by stimulated emission. This structure has two more advantages compared to the p-n junction. The charge-carriers (electrons and holes) are confined inside the intrinsic layer because of the barriers in the conduction and the valence band. Furthermore, an optical waveguide is realized because for most semiconductor-material systems, the material with the low band-gap exhibits a higher refractive index compared to the surrounding highly doped material with a higher band-gap ($E_{G,CL}$).

2.2.2 Fabry-Perot diode laser

In an edge emitting diode laser, the resonator is formed between the two parallel cleaved facets of the semiconductor chip. The index step between the semiconductor material and air results in a reflectivity of approximately 30%. Thus, the back facet of the diode laser is typically highly reflective coated, while the front facet remains uncoated or has to be anti-reflection (AR) coated to reach a few percent reflectivity.

The scheme of a standard diode laser with a Fabry-Perot resonator and its typical transversal emission characteristic is depicted in Fig. 2.3. The vertical direction (y) is called the "fast-axis" and the lateral direction (x) is called the "slow-axis". Typically, the far-field emission angle in slow-axis direction is lower because the emitter is broader. The z-direction is the light propagation direction.

Below threshold the semiconductor material will absorb a propagating wave and the intensity will read:

$$I(z) = I_0 \exp(-\alpha \cdot z), \tag{2.12}$$

with the initial intensity I_0 and the absorption coefficient α. The optical gain at threshold is given by $g_{th} = -\alpha$. By injecting more carriers, stimulated emission will overcompensate the absorption losses and lasing will start.

For a Fabry-Perot resonator with two mirrors with reflectivities R_F at the front facet and R_B at the back facet, the threshold condition will become:

$$g_{\text{modal}} = \Gamma \cdot g(J_{th}) = \alpha_i + \alpha_m, \tag{2.13}$$
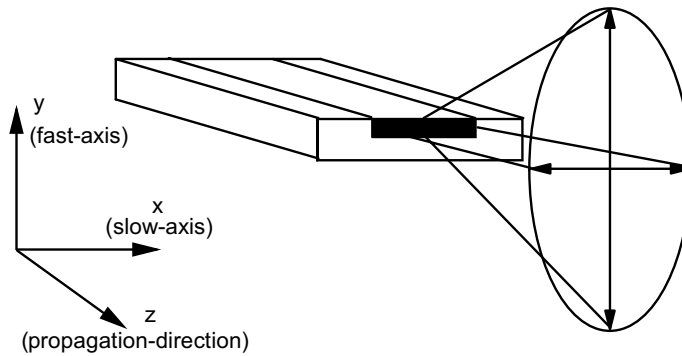
Figure 2.3: Typical emission characteristic of a Fabry-Perot diode laser. The vertical axis (y) with the higher divergence is called fast-axis. The lateral direction (x) with the smaller divergence angle is called the slow-axis.

with the threshold current J_{th} the modal gain g_{modal}, the internal losses α_i, the mirror losses α_m and the confinement factor Γ. The mirror losses are given by:

$$\alpha_m = \frac{1}{2L} \ln \left(\frac{1}{R_F \cdot R_B} \right), \qquad (2.14)$$

with L being the resonator length. The confinement factor is defined as the overlap of the optical mode with the gain:

$$\Gamma = \frac{\int\limits_{-h/2}^{+h/2} J(y) dy}{\int\limits_{-\infty}^{+\infty} J(y) dy}, \qquad (2.15)$$

whereas h is the thickness of the active region.

An important parameter for high power diode lasers is the shift of the laser threshold current with temperature, which can be described by the following exponential relation:

$$J_{th2} = J_{th1} \exp \left(\frac{T_2 - T_1}{T_0} \right), \qquad (2.16)$$

whereas J_{th1} is the threshold current at an ambient temperature T_1, J_{th2} is the threshold current at an ambient temperature T_2 and T_0 is a characteristic temperature. The higher the characteristic temperature, the more stable is the operation of the diode laser at higher ambient temperature. A typical value at an emission wavelength of 980 nm is $T_0 = 200$ K.

The waveguide of such a Fabry-Perot diode laser can be approximated by a slab. The amplitude of the electric-field vector $\mathbf{E}(x, y, z)$ of the light propagating inside a slab dielectric material with a refractive index $n(x, y, z)$ can be derived using the Helmholtz equation:

$$\Delta \mathbf{E}(x, y, z) + k_0^2 n^2(x, y, z) \mathbf{E}(x, y, z) = 0, \qquad (2.17)$$

with $k_0 = 2\pi/\lambda$ and λ is the wavelength of the light in vacuum.

The field distribution $\mathbf{E}(x, y)$ at the laser facet is the near-field distribution. The far-field intensity pattern $I(\theta_x, \theta_y)$ can be derived using the Fresnel-Kirchhoff diffraction integral. In one dimension this reads:

$$I(\theta_x) \propto \cos^2 \theta_x \left| \int\limits_{-\infty}^{+\infty} \mathbf{E}(x) \exp(ik_0 \sin \theta_x x) dx \right|^2,$$

$$I(\theta_y) \propto \cos^2 \theta_y \left| \int\limits_{-\infty}^{+\infty} \mathbf{E}(y) \exp(ik_0 \sin \theta_y y) dy \right|^2. \qquad (2.18)$$

2.2.3 Optical confinement

Two cases of optical confinement can be distinguished as depicted in Fig. 2.4: (a) Index guiding and (b) gain guiding.

Index guiding: In an index guiding structure a step index of the refractive index n is realized. The optical waveguide is formed by a material with a higher refractive index n_{WG} that is surrounded by a cladding material with a lower refractive index n_{CL}. Such a step index can also be realized with air as surrounding material. Thus, index guided lateral structures can be manufactured by etching a ridge waveguide, where the p-side cladding and partly the waveguide layer is removed except for a ridge of a few μm width.
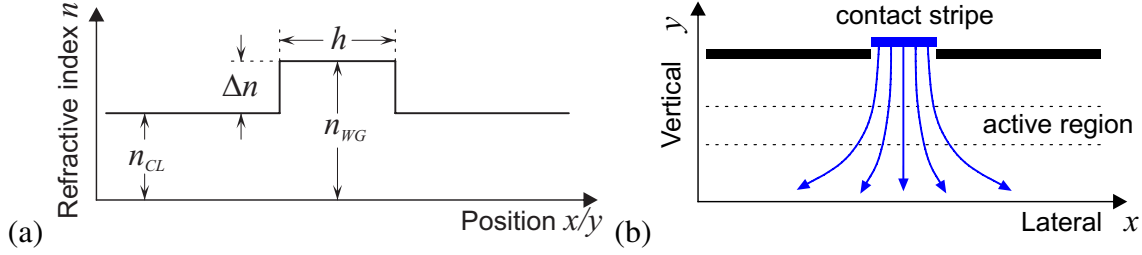
Figure 2.4: Optical confinement (a) index guiding and (b) gain guiding [18].

Gain guiding: In a gain guided structure, the refractive index of the material without the presence of carriers is homogeneous. Carriers are only injected in a narrow region of the active region through a contact stripe, while the active layer expands over the whole width of the device. The electrical contact stripes can either be applied by etching through an isolator layer before metalization or by ion implantation.

If the injection current is increased, the refractive index changes due to the free carrier plasma effect and Joule heating in the active layer. The carrier induced change in the refractive index Δn_C due to the free carrier plasma effect is proportional to the injected carrier concentration N_C [19]:

$$\Delta n_C = \frac{e^2}{2 m_C \cdot \omega^2 \cdot \varepsilon_0 \cdot n} N_C, \tag{2.19}$$

whereas $e = 1.602 \cdot 10^{-19} As$ is the elementary charge, $m_C = 9.109 \cdot 10^{-31} kg$ is the effective mass of the free carriers, ω is the angular frequency of light, $\varepsilon_0 = 8.854 \cdot 10^{-12} As/Vm$ is the permittivity in vacuum, and n is the refractive index without the injection of carriers. Considering a typical carrier concentration of $N_C = 10^{18}$ cm^{-3}, the refractive index will decrease on the order of 10^{-3}. Thus, the light is not completely confined to the active layer and is radiated to the surrounding regions, which is called the "antiguiding" effect (see next chapter).

However, if the injection current is increased the active layer will be heated by Joule heating. Thus, the temperature in the injection region will rise as well. This will result in a temperature induced refractive index change Δn_T given by [19]:

$$\Delta n_T \approx 5 \cdot 10^{-4} \cdot \Delta T, \tag{2.20}$$

with ΔT being the increase in the temperature of the injection region in units of Kelvin. The resulting increase in the refractive index due to Joule heating of the active layer will result in a positive index step similar to an index guided structure.

Since both refractive index changing effects are opposed to each other, pure gain guiding will only occur very close to the laser threshold. Strictly speaking, neither gain nor index guiding alone are usually realized in a real-world device. However, one of the two possible confinement mechanisms can play the major role for a specific diode laser device.

2.3   Design considerations for power scaling

Typically, the emitting area of a narrow stripe single element diode laser has a width of 3 μm and a height of < 1 μm. At cw emission with output powers in the range of a few hundred milliwatts this will result in power densities of 3-10 MW/cm^2, which is very close to the damage threshold of the semiconductor material and coatings. Furthermore, absorption at

the diode laser facets can occur. The absorption can cause heating of the device that might lead to catastrophic optical mirror damage, which is still one of the main issues limiting the output powers achievable with high power diode lasers [20].

Several solutions to overcome facet damage exist, but the most crucial aspect for diode laser degradation and device failure remains the power density at the facet [21]. The increase of the emitting area is one way to reduce the power density at the facet and to achieve more output power from a single element diode laser.

2.3.1 Vertical layer design

Today, high power semiconductor lasers feature a thin quantum well with a few nanometers thickness (typical values are 7-15 nm) surrounded by a material with a higher band-gap. The band-gap difference has to be larger than 100 meV to avoid carrier leakage. The use of a thin quantum well has the advantage that only a small region is pumped. Furthermore, the emission wavelength can be adjusted by using strained compositions with a moderate lattice mismatch between waveguide and quantum well.

Depending on the strain of the quantum well, the diode laser emission will be polarized in different axes. For tensile strain the emission will be polarized in the transverse-magnetic (TM) direction, meaning that the magnetic component of the electromagnetic field will oscillate in fast-axis direction. Transverse-electric (TE) polarization, where the electric component of the field oscillates in slow-axis direction, will be present if compressively strained structures are used. In the near infrared wavelength region ranging from 880 nm to 1150 nm, compressively strained indium gallium arsenide (InGaAs) quantum wells embedded in an aluminum gallium arsenide (AlGaAs) waveguide layer are used. All diode laser chips investigated in this work are InGaAs quantum well structures.

A way to minimize the facet load and to reduce the far-field angle is to enlarge the emitting area in vertical direction. So called large optical cavities [22], super large optical cavities [23] and asymmetric super large optical cavities [24] have been fabricated with waveguide thicknesses of up to 8.5 μm [25]. Although the waveguide is multimode in principle, only the fundamental mode will be amplified because higher modes are sup-
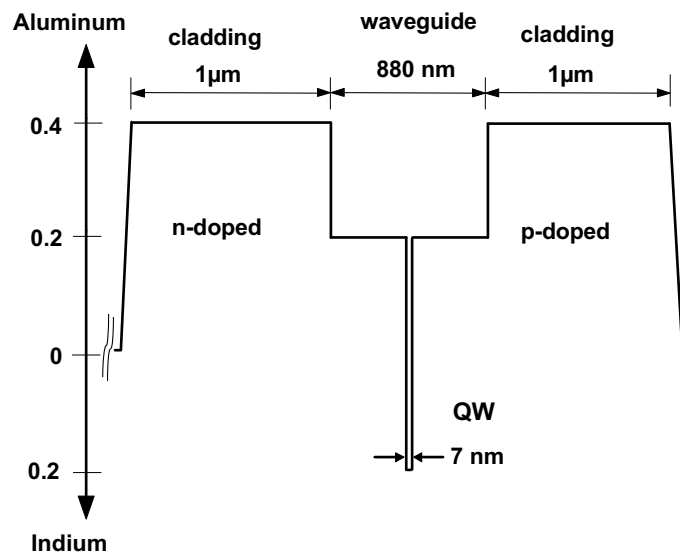
Figure 2.5: Epitaxial layer structure of the stripe-array with a large optical cavity.

pressed due to higher losses. This can be achieved by carefully adjusting the cladding layer thickness.

Figure 2.5 shows the vertical layer design of the stripe-array used in this work with a large optical cavity structure. The active region consists of a single InGaAs quantum well embedded in a 880 nm thick AlGaAs core region. The quantum well is 7 nm thick with an indium content of 20%. The optical waveguide is formed by 1 μm thick AlGaAs claddings with 40% Al. The GaAs cap layer is heavily p-doped ($6 \cdot 10^{19}$ cm^{-3}) in order to reduce the contact resistance [22].

2.3.2 Lateral chip design

Another approach to achieve higher output powers from a single diode laser element without damaging the semiconductor material or the facets, is extending the device in lateral direction. The three most widespread lateral chip designs for diode lasers are depicted schematically in Fig. 2.6.
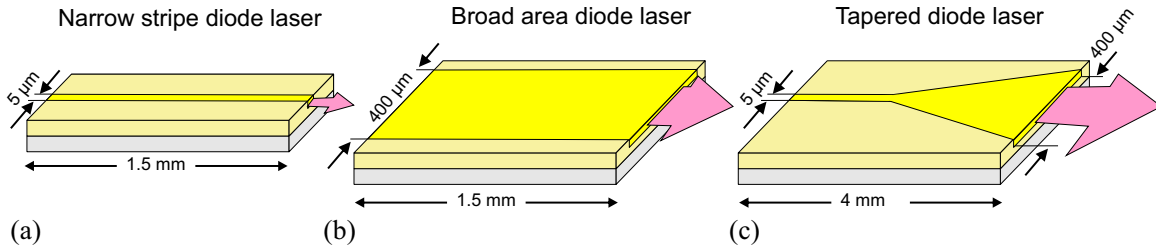
Figure 2.6: Sketch of the lateral structure of (a) a narrow stripe diode laser, (b) a broad area diode laser and (c) a tapered diode laser.

Narrow stripe diode lasers: Narrow stripe single emitter diode lasers typically emit a nearly diffraction-limited beam in both directions. A schematic drawing of such a device along the slow-axis is depicted in Fig. 2.6 (a). This results in a circular, nearly Gaussian intensity distribution and low astigmatism. Nowadays, narrow stripe diode lasers are mostly realized by index guiding. Such ridge waveguide diode laser have widths between 3 and 5 μm and are capable of delivering several hundred milliwatts of diffraction-limited light with low ellipticity and astigmatism. Recently, a ridge waveguide diode laser with a 4.8 μm thick vertical asymmetric super large optical cavity structure and a 5 μm wide ridge was demonstrated. This device was capable to produce nearly diffraction-limited emission ($M^2 < 1.3$ in both axes) with optical output powers of 1.5 W at an emission wavelength of 980 nm [26].

Broad area (BA) diode lasers: BA diode lasers are broadened in the lateral direction, as depicted in Fig. 2.6 (b). Typically, BA diode lasers have widths between 50 μm and 1000 μm. Output powers of more than 15 W in combination with high reliability have become feasible with emitters in the 100 μm range [4]. Most commonly, in fast-axis direction a narrow waveguide ($\approx 1 - 3\mu$m) is realized by index-guiding. Thus, in fast-axis direction a near diffraction-limited beam with a far-field angle in the range of $\approx 30°$ is emitted. This makes aspherical cylindrical lenses with high numerical apertures of up to NA = 0.8 necessary. Such a lens is called fast-axis collimator (FAC).

The far-field distribution of the emission along the slow-axis consists of the superposition of the several transversal modes that can arise because of the broadened waveguide. The emission angle of $\approx 12°$ is significantly smaller than in fast-axis direction. Thus, the resulting beam profile emitted by a standard BA diode laser shows a strong ellipticity and astigmatism. The enlargement of the emitter has a severe impact on the lateral beam quality. For example, the beam propagation factor of a 100 μm emitter is in the range of $M_x^2 \approx 30$ ($M_x^2 \approx 60$ for a 400 μm wide emitter). Although single element BA devices with stripe widths up to 1000 μm have been reported [27], the output powers could not be improved significantly. Rather, a strong filamentation that results in a non homogeneous intensity distribution at the diode laser facet was observed. Because of these "hot spots", the on-set of catastrophic optical mirror damage does not scale linearly with the emitter width. Furthermore, the filamentation is a reason that the slow-axis far-field of a BA diode laser does not have the highest intensity along the optical axis. Rather, a double lobe emission with two high intensity peaks "off-axis" was observed. Nonlinear and chaotic behavior like self-pulsation and self-focusing are other possible consequences of the beam filamentation [28, 29].

Tapered diode lasers: To overcome the drawbacks of the BA devices and realize high output powers without damaging of the facet, tapered amplifiers and tapered diode lasers have been suggested [30, 31].

Today, a tapered diode laser typically consists of an index-guided ridge waveguide and a gain-guided tapered amplifier section. This is schematically drawn in Fig. 2.6 (c). To avoid leakage of stray light from the taper into the ridge section, additional grooves can be etched as reflectors. Typical values for the tapered angle are $4 - 6°$. The tapered section is typically $2 - 4$ mm, the ridge section $0.3 - 1$ mm long resulting in overall chip lengths of $2.5 - 6$ mm.

The ratio between the length of the ridge and taper section is a critical parameter and has a severe impact on the lateral beam quality as well as the achievable output power. If the ridge section is too short, the spatial mode filtering of the oscillator is insufficient and the beam propagation factor of the whole device will become low. Furthermore, a short ridge will be more sensitive to optical feedback from the tapered section. At high injection currents saturation effects caused by an overload of the ridge section are observed.

On the other hand, a long ridge waveguide section can have too much power oscillating. This can induce self-focusing, filamentation and self-pulsation into the tapered region, especially at higher injection currents. These drawbacks can be avoided by separately contacting ridge and taper section. The disadvantage of this method is the increased heat conductivity, because the laser chips must be mounted p-side up on the heat sink to make the p-contacts separately accessible. However, with such p-side up mounted tapered devices emission with optical output powers of more than 6 W possessing a good beam quality ($M_x^2 \approx 2$) and showing narrow vertical and lateral far-field angles have been demonstrated [32].

Diode laser arrays

Besides increasing the emitter size, it is possible to arrange several emitters in a row to achieve power scaling as shown in Fig. 2.7. This was done with all three lateral diode lasers designs described above.

One can distinguish between arrays of uncoupled and coupled emitters, which mainly depends on the distance between the emitters. Most commonly, BA diode lasers are ar-

ranged in so called laser bars, where the emitters are not coupled as indicated in Fig. 2.7 (a). However, uncoupled arrays of narrow stripe and tapered diode laser have been manufactured and studied in the past, too.

If the emitters are manufactured very close to each other, as shown in Fig. 2.7 (b), coupling between the emitters of an array can occur. In this case, the array emission is characterized by an array "supermode" rather than the mode of an individual emitter.

Since the major part of this thesis is dedicated to the investigation of such coupled stripe-array diode lasers, a more detailed theoretical description of these devices can be found in the next chapter 3.
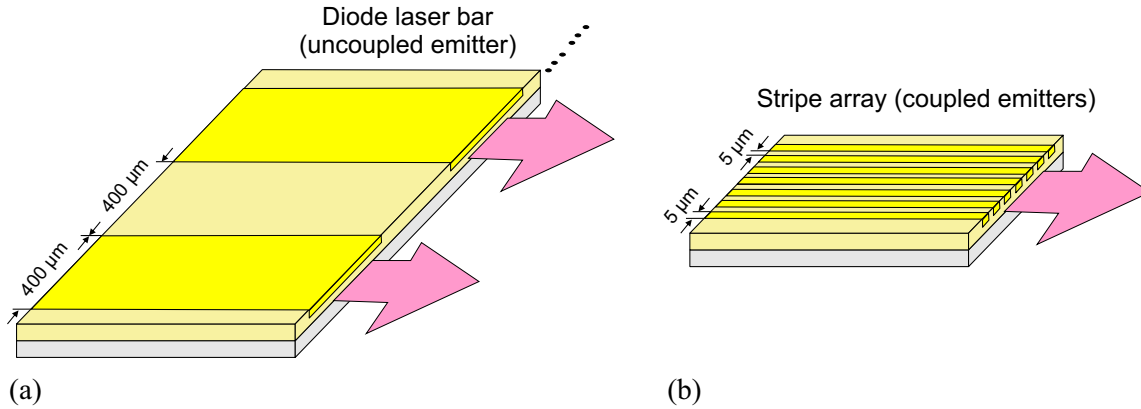
Figure 2.7: Diode laser arrays with (a) laser bar with uncoupled emitters and (b) stripe-array with coupled emitters.

2.4 Approaches to achieve narrow bandwidth emission

For nonlinear frequency conversion the pump light source has to meet the requirements for phase-matching. Therefore, a small bandwidth of emission and a high stability of the emission wavelength are necessary.

The fundamental limit for the laser linewidth resulting from the quantum noise was calculated by Schawlow and Townes even before the first laser was demonstrated. They introduced the Schawlow-Townes laser linewidth $\Delta\nu_{laser}$. For semiconductor lasers, this linewidth is increased by a factor of $(1 + \alpha_H^2)$, whereas α_H is the alpha or Henry - factor [33]. The Schawlow-Townes-Henry linewidth then reads:

$$\Delta\nu_{diode} = \frac{\pi \cdot h\nu \left(\Delta\nu_C\right)^2}{P} \left(1 + \alpha^2\right), \tag{2.21}$$

with the photon energy $h\nu$, the laser output power P and the cavity bandwidth $\Delta\nu_C$.

But, because of the broad spectral gain of the semiconductor material and the insufficient wavelength selectivity of the Fabry-Perot resonator, edge emitting diode lasers will typically show longitudinal multimode operation. The emission of such a device shows a spectral width of a few nanometers, far above the theoretical limits. Several approaches to realize frequency stabilization and a reduction of the bandwidth of diode laser emission exist. One can distinguish between the two main approaches: the use of external cavities that contain wavelength selective elements or integrating wavelength selective regions to the laser chip itself.

2.4.1 External cavity diode lasers

By building an external cavity with beam shaping optics and wavelength selective elements, it is possible to take influence on the longitudinal and transversal emission behavior of a diode laser. In most cases the external cavity is formed between one facet of the diode laser and a reflective element like an external mirror or a diffraction grating. Those devices are called external cavity diode lasers (ECDLs). To suppress the chips own longitudinal and transversal modes the other facet has to be typically highly AR coated.

Reflective diffraction gratings are used as frequency selective elements for the external stabilization of diode lasers. Most commonly, Littrow or Littman Metcalf type ECDLs are realized. The grating equation for the general case is given by $m \cdot \lambda = d_G \cdot (\sin \alpha \pm \sin \beta)$, with the groove distance d_G wavelength λ, the incident angle α, the diffraction angle β and the diffraction order m. For the Littrow configuration, the incident angle and the angle of the first order of diffraction are the same resulting in the following condition:

$$\sin \alpha_L = \lambda/d_G \cdot 2, \tag{2.22}$$

with the Littrow angle α_L.

The classic Littrow setup consisting of a diode laser with an AR-coated front facet and a HR coated back facet, a collimation lens and a diffraction grating is depicted in Fig. 2.8 (a). The first order of diffraction of the grating is reflected back onto itself and outcoupling is managed via the zero order of diffraction. By tilting the grating the emission wavelength of the diode laser can be tuned. A practical description of such an ECDL is given by Ricci et al. [34].
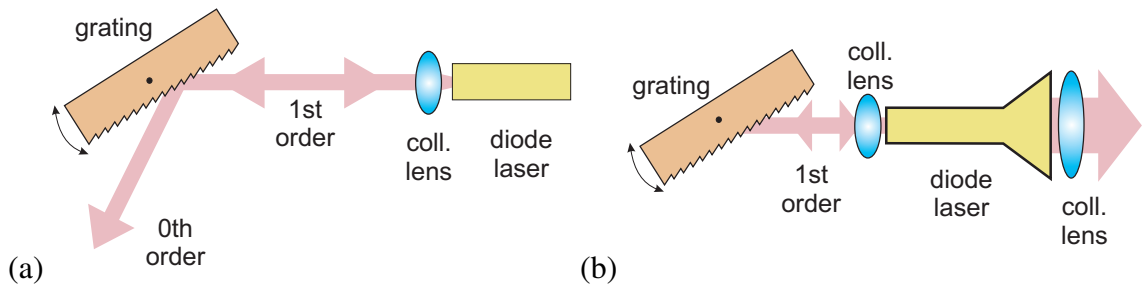
Figure 2.8: Littrow type external cavity diode lasers with reflective diffraction gratings, (a) standard and (b) rear setup.

The main disadvantage of the Littrow configuration is the beam displacement when the diode laser wavelength is tuned by tilting the grating. This lateral shift can be compensated by using an additional mirror parallel to the grating [35] or a triangular prism [36]. Moreover, a rear Littrow configuration as depicted in Fig. 2.8 (b) can be used. In this scheme, a
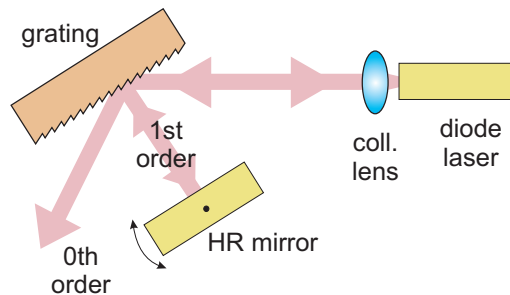
Figure 2.9: Littmann type external cavity diode lasers with a reflective diffraction gratings.

diode laser with a highly AR-coated back facet and a partly AR-coated front facet is used. The resonator is formed between the grating and the front facet of the diode laser.

The Littman-Metcalf setup is depicted in Fig. 2.9. The grating is fixed and the first order of diffraction is directed to a movable mirror where it is reflected back to the diode laser [37, 38]. Outcoupling is managed via the zeroth order of diffraction and the emission wavelength can be tuned by rotating the mirror. Although the Littman-Metcalf configuration has the higher wavelength selectivity because the grating diffracts the light twice per resonator roundtrip, the Littrow setup tends to show the smaller bandwidths in practice. The laser bandwidth of an ECDL system is mainly influenced by electronic and acoustic noise or mechanical vibrations. The simpler and more robust Littrow setup is less susceptible to those external influences.

2.4.2 Distributed feedback diode lasers

Besides the use of external gratings it is possible to achieve wavelength stabilization and tunability by monolithically integrated spectral filters directly to the diode laser chip. This is done by implementing an on chip Bragg grating close to the active region in order to stabilize and spectrally narrow the diode laser emission. The Bragg grating period Λ_{Bragg} is given by the grating order m, the refractive index n and the emission wavelength λ:

$$\Lambda_{\mathrm{Bragg}} = \frac{m \cdot \lambda}{2 \cdot n}.$$

In a distributed feedback (DFB) diode laser, the corrugated grating spans the whole length of the device. A DFB ridge waveguide diode laser is schematically depicted in Fig. 2.10 (a) [39, 40]. To suppress the Fabry-Perot modes of the laser chip, the front facet is AR-coated. Due to the long grating, spanning the whole width of the device, instabilities and mode hops are avoided. Furthermore, no separated contacts are necessary and the chip can be mounted p-side down for better heat removal. However, the grating of a DFB diode laser has to be buried to realize electrical contacting of the diode laser. Such a buried grating is depicted in Fig. 2.10 (b). Ridge waveguide DFB diode lasers can deliver several hundreds of mW of diffraction-limited output power with bandwidths in the MHz regime and side-mode suppression ratios exceeding 50 dB. In a recent work, more than 500 mW at a wavelength of 980 nm have been demonstrated [41].
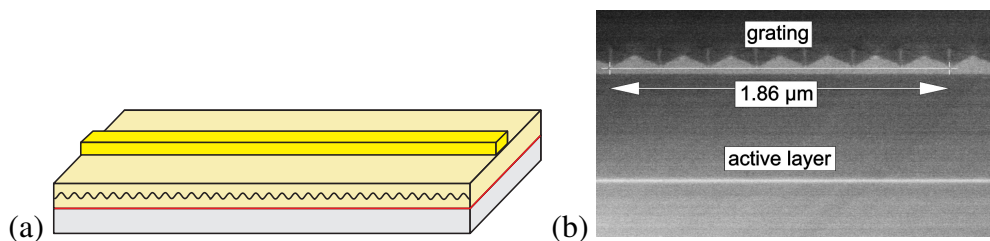
Figure 2.10: (a) Schematic drawing of a DFB diode laser. (b) On chip buried grating of a DFB diode laser. Right picture copyrighted by FBH [1]. Reprinted with the friendly permission of K. Paschke

---

[1]Ferdinand Braun Institut für Höchstfrequenztechnik, www.fbh-berlin.de

Chapter 3

Theoretical description and modeling of coupled diode laser arrays

The main part of this thesis is dedicated to the investigation of stripe-array diode lasers. Stripe-arrays are laterally coupled narrow stripe lasers with a resulting emitter width that is comparable to a BA diode laser. In subsection 2.3.2 a brief discussion of the most commonly used lateral chip designs, including BA diode lasers and arrays, was given. In this chapter, a more detailed phenomenological and theoretical description of coupled arrays in general, and gain guided stripe-arrays in particular, will be presented. Coupled stripe-arrays tend to operate in a global mode, the so called supermode. Two models are used to illustrate the array supermodes and the mechanisms for the coupling are described. Furthermore, numerical simulations of the stripe-array diode laser have been performed.

Coupled stripe-array diode lasers and amplifiers: The stripe-arrays used in this work were manufactured by M2K LASER GMBH. A scheme is depicted in Fig. 3.1. If the front facet is AR-coated, the term amplifier will be used. For non AR-coated devices, the term diode lasers is used. The lateral stripe-array substructure was realized by a patterned electrode in slow-axis direction. The emitter had a width of 400 μm, several contact stripes
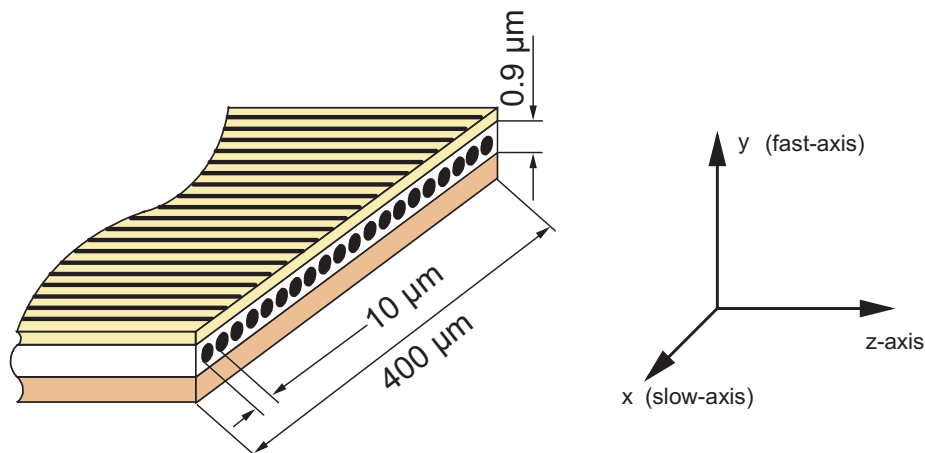
Figure 3.1: Schematic drawing of a gain guided stripe-array amplifier. In lateral direction (slow-axis) a stripe-array is realized by a patterned electrode. The current is injected through small stripes with a width of 4 μm and a pitch of 10 μm. The emitter width was 400 μm. In direction of the fast-axis index guiding is realized with a 0.88 μm waveguide.

each with a width of 4 μm and a pitch of $d = 10$ μm were realized by etching trenches with a depth of 200 nm into the p-doped cap layer before metalization. Only one additional fabrication step is necessary compared to a standard BA structure.

The active region featured a 7 nm thick InGaAs quantum well and a waveguide with a height of 0.88 μm and spanned the whole width of the device. A description of this large optical cavity layer structure can be found in subsection 2.3.1. With a similar epitaxial layer structure and a standard BA diode laser with a width of 80 μm and a length of 2 mm cw output powers of up to 7 W have been reported [42].

3.1   Array design considerations and brightness scaling

Instead of simply broadening the area of emission as in a BA diode laser, scaling of the output power can be realized by arranging several emitters in a row. The far-field emission of such an array of individual emitters can be described as the superposition of individual beams emitted from each of the emitters. Depending on the phase relationship between neighboring emitters constructive or destructive interference will occur under a specific far-field angle. This can be calculated for a given number of emitters N, the emission wavelength λ (equal for all emitters) and the phase difference between adjacent emitters.

Concerning the temporal coherence of the array emission three cases can be distinguished:

- Coherent, single-longitudinal mode operation: all emitters of the array will oscillate at the same wavelength and the array will have a bandwidth $\Delta\lambda$ following the Schawlow-Townes-Henry linewidth (equation 2.21)

- Quasi single-longitudinal mode operation: each emitter of the array will operate single-longitudinal mode but not all emitters will operate at the same wavelength

- Incoherent, broadband operation: the array emission will be longitudinal multi-mode without temporal coherence between the emitters

For simplicity, only the first case of temporal coherent single-longitudinal mode operation of the array will be discussed in this section.

Furthermore, two cases concerning the spatial coherence of the array emitters can be distinguished:

- Arbitrary phase relationship between the emitters of an array

- Fixed phase relationship between the emitters of an array

If there exits an arbitrary phase relationship between the fields of the individual emitters at the front facet of the array, no stable far-field distribution will be achieved. The power P of the array will scale linearly with the number of emitters N and the far-field angle θ will be independent from the number of emitters in this case [43]:

$$\theta = \frac{\lambda}{w},$$
(3.1)

whereas w is the width of an individual emitter. The brightness B will remain constant, independently from the numbers of emitters N of such an incoherent array. Devices where

this kind of operation is present are mostly arrays of BA diode lasers arranged in so called laser bars. Each emitter has a Fabry Perot cavity without wavelength stabilization and the spacing between the emitters is too large to achieve a coupling between the fields.

If the individual emitters of an array are realized with close proximity, the fields of neighboring emitters can couple with each other [44]. The far-field distribution of such an array with temporal coherent emission and a fixed phase relationship between the emitters can be described as a diffraction grating with N slits. Considering all emitters of an array being perfectly phase-coupled and the phase difference between all emitters being zero, the far-field distribution in lateral direction (x) will show a dominant single lobed output beam along the optical axis. This single lobe will have a far-field divergence of

$$\theta \approx \frac{\lambda}{N \cdot d},$$
(3.2)

where d is the distance between the emitters. Thus, the brightness of such a coherently phase-coupled diode laser array will scale with the number of emitters N. This kind of on-axis spatial coherent coupling with fixed phase relationship between the emitters of the array is very challenging.

However, it was experimentally observed that stripe-arrays tend to operate in the out-of-phase mode and show the same double lobed lateral far-field as the standard BA devices. The physical reasons for this behavior will be discussed briefly in the next sections. For further reading, the textbooks by Carlson [43] and Botez [44] are recommended.

3.1.1 Coupling mechanisms

Depending on whether gain guiding or index guiding is realized to achieve optical confinement, the two coupling mechanisms can be distinguished:

- Index guiding (strong optical confinement): Evanescent field coupling

- Gain guiding (weak optical confinement): Leaky wave coupling

These two coupling mechanisms are schematically depicted in Fig. 3.2.

(a) I (b)
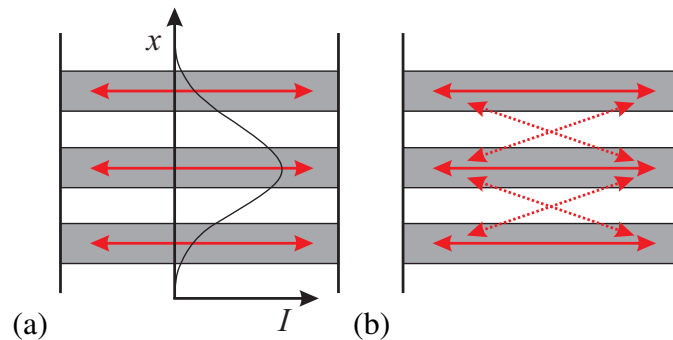
Figure 3.2: Coupling mechanisms for the coupling of an array. (a) Evanescent field coupling (b) Leaky wave coupling [44, 45].

Evanescent-field coupling: If two step index waveguides (each having strong optical confinement) are close together, the fields of the individual waves can overlap in the outermost regions (Fig. 3.2 (a)). In this case, the overlap depends on the distance between the waveguides. The overlap will result in a coupling between the fields of neighboring array emitters and is called evanescent field coupling. Since the evanescent wave can only influence the next adjacent stripe it is also called serial coupling.

The strength of the coupling between two neighboring fields is given by the coupling coefficient κ, which can be derived by the overlap integral [46]:

$$\kappa = \omega\varepsilon_0 \int \int_{-\infty}^{\infty} \Delta\varepsilon\,(x,y)\mathbf{E}^{(1)}(x,y)\mathbf{E}^{(2)*}(x,y)dxdy, \tag{3.3}$$

whereas $\Delta\varepsilon$ describes the influence of the second wave on the undisturbed wave $\mathbf{E}(1)$ in the first waveguide, while $\mathbf{E}^{(2)}$ is the undisturbed wave in the second waveguide.

Leaky wave coupling: Gain guided emitters have a low optical confinement and therefore, leaky waves can occur. The main difference to evanescent wave coupling is that leaky waves can propagate, while the evanescent waves decay exponentially (see Fig. 3.2). Thus, coupling can be realized even when the emitters are manufactured at a larger distance. Furthermore, a strong global coupling between the emitters can be achieved because not only next neighboring stripes are coupled. Therefore, this coupling scheme is also called parallel coupling.

Guiding and antiguiding: Both coupling mechanisms are present in a gain guided stripe-array diode laser since the injection of carriers will change the refractive index and the temperature in the pumped regions (subsection 2.2.3). Figure 3.3 shows the two possible guiding mechanisms that characterize such a gain-guided array.

Near threshold, the injection of carriers will lead to a decrease of the refractive index in the pumped regions. This will result in a negative index step, whereas the wave will be guided rather in the unpumped regions. This is called antiguiding and is depicted in Fig. 3.3 (b). Since the wave is only confined due to the presence of carriers, this will result in a strong leaky wave coupling. If the temperature in the pumped regions of the junction increases by Joule heating, this will cause an increase of the refractive index. Thus, at higher injection currents a gain guided array should act similar to an array of diode lasers with a positive index step, which is referred to be positive guiding (Figure 3.3 (a)).
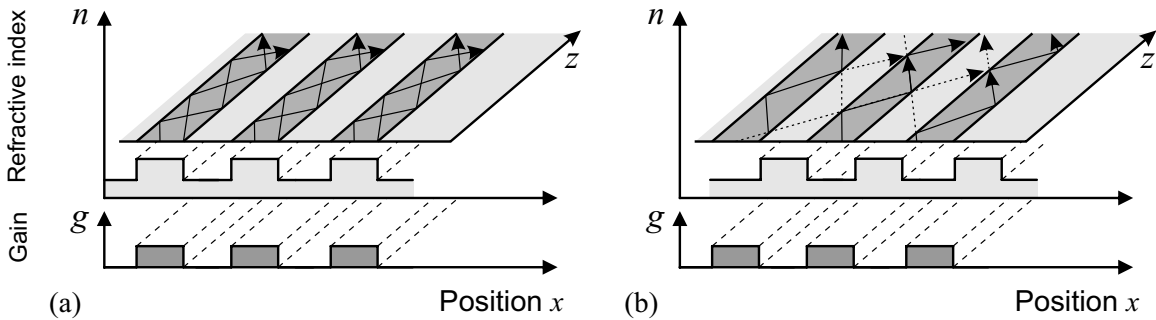
Figure 3.3: (a) Positive guiding with evanescent wave coupling and (b) antiguiding with leaky wave coupling [44, 45].

3.1.2 Array supermodes and off-axis emission

Usually, the coupling between adjacent emitters results in a global coupling of all emitters. Thus, the array will operate in a so called supermode that characterizes the emission of all coupled emitters. Several models for the calculation of the field distributions of globally coupled diode laser arrays exist. For a better understanding of the so called array supermodes, two of these models will be shown here to describe the tendency of the arrays to emit a double lobed far-field. A fully dynamic traveling wave model and numerical results for the actual stripe-array diode laser will be presented in the next section 3.2.

Diffraction model: In a simple model, the emitters of an array can be approximated by a grating with N representing the number of emitters of the array. In this case, the far-field distribution $I(\theta_x)$ of the array derived from the Fresnel-integral (equation 2.18) can be written as [47]:

$$I(\theta_x) = |E(\theta_x)|^2 \cdot A(\theta_x), \tag{3.4}$$

with the far-field amplitude $E(\theta_x)$ and the function $A(\theta_x)$ representing the array and the interference between the coupled emitters of the array. In the case of the simple diffraction model, this will read:

$$A(\theta_x) = A(u) = \frac{\sin^2\left(\frac{N \cdot u}{2}\right)}{\sin^2\left(\frac{u}{2}\right)}, \tag{3.5}$$

whereas $u = k_0 \cdot d \cdot \sin\theta_x$ with d being the pitch of the emitters. This represents a grating with N emitters as mentioned above.

Depending on the phase relationship between the emitters, constructive or destructive interference at certain far-field angles will be present. This can be expressed by introducing a phase shift term $\Delta\phi$:

$$A(u) = \frac{\sin^2\left[\frac{N}{2}(u + \Delta\phi)\right]}{\sin^2\left(\frac{u + \Delta\phi}{2}\right)}. \tag{3.6}$$

If a strict out-of-phase or an in-phase oscillation between neighboring emitters is assumed, the phase difference between adjacent emitters is $m_{order} \cdot \pi$. Here, m_{order} is the diffraction order giving in-phase oscillation for even numbers and out-of-phase oscillation for odd numbers. The angle of constructive interference can be calculated by:

$$sin\alpha = \frac{m_{order} \cdot \lambda}{2 \cdot d}. \tag{3.7}$$

The case of out-of-phase oscillation is schematically shown in Fig. 3.4.
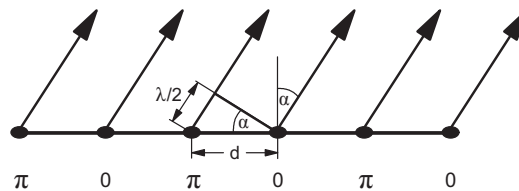
Figure 3.4: Simplified illustration of the lowest order out-of-phase mode of the emission of adjacent stripes following the diffraction model.

Figure 3.5 shows the calculated far-field distributions for (a) the lowest order in-phase mode ($m_{mode} = 0$ and $\Delta\phi = 0$) and (b) the lowest order out-of-phase mode with a phase
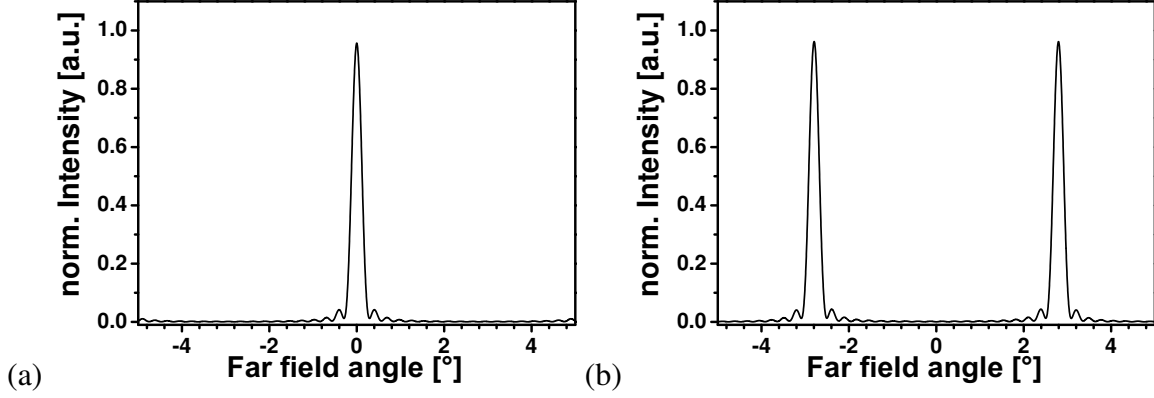
Figure 3.5: Calculated far-field distribution using the simple diffraction model for a diode laser
array with N = 40 emitter, an emitter width of 4 μm and a wavelength of λ = 976 nm
following the simple diffraction model [43, 44]. The two cases of (a) a phase difference
of $\Delta\phi = 0$ representing the lowest order in-phase mode and (b) a phase difference of
$\Delta\phi = \pi$ between adjacent emitters, representing the lowest order out-of-phase mode are
depicted.

relationship of $\Delta\phi = \pi$. An emitter number of $N = 40$, a wavelength of $\lambda = 976$ nm and
a pitch of $d = 10\ \mu$m have been used. The in-phase mode represents the case of perfect
coherent coupling between the emitters of an array. The resulting far-field shows a nearly
single lobed intensity distribution in direction of the optical axis (on-axis). For the lowest
order out-of-phase mode, the far-field shows a pronounced off-axis double lobed emission.
The angle between one of the lobes and the optical axis is called the off-axis angle and was
calculated to be $\alpha_{oa} = 48.8$ mrad ($\approx 2.8°$) for $\lambda = 976.0$ nm.

Coupled mode theory: In the coupled mode theory, the electric field distribution of the
array can be described as a superposition of the fields of N individual emitters [48]:

$$\psi_{Array}(x, y, z) = \sum_{m=1}^{N} C_m(z)\psi_m(x, y, z), \tag{3.8}$$

with $C_m(z)$ being the complex coefficient that determines the amplitude and phase of the
individual emitter. Since this coefficient has only a weak z dependence, the waveform
$\psi_m(x, y, z)$ of the $m - th$ array, with $m = 1, 2, ..., N$ can be written in separate form:

$$\psi_m(x, y, z) = u^m(x)v^m(y)e^{-\gamma z}, \tag{3.9}$$

with the lateral component $u^m(x)$ and the vertical component $v^m(y)$ and γ being the com-
plex two-dimensional propagation constant. By assuming just a coupling between the next
neighboring emitters and a uniform coupling constant over the whole array, the following
analytical solution for the array-modes $\psi_L(x, y, z)$ can be obtained for $L = 1, 2, \cdots, N$.
[47]:

$$\psi_L(x, y, z) = \sum_{m=1}^{N} \sin(m \cdot \theta_L)u^m(x)v^m(y)e^{-(\gamma+\gamma_L)z}, \tag{3.10}$$

with $\partial\gamma_L = \left(\frac{-k_0^2 \cdot c}{\gamma}\right) \cdot \cos(\theta_L)$, $k_0 = \frac{2\cdot\pi}{\lambda}$ and $\theta_L = \frac{L\cdot\pi}{(N+1)}$. Whereas $\partial\gamma_L$ are the eigenvalues
of the $L - th$ mode [48].

A result of the coupled mode theory is, that the array can be operated in a number of N
array modes with the mode order $L = 1, 2, ..., N$, whereas N is the number of emitters. The

array mode with $L = 1$ corresponds to the (lowest order) in-phase mode and the array mode with $L = N$ is the (lowest order) out-of-phase mode. However, the array can (in principle) operate in any mode in between these two cases. The array function from equation 3.5 will then become:

$$A_L(u) = \frac{\sin^2\left[\frac{(N+1)}{2}(u + \theta_L)\right]}{\left[\sin^2\left(\frac{u}{2}\right) - \sin^2\left(\frac{\theta_L}{2}\right)\right]^2},$$

(3.11)

with $\theta_L = L \cdot \pi (N + 1)$.

The near-field distributions for four of the allowed eight modes of a diode laser array with $N = 8$ emitters are depicted in Fig. 3.6. The position of the emitters are indicated by gray vertical bars in the graphs.
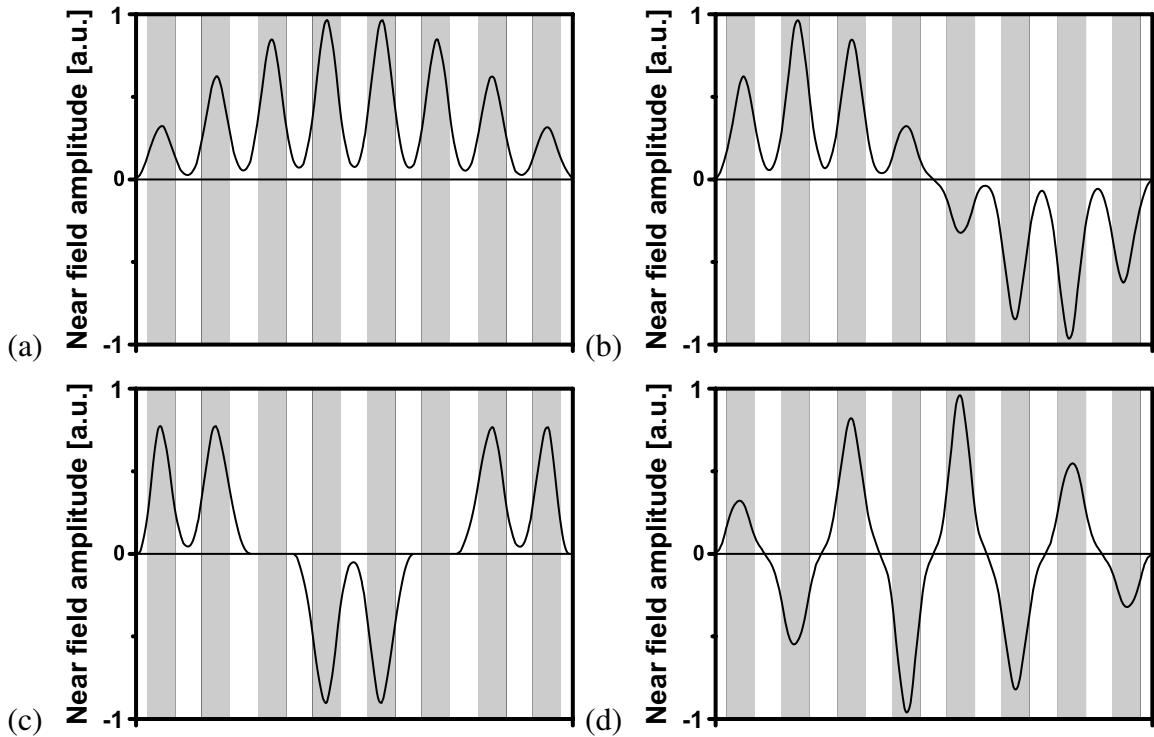
Figure 3.6: Near-field distributions for a diode laser array with N = 8 emitter. The four modes L= 1 (a) , L = 2 (b) , L = 3 (c) and L=8 (d) are depicted.

The near-field of the lowest order in-phase mode ($L = 1$, Fig. 3.6 (a)) has field strength between the emitters, where no gain is available. Thus, this mode will experience high losses since the field between the emitters will be absorbed. The near-field distribution of the lowest order out-of-phase mode ($L = 8$, Fig. 3.6 (d)) shows that this mode has no field strength in the unpumped regions. Thus, this mode will have the lowest losses compared to the other modes, especially the lowest order in-phase mode. As a rule of thumb, the higher the mode, the lower the losses also for the "in between" modes.

However, the far-field distribution of the higher order modes will have multiple peaks. For the two cases of $L = 1$ with a (nearly) single lobed far-field and $L = 8$ with a pronounced double-lobed far-field, the coupled mode theory and the diffraction model show similar results (please refer to Fig. 3.5). The full derivation of the equations presented here and a comparison between diffraction theory and coupled mode theory can be found in [47, 48].

3.2 Mathematical modeling

To predict the behavior of the stripe-array amplifier in an external cavity, numerical modeling of the actual device was performed assuming a stripe-array diode laser (without AR-coated front facet).

3.2.1 Traveling wave model

Self consistent modeling of diode laser arrays can be performed by using the traveling wave equation assuming a slab waveguide architecture. The model described here was used for the numerical simulation of distributed feedback tapered diode lasers and is described in more detail in [49]. A similar model was used for the simulation of a two-stripe diode laser array [50]. The model is based on the Maxwell's wave equation for the electric field $\mathbf{E}$ with the appropriate material equations for the polarization $\mathbf{P}$ and the carrier density N_C. The wave equation reads:

$$\left(\nabla^2 - \frac{1}{c^2}\frac{\partial^2}{\partial t^2}\right)\mathbf{E}(\mathbf{r}, t) = \frac{1}{\varepsilon_0 c^2}\frac{\partial^2}{\partial t^2}\mathbf{P}(\mathbf{r}, t), \tag{3.12}$$

with the speed of light $c = c_0/n$ and the vacuum permittivity ε_0.

In a semiconductor laser slab waveguide with z being the propagation direction of the optical field, assuming the field and the polarization to be linearly polarized perpendicular to the z-axis. Furthermore, the paraxial ray approximation can be made assuming slowly varying counterpropagating optical fields $E^\pm$:

$$E(x, z, t) = \left(E^+(x, z, t)e^{-i\bar{n}k_0 z} + E^-(x, z, t)e^{i\bar{n}k_0 z}\right)e^{i\omega_0 t} + cc.. \tag{3.13}$$

In the model, the complex slowly varying amplitudes $E^\pm$ of the forward and backward traveling optical fields 3.14 are coupled to an ordinary differential equation 3.15 for the complex slowly varying amplitudes $p^\pm$ of the induced polarization:

$$\frac{n_g}{c_0}\frac{\partial}{\partial t}E^\pm = -iD_p\frac{\partial^2}{\partial x^2}E^\pm + \left(\mp\frac{\partial}{\partial z} - i\beta\right)E^\pm - \frac{\bar{g}}{2}\left(E^\pm - p^\pm\right) + F_{sp}^\pm \tag{3.14}$$

$$\frac{\partial}{\partial t}p^\pm = \bar{\gamma}\left(E^\pm - p^\pm\right) + i\bar{\omega}p^\pm \tag{3.15}$$

whereas $D_p = (2k_0\bar{n})^{-1}$.

Equation 3.14 can be derived from the scalar wave equation by using a slowly varying forward and backward rotating wave Ansatz, paraxial approximation and the effective index method [51]. Equation 3.15 is a time domain description of a Lorentzian gain dispersion profile [52].

The real excess carrier density N_C is described by a parabolic diffusion equation that follows from a standard carrier transport equation:

$$\frac{\partial}{\partial t}N_C = D_N\frac{\partial^2}{\partial x^2}N_C + \Lambda(x) - R(N_C)$$
$$- \frac{c_0}{n_g}\mathfrak{Re}\sum_{\nu=\pm}E^{\nu*}[g(N_C, E)E^\nu - \bar{g}(E^\nu - p^\nu)], \tag{3.16}$$

whereas $\Lambda(x)$ is the transversely dependent pump term represented by:

$$\begin{cases} (J/q)\cdot h & , & x_i - \frac{1}{2}w \le x \ge x_i + \frac{1}{2}w \\ 0 & , & elsewhere \end{cases},$$

where q is the electron charge and x_i is the center of the ith stripe with the stripe width w.

The boundary conditions for the reflection at both facets of the laser at $z = 0$ and $z = l$ reads:

$$\begin{cases} E^+(t, x, 0) = \sqrt{R_0(x)}e^{i\varphi_0(x)}\, E^-(t, x, 0) \\ E^-(t, x, l) = \sqrt{R_l(x)}e^{i\varphi_l(x)}\, E^+(t, x, l) \end{cases}.$$

Here, $t \in \mathbb{R}$ denotes time, $z \in [0, l]$ corresponds to the longitudinal propagation direction, with the chip length l and $x \in \mathbb{R}$ is the lateral space dimension.

The complex propagation parameter β used in equation 3.14 is given by:

$$\begin{aligned} \beta &= \delta_0(x, z) + \delta_\Sigma(x, z, N_C, J) + i\frac{g(x, z, N_C, E) - \alpha(x, z)}{2}, \\ \delta_\Sigma(x, z, N_C, J) &= \delta_n(x, z, N_C) + \delta_T(x, z), \end{aligned}$$

with the peak gain g, that depends on the carrier inversion $N_C = N_C(t, x, z)$ within the active zone.

The factor $\delta_0(x, z)$ is a built-in variation of the dielectric function, independent of N_C and the temperature, whereas δ_n and δ_T introduce the dependence of the effective refractive index on N_C and the temperature, respectively.

The following models for g and δ_n were used:

$$\begin{aligned} g = g(x, z, N_C, E) &= g'(x, z)\frac{\ln\left(N_C(t, x, z)/N_{\text{tr}}\right)}{1 + \epsilon\|E\|^2}, \\ \delta_n(x, z, N_C) &= -k_0\sqrt{n'(x, z)N_C(t, x, z)}. \end{aligned}$$

The function $J(x, z)$ denotes the injection current density, so that the injection is given by:

$$J_{inj} = \iint J(x, z)dxdz.$$

A linear nonlocal dependence on the inhomogeneous current injection $J(x, z)$ is used to model heating of the device:

$$\delta_T(x, z) = \frac{k_0 n_g}{\lambda_0}\iint c_T(x, z, \tilde{x}, \tilde{z})J(\tilde{x}, \tilde{z})d\tilde{x}d\tilde{z}, \tag{3.17}$$

with the thermal coefficient c_T that describes local and nonlocal crosstalk thermal effects.

The parameters $\overline{g}$, $\overline{\lambda} = -\frac{\lambda_0}{k_0 c_0}\overline{\omega}$, and $\overline{\Gamma} = 2\frac{\lambda_0}{k_0 c_0}\overline{\gamma}$, denoting the amplitude, the peak wavelength detuning with respect to λ_0, and the full width at the half maximum of the Lorentzian approximating the gain profile can be also dependent on the instantaneous inversion $N_C(t, x, z)$ and the injection current induced heating.

The variation of the gain profiles with changing N_C were neglected in this model, but a thermal shift of the gain peak wavelength $\overline{\lambda}$ was assumed:

$$\overline{\lambda}(x, z) = \overline{\lambda}_0(x, z) + \iint \nu_T(x, z, \tilde{x}, \tilde{z})J(\tilde{x}, \tilde{z})d\tilde{x}d\tilde{z}.$$

The rate of nonradiative and spontaneous radiative recombination is given by

$$R(N_C) = A(x, z)N_C + B(x, z)N_C^2 + C(x, z)N_C^3 \tag{3.18}$$

Table 3.1: Parameters used in simulations

Symbol	Description	Unit	Value
$\overline{n}$	reference refractive index		3.27
n_g	group refractive index		3.66
λ_0	central wavelength	m	$976.0 \cdot 10^{-9}$
$\overline{g}$	Lorentzian gain amplitude	m^{-1}	10000
$\overline{\Gamma}$	Lorentzian width at half max.	m	$95 \cdot 10^{-9}$
$\overline{\lambda}$	gain peak detuning @ $J = 0$	m	0
$g'(x, z)$	differential gain		
	$(x, z) \in$ stripe	m^{-1}	5000
	$(x, z) \in$ elswhere	m^{-1}	0
$\alpha(x, z)$	internal absorption	m^{-1}	100
R_0	rear facet intensity reflectivity		0.9
φ_0	rear facet phase reflectivity		$1 \cdot \pi$
R_l	front facet intensity reflectivity		0.03
φ_l	front facet phase reflectivity		$0 \cdot \pi$
N_{tr}	transparency carrier density	m^{-3}	$1 \cdot 10^{24}$
ϵ	nonlinear gain compression	m^3	0
n'	differential index	m^3	$5 \cdot 10^{-31}$
D_N	carrier diffusion coefficient	$m^2 s^{-1}$	$20 \cdot 10^{-4}$
l	length of the chip	m	$1.5 \cdot 10^{-3}$
w_{stripe}	contact stripe width	m	$4 \cdot 10^{-6}$
h	thickness of active region	m	$7 \cdot 10^{-9}$
A	recomb. parameter Eq. (3.18)	s^{-1}	$3 \cdot 10^8$
B	recomb. parameter Eq. (3.18)	$m^3 s^{-1}$	$1.8 \cdot 10^{-16}$
C	recomb. parameter Eq. (3.18)	$m^6 s^{-1}$	$3 \cdot 10^{-42}$
c_T	thermal coeff. $c_T(x, z, \tilde{x}, \tilde{z})$		
	$(x, z), (\tilde{x}, \tilde{z}) \in$ stripe	$A^{-1}m$	$0.75 \cdot 10^{-9}$
	elsewhere	$A^{-1}m$	0
ν_T	thermal coeff. $\nu_T(x, z, \tilde{x}, \tilde{z})$		
	$(x, z), (\tilde{x}, \tilde{z}) \in$ stripe	$A^{-1}m$	$2.7 \cdot 10^{-9}$
	elsewhere	$A^{-1}m$	0

and the last expression in 3.16 is the rate of stimulated recombination, which takes into account the contribution from the polarization model 3.15.

Finally, the stochastic term $F_{\text{sp}}^{\pm}$ in 3.14 represents the contribution of spontaneous emission to the optical field. It is modeled similarly as described in [53].

All other coefficients, with the exception of $k_0 = \frac{2\pi}{\lambda_0}$, n_g, $\bar{n}$ and D_N, are allowed to be spatially nonhomogeneous and discontinuous, depending on the heterostructural laser geometry. The values and their explanation are given in Table 3.1.

3.2.2 Numerical method and results: stripe-array diode laser

The numerical modeling was performed at the WIAS[1] by Mindaugas Radziunas and Mark Lichtner, since the computing capability of a standard PC is not sufficiently fast for this kind of dynamic 2+1D modeling with an appropriate resolution. The corresponding software tool was written by Mark Lichtner.

The numerical method was similar to that described in [54], where a splitting scheme was used to solve the equations 3.14-3.16. Fast Fourier transform was used to derive the lateral optical diffraction and carrier diffusion along the x direction. The remaining coupled hyperbolic system in equation 3.14 was integrated along characteristics using finite differences. For numerical stability it was crucial to resolve the stiff equation 3.15 adequately. An exponentially weighted scheme with forward values for $E^{\pm}$ was used. This scheme ensures, that in the limit for $\overline{\gamma} \to \infty$ the discretized solutions for p converged to E.

The resolution of the coupling of the array emitters required a sufficiently fine lateral space discretization. Similarly, a proper propagation of the fast oscillating modes along the characteristics, as well as the resolution of a sufficiently large optical frequency range, requires a fine time- and longitudinal space discretization. A uniform spatial grid with the steps of $\Delta x = 0.666\mu$m, $\Delta z = 5\mu$m, resulting in a time step of ~ 0.061ps was used. This spatial grid has 210000 nodes, yielding 1.89 million real unknown variables.

The large scale system of equations was solved using multilevel parallel distributed computing (MPI+Multithreading), that allowed to run long time dynamic simulations over large parameter ranges, corresponding to simulation times of more than 3000ns on a blade cluster of 64 quad core Intel $Xeon5430$ processors interconnected via infiniband (HP CP3000BL 32xHP BL460c) in only one day [55]. Comparable computations on a single PC system take nearly 100 times longer.
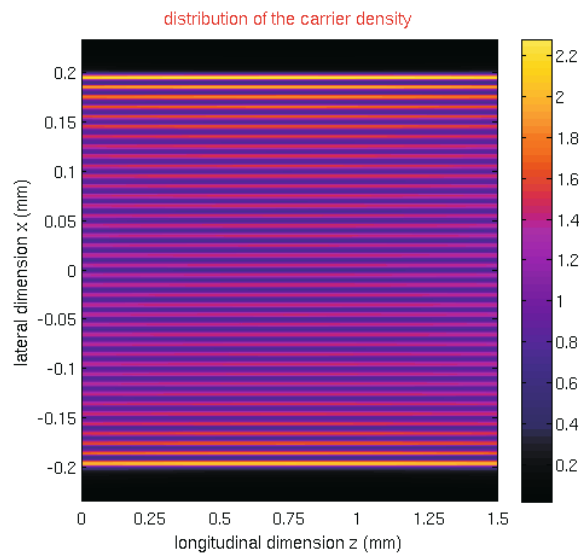
Figure 3.7: Carrier distribution used for the modeling of the stripe-array diode laser. (With the permission of M. Radziunas)

The carrier distribution for the 40 stripe-array used for the modeling is depicted in Fig. 3.7. The calculated near-field intensity distribution is depicted in Fig. 3.8 (a). The fields of the 40 emitters can be resolved. However, the intensity distribution is not homoge-

---

[1]Weierstrass Institute for Applied Analysis and Stochastics, www.wias-berlin.de

neous. Rather, an envelope with a nod in the middle is observed. This indicates the presence of a mode with a number slightly of the out-of-phase mode (e.g $L = 39$).

Figure 3.8 (b) shows the calculated far-field intensity distribution of the stripe-array diode laser. Two main peaks at far-field angles of $\alpha_{oa} = \pm 2.8°$ are observed, corresponding to the mode number $L = 40$ for $\lambda = 976.0\ nm$. The intensity of both peaks is slightly asymmetric. Furthermore, side lobes in between the two main peaks are present. The angle of the far-field distribution of these two inner peaks is $\alpha_{oa} = \pm 2.5°$ corresponding to the mode number $L = 36$ for $\lambda = 976.0\ nm$. An explanation for the non-perfect out-of-phase coupling between the emitters of the free running array is the lack of wavelength stabilization or selectivity.

(a)   (b)
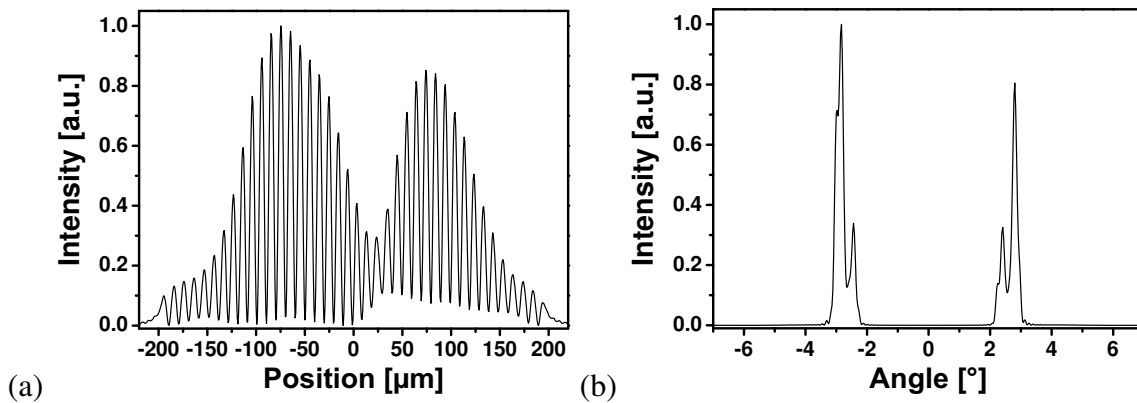
Figure 3.8: Calculated (a) near-field intensity distribution and (b) far-field intensity distribution of the free running stripe-array diode laser.

3.3 Summary

In this chapter, a phenomenological and theoretical description of coupled diode laser arrays was given. With the diffraction model, an intuitive picture of the array can be given if the emitter are coupled in-phase and out-of-phase. Furthermore, near-field distributions following the coupled mode theory have been calculated to illustrate the different array modes. Both models can be used to explain the double lobed far-fields of such arrays in a first approximation.

A traveling wave model was used for the numerical simulation of the gain guided stripe-array as a laser. The near-field and far-field intensity distributions were simulated. The numerical simulations have proven that the stripe-array as a laser operates preferably in a supermode close to the lowest order out-of phase mode. However, the simulations showed a non perfectly pronounced double lobed lateral far-field. It is assumed that the lack of wavelength stabilization is the reason that the array operates not exactly at the out-of-phase supermode.

The stripe-array as an amplifier can be wavelength stabilized with an external cavity. Furthermore, this external cavity can be designed off-axis to support the "native" lateral double-lobed emission and stabilize the out-of-phase supermode. The calculated far-field pattern corroborate this assumption. In the next chapters the gain guided stripe-array amplifier is investigated experimentally in different external cavity configurations.

Chapter 4

Transversal mode selection with off-axis external cavities

Several techniques to achieve emission with good spatial beam quality from standard BA and stripe-array diode lasers have been reported in the literature. This includes the use of mode apertures, phase masks [56] and phase conjugation [10, 57]. Moreover, it was shown that the double lobed emission can be supported by operating BA diode lasers in off-axis resonators [8, 58, 59] or by off-axis injection locking with a master laser [60].

As discussed in the previous chapter, the emitters of a stripe-array are coupled most likely in the out-of-phase supermode. This results in a double lobed far-field distribution in lateral direction similar to that of BA diode lasers. Furthermore, the numerical results presented in section 3.2 have shown, that the particular stripe-array used in this work possesses this strong double lobed far-field. Thus, the out-of-phase coupling between adjacent emitters can be enforced by setting up an external resonator with a high angular selectivity.

Since one aim of this work was to achieve emission with a high brightness from BA and stripe-array amplifiers, the selection and stabilization of a certain supermode with an external cavity was experimentally investigated here. Therefore, BA and stripe-array amplifiers have been characterized with two off-axis external cavity designs in this chapter.

4.1 Characterization of the stripe-array amplifier

A crucial aspect for operating a diode laser in an external cavity is the suppression of the longitudinal and transversal modes of the Fabry-Perot chip resonator. If the chip modes of the diode laser are not sufficiently suppressed, mode competition can occur. Thus, an AR coating on the front facet with a residual reflectivity in the range below 0.1% is necessary. In this case, an amplifier is realized that can be integrated to an external cavity as gain medium. Such amplifiers are characterized by the emission of spectrally broad super-luminescence and can also be realized with AR coatings at both facets.

The stripe-array amplifiers investigated here, were AR coated at the front facet by using a single layer of silicon nitride. The manufacturer specifies the reflectivity to be $R_F < 0.5 \cdot 10^{-5}$ at the gain maximum and $R_F < 10^{-5}$ over the whole spectral gain width. The back facet had a reflectivity of $R_B > 90\,\%$ and was realized by a stack of silicon oxide and silicon nitride layers.

The quality of the AR-coating can be evaluated by the shape of the super-luminescence output as a function of the injection current. In Fig. 4.1, the power as a function of the injection current for three different amplifiers are shown. Two 400 μm wide stripe-array
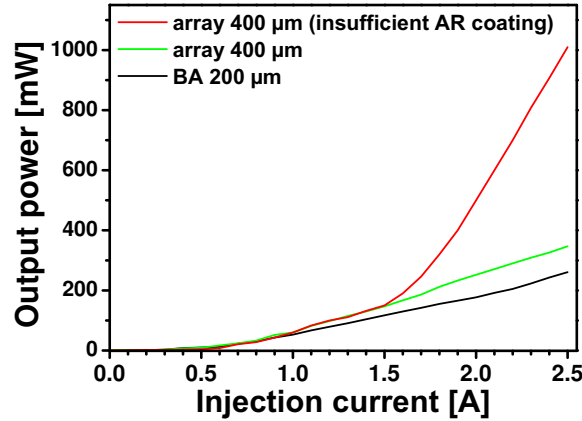
Figure 4.1: Output power of the free running BA and stripe-array amplifiers as a function of the injection current without external cavity.

amplifiers and a 200 μm wide BA amplifier have been investigated up to an injection current of 2.5 A. The 200 μm wide BA amplifier was chosen because the effective emitting area of the 400 μm stripe-array is $40 \cdot 4\mu$m = 160 μm. However, a 160 μm wide emitter was not available. The output power of the super-luminescence for the stripe-array amplifier with good AR coating (green line) was below 350 mW at 2.5 A and no kinks indicated the onset of lasing. The red line indicates the output power of the stripe-array with insufficient AR-coating. This device started lasing at about 1.5 A and the output power was nearly three times higher than for the well AR-coated chip. The third curve (black line) represent the measurement with the BA amplifier. No onset of lasing was observed, indicating a well AR coated facet.

From these measurements a high quality of the AR coating is assumed for the two chips with the low output powers. Those chips were selected for further investigation.

Another method to evaluate the quality of the AR-coating is to investigate the spectral emission of the super-luminescence. Figure 4.2 shows the corresponding spectra for the two 400 μm wide chips for different injection currents. The super-luminescence spectra of the amplifier having the specified AR-coating 4.2 (a) remained broad even at higher injection currents. In contrast, the emission spectra of the amplifier with the insufficient AR-coating showed several narrow spectral peaks above an injection current of 1.5 A, as shown in Fig. 4.2 (b). These spectral peaks are attributed to lasing of the chip itself.

From these measurements a high quality of the AR coating is assumed for the two chips with the low output powers. Those chips were selected for further investigation.

Figure 4.2: Spectra of the free running stripe-array amplifier for different injection currents for the case of (a) good AR-coating and (b) insufficient AR-coating.

4.2   Off-axis external cavities

Two different off-axis external cavity approaches can be distinguished:

Symmetric off-axis feedback: In the symmetric off-axis external cavity design, feedback is provided on both lobes of the do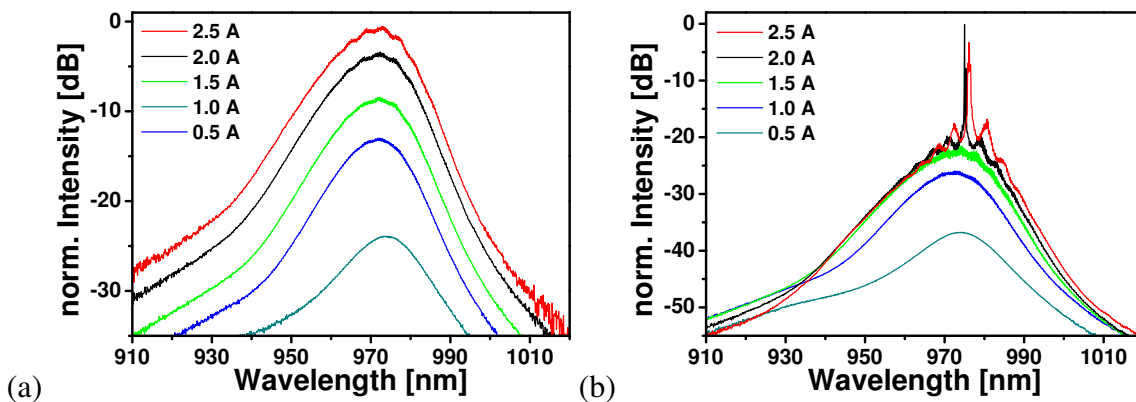uble lobed emission equally [8, 61]. This results in a homogeneous near-field distribution. The drawback of this scheme is that the output power is equally distributed over the two output lobes. Although a certain transversal supermode can be selected and stabilized, the output remains double lobed. Each of the two lobes can show a nearly diffraction limited behavior and the two beams can be superimposed into one single beam by polarization coupling [62], but the effort is correspondingly high. Thus, the application of a symmetric off-axis ECDL is limited.

Asymmetric feedback: A way to overcome this drawback is to provide asymmetric off-axis feedback [7, 8, 27, 63–68]. Two ways of asymmetric feedback are possible. One way is providing feedback on both lobes but with different reflectivities. The other way is provide very strong feedback on one side and no feedback on the other side. In both cases, this results in asymmetric far-field and near-field distributions. The advantage of the asymmetric scheme is, that the lobe with (stronger) feedback is less pronounced while the other lobe can be coupled out. Thus, more power is concentrated in the outcoupled lobe especially when no feedback on this lobe is present (see subsection 4.2.2).

In the following two subsections two different schemes to realize angular selective external cavities will be presented. In principle, both resonator schemes can be realized asymmetric and symmetric.

4.2.1   Spherical aberrations for symmetric off-axis feedback

Usually, spherical aberrations have to be avoided in any optical setup, especially in resonators. However, in some cases the spherical aberrations can be utilized to achieve a positive effect. In this subsection, the use of the spherical aberrations of a plano-convex lens to realize an angular selective resonator is described. A standard BA and a stripe-array amplifier have been investigated.

If a plano-convex lens is irradiated by collimated monochromatic light, the focal point for outer rays will be closer to the lens than the focal point from paraxial rays. The aberrations will become stronger if the lens is placed with the convex side facing the focus. A simulation made with the ray tracing software ZEMAX for the two lens orientations is depicted in Fig. 4.3 exemplarily for a lens with $f = 50$ mm and a diameter of 22 mm. The deviation between the focal planes of paraxial rays and the rays incident on the edges of the lens is increased from 2.5 mm to 10 mm if the lens is placed "the wrong way round" as shown on the right hand side of the picture. This effect can be exploited to form an angular selective external cavity [64, 65].

The experimental setup of a symmetric feedback scheme utilizing this effect is depicted in Fig. 4.4 along the slow-axis of the diode. In fast-axis, the diode (amplifier) emission is collimated using an FAC. Since the emission in this direction is nearly diffraction limited, it can remain uninfluenced by the external resonator. In slow-axis, a plano-convex cylindrical lens with the curved side facing the stripe-array and the BA amplifier, respectively was used. A plane mirror with a reflectivity of $R_M > 20$ % was placed perpendicular to the optical axis.
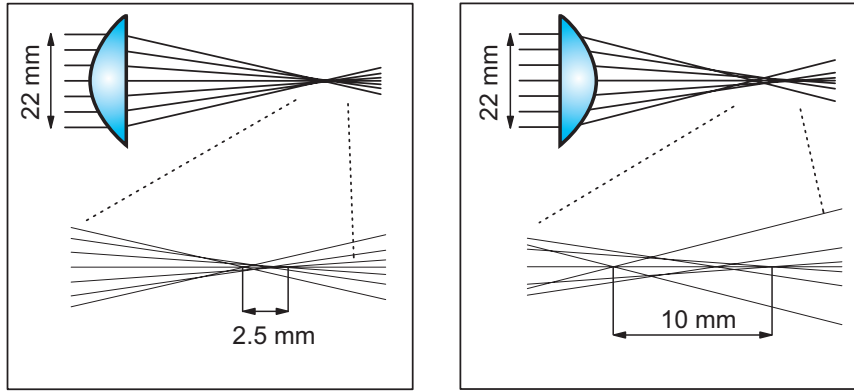
Figure 4.3: Illustration of the spherical aberrations of a plano-convex lens [69].

For a given distance d_{lens} between the amplifier and the lens, a specific angular emission from the amplifier is supported by the resonator. This case is indicated by the solid line in Fig. 4.4. The emission from the amplifier matching to this feedback angle $\pm\ \alpha_{\text{FB}}$ will be collimated behind the lens. This angular emission will be incident perpendicular at the mirror. Therefore, it will be reflected back onto itself and back into the amplifier. Emission that exits the amplifier at a different angle than $\pm\ \alpha_{\text{FB}}$ will have a skew incident angle at the mirror, which is indicated by the dashed line in the picture. Thus, it will not be fed back into the active region and cannot be amplified. In other words, the feedback angle $\pm\ \alpha_{\text{FB}}$ that is supported by the resonator can be adjusted by changing the distance between the lens and the amplifier.
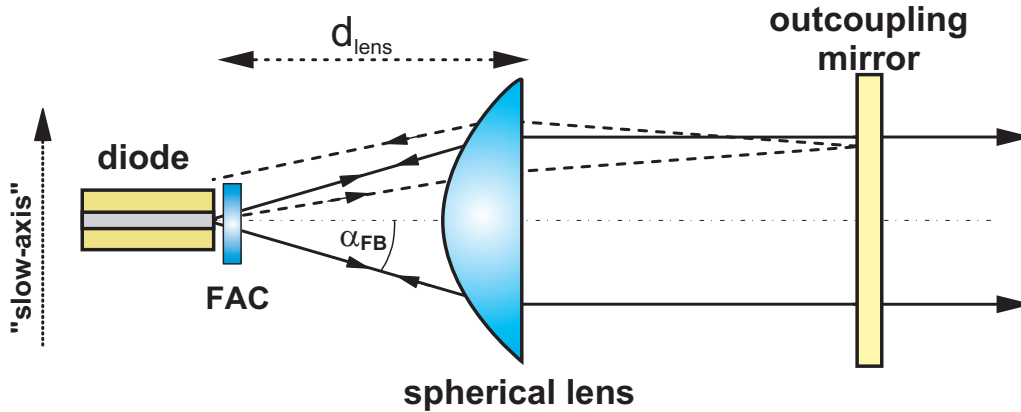
Figure 4.4: Sketch of the angular selective external cavity comprising a plano-convex cylindrical lens for transversal mode selection.

This scheme was studied as symmetric and asymmetric design [65, 70], but in these cases additional apertures or stripe mirrors were used. Here, the symmetric scheme utilizing just one feedback mirror and no apertures was investigated to evaluate the quality of the angular selectivity of the spherical aberrations alone.

Comparison between standard BA and stripe-array amplifier: The far-field emission behavior of the stripe-array and the standard BA amplifier that were characterized in section 4.1 were investigated. Both chips had a center wavelength of about 974 nm, while several longitudinal modes were present in most cases. The angular selective external cavity was set up symmetrically as depicted in Fig. 4.4. A plano-convex cylindrical lens with
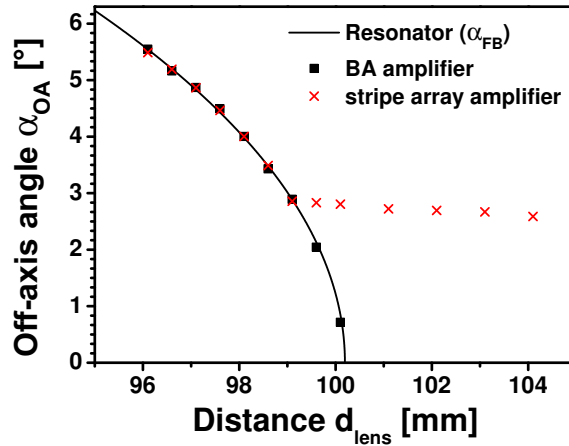
Figure 4.5: Off-axis angle of the emission as a function of the distance d_{lens} between the spherical lens and the amplifiers. The black line indicates the corresponding calculated feedback angles α_{FB} supported by the resonator.

a focal length of $f = 100$ mm was mounted on a precision translation stage. A plane mirror with a reflectivity of $R_M = 20\%$ was placed in a distance of $d_M = 100$ mm with respect to the lens. To change the feedback angle, the distance between lens and amplifier was changed. In other words, the lens to diode distance d_{lens} corresponds to a certain feedback α_{FB} angle supported by the resonator. To determine the off-axis angle the far-field distributions in lateral direction have been measured for different lens to diode distances by using the *Beamscope*. The feedback angle given by the resonator was compared to the off-axis angle of the emission from the ECDL.

The off-axis angle (α_{OA}) of the emission of the two amplifiers is depicted in Fig. 4.5 as a function of the lens position, whereas the angle between the two lobes in the far-field is defined as $2 \cdot \alpha_{OA}$. The theoretical feedback angle (α_{FB}) of the resonator is represented by the black line in Fig. 4.5. It can be calculated with a ray tracing program as illustrated in Fig. 4.3.

The black squares in this graph represent the values measured using the standard BA amplifier, while the red crosses correspond to the stripe-array amplifier. Both amplifiers were investigated at an injection current of 1.5 A. The characteristic double lobe emission was observed in most cases. The angular emission of the standard BA amplifier followed the resonator in all cases. For longer distances than $d_{\text{lens}} = 100$ mm, the standard BA amplifier did operate on-axis. The angular emission of the stripe-array amplifier followed the resonator only for short lens to diode distances. For small angles ($d_{\text{lens}} > 99.2$ mm), the stripe-array tended to operate close to its "native" off-axis angle ($\pm\alpha_{OA} = 2.79°$ for $\lambda = 974.0$ nm).

The corresponding far-field intensity distributions are depicted in Fig. 4.6 for the standard BA amplifier and in Fig. 4.7 for the stripe-array amplifier at six different feedback angles. Each graph shows the far-fields measured for three different injection currents.

The standard BA amplifier showed the characteristic double lobed far-field emission in nearly all cases (Fig. 4.6 (a-e)). However, the shape of the two far-field lobes was rather broad and multiple peaks indicated non diffraction limited emission. Furthermore, the width of the double lobes broadened with decreased feedback angle and the on-axis background became stronger, especially at higher injection currents. The far-fields measured with the standard BA amplifier showed, that this diode did not have a distinct preferred emission angle. At $\alpha_{\text{FB}} = 0.7°$ (as shown in Fig. 4.6 (f)), the double lobes were only visible

Figure 4.6: Far-field intensity distribution of the standard BA amplifier operated in the off-axis external cavity with plano-convex lens for different feedback angles $\pm \alpha_{\mathrm{FB}}$.

at the laser threshold of 0.75 A (green line). At higher injection currents, a multiple lobe on-axis emission was observed at this feedback angle.

Figure 4.7 (a-f) shows the corresponding far-fields for the stripe-array amplifier. At large feedback angles, the stripe-array amplifier did operate at an off-axis angle matching to the feedback angle. However, for smaller feedback angles than 2.8° and at higher injection currents, the stripe-array tended to operate close or at its native off-axis angle. At a feedback angle of 5.6°(Fig. 4.7 (a)), a double lobed emission at approximately the feedback angle was observed at low injection currents. By increasing the injection current to 2.0 A, the far-field showed four lobes, whereas the two inner lobes match to the "native" out-of-phase mode operation of the stripe-array. If the feedback angle was decreased further (Fig. 4.7 (b-d)), the far-field lobes broadened and the on-axis background increased. However, if the feedback angle matched exactly the angle corresponding to the out-of-phase coupling of the array emitters as depicted in Fig. 4.7 (e), the far-field showed two very pronounced peaks without any background or on-axis radiation. In this case, each of the two lobes was nearly diffraction limited. The standard BA amplifier did not show such a distinct preference to any feedback angle. If the feedback angle was decreased further, the stripe-array amplifier still tended to operate close to its native off-axis angle, while the external cavity supported considerably smaller feedback angles. As shown in Fig. 4.7 (f), the stripe-array operated at
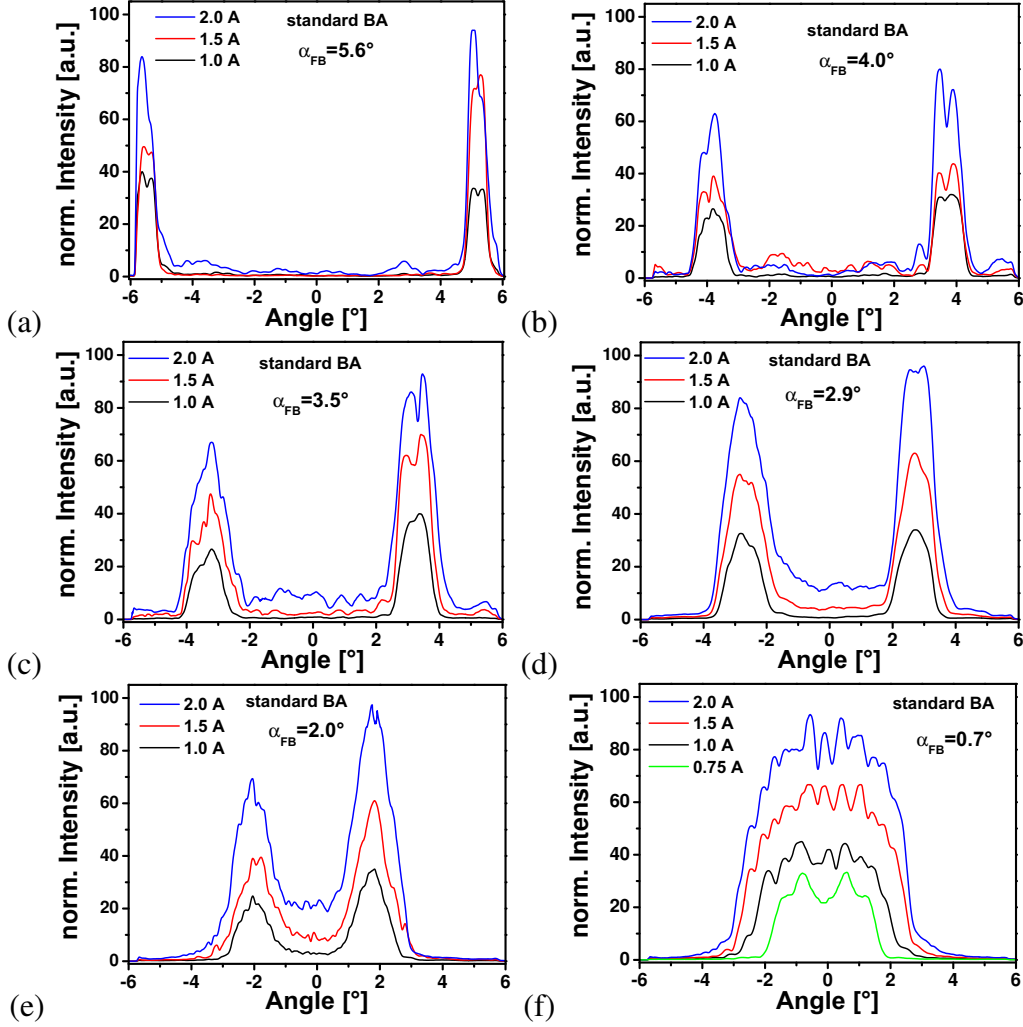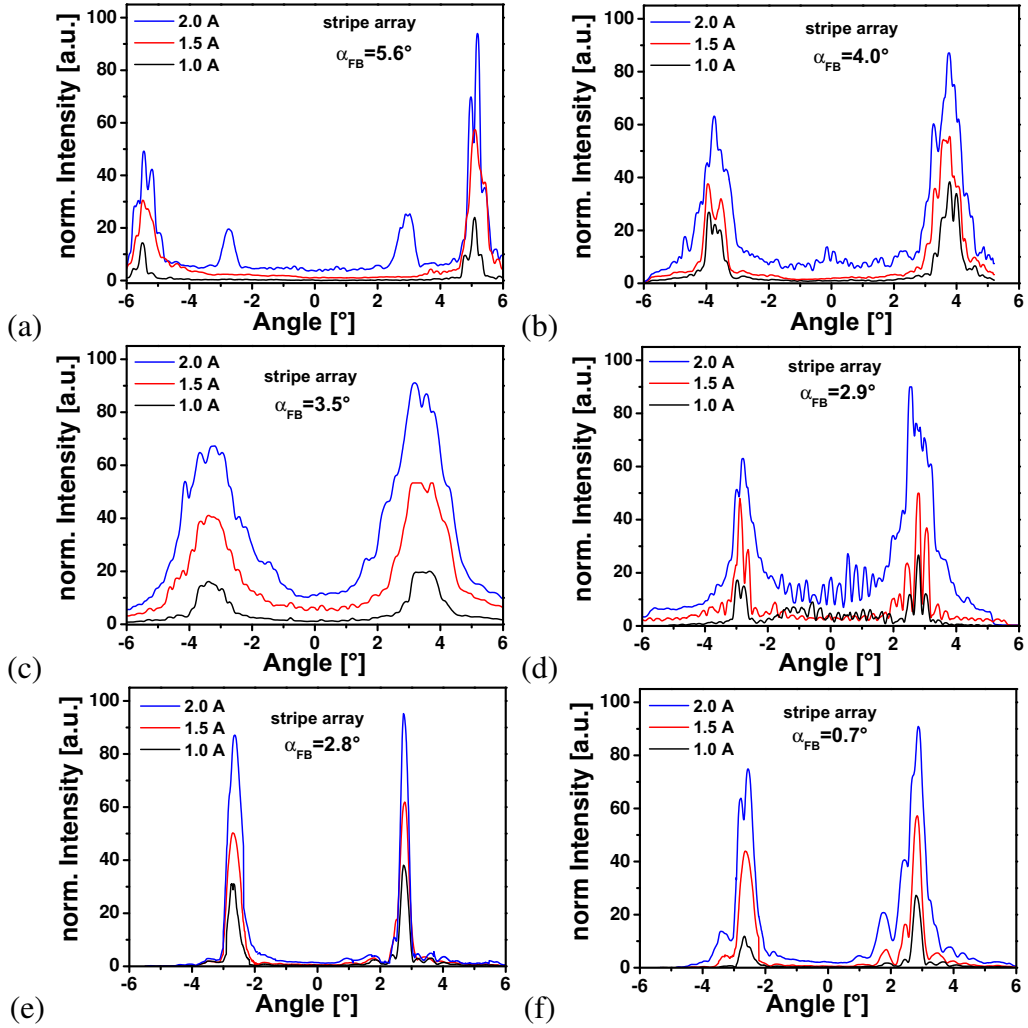
Figure 4.7: Far-field intensity distribution of the stripe-array amplifier operated in the off-axis external cavity with plano-convex lens for different feedback angles $\pm \alpha_{\mathrm{FB}}$.

an off-axis angle of $\alpha_{OA} \approx 2.75°$, while the feedback angle supported by the resonator was $\alpha_{\mathrm{FB}} = 0.7°$. This is attributed to the lower impact of aberrations for smaller angles.

Several consequences result from these measurements: First off all, the stripe-array possessed a preferred angular emission, while the standard BA amplifier can be operated at arbitrary feedback angles. Secondly, the angular selectivity of this resonator was insufficient to dominate the stripe-array. Furthermore, the angular selectivity was lower at small feedback angles (and shorter lens to diode distances, respectively), because the spherical aberrations are weaker in this case. However, the angular selectivity was sufficient to dominate the standard BA amplifier in all cases. This can be explained by filaments arising inside the BA amplifier matching to the off-axis feedback from the external cavity. If the feedback angle is changed, these filaments will follow the external cavity. In contrast, the stripe-array has well defined stripes resulting in a "native" off-axis emission angle. This agrees well with the simulations made in the previous chapter and the theory of array supermodes [43, 44].

The aberrations of the lens alone are not strong enough to provide a precisely defined angular selective resonator. However, this precision is necessary to select a certain array supermode. Additional mode apertures or stripe mirrors are necessary to realize high angular selectivity. The combination of slow-axis lenses and stripe mirrors (or the use of apertures

in front of mirrors, respectively) was reported in the literature [7, 8, 27, 66, 67].

4.2.2   Plane mirror for asymmetric off-axis feedback

A simple resonator for asymmetric off-axis feedback with a high angular selectivity can be realized with a plane mirror tilted with respect to the optical axis. A sketch of this resonator scheme is depicted in Fig. 4.8. The stripe-array amplifier emission in fast axis direction was collimated using an FAC. In slow-axis, angular selective feedback at $\pm\,\alpha_{\mathrm{FB}}$ was provided with a plane mirror on one of the two lobes. This branch is called the feedback branch, while the other branch is called the outcoupling branch. Thus, a highly reflective mirror can be used at the feedback side. A second mirror can be used at the outcoupling side. Since the gain in a semiconductor amplifier is sufficiently high this is not necessary.
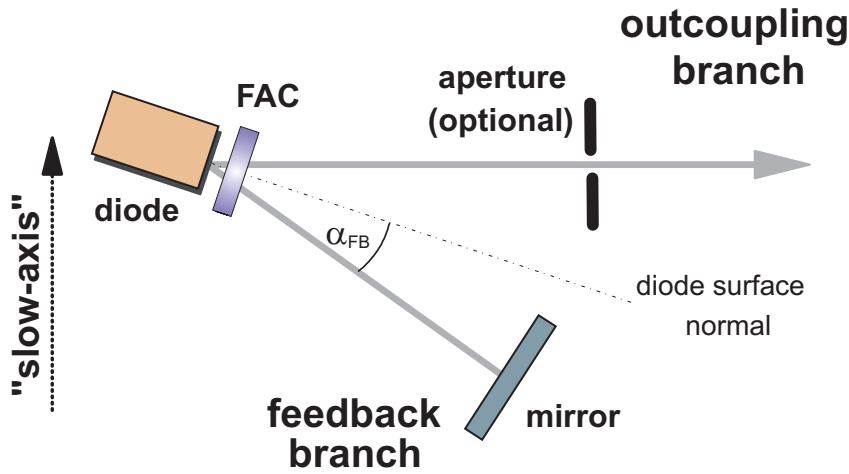
Figure 4.8: Asymmetric off-axis external cavity design without lenses in the slow-axis.

Comparison between standard BA and stripe-array amplifier: To resolve both lobes and for a better comparison to the measurements obtained in the previous section, a mirror with a partial reflectivity of 20% was used. The mirror was positioned in a distance of 40 mm from the front facet of the amplifiers. The resonator length was limited by the mechanical components. The lateral far-field distributions were measured with the *Beamscope*.

Figure 4.9 (a) shows the far-field intensity distribution using the standard BA amplifier at a feedback angle of $\alpha_{\mathrm{FB}} = 2.78°$. The characteristic double lobe emission was observed, whereas the outcoupling lobe has a higher intensity and the feedback lobe is suppressed. The outcoupling lobe had a far-field angle measured at full width at half maximum (FWHM) of $2\theta_0(\mathrm{FWHM}) = 1.5°$ corresponding to a beam propagation factor of $M_x^2 \approx 4.2$ for the 200 μm wide emitter. Despite the asymmetric intensity of the two lobes, the BA amplifier showed the same behavior for different feedback angles as with symmetric feedback (as shown in Fig. 4.6 in the previous subsection). Because of the low beam quality and the lack of angular susceptibility, the BA amplifier was not further investigated.

The far-field intensity distribution of the stripe-array at an injection current of 1.0 A is depicted in Fig. 4.9 (b) for three different feedback angles. In all three cases an asymmetric far-field was observed, with the lower intensity in the feedback lobe. The center wavelength was 972 nm with several spectral peaks. At a feedback angle of $\alpha_{\mathrm{FB}} = 2.78°$, the
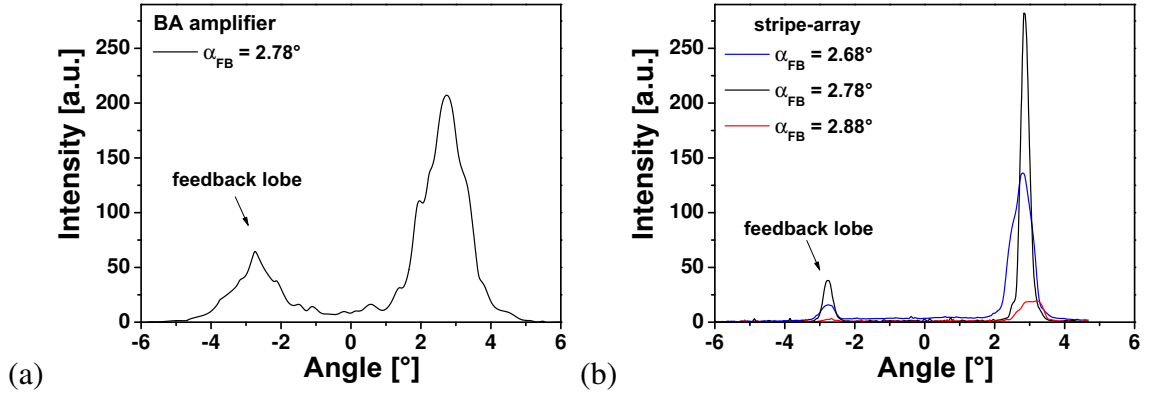
Figure 4.9: Far-field intensity distribution of (a) the BA amplifier and (b) the stripe-array amplifier with asymmetric off-axis feedback from a plane mirror at an injection current of 1.0 A.

highest intensity was measured. In this case, the far-field angle of the outcoupling lobe was $2\theta_0(\text{FWHM}) = 0.26°$. With the emitter size of 400 μm, this results in a beam propagation factor of $M_x^2 \approx 1.5$. This is nearly three times better than with the BA amplifier. At the two other feedback angles, the intensity drops and the width of the lobes broadened. If the feedback angle was decreased below $\alpha_{\text{FB}} = 2.68°$ or increased above $\alpha_{\text{FB}} = 2.88°$, no laser emission was observed. At a higher injection current of 1.5 A a similar behavior was observed. The ECDL could be operated at a larger angular range between $\alpha_{\text{FB}} = 2.54°$ and $\alpha_{\text{FB}} = 3.02°$. Since several peaks were present in the spectrum, the supermode could not be fully stabilized.

Power in central lobe and beam quality: Figure 4.10 (a) shows the measured far-fields of the outcoupling lobe for three different injection currents. By increasing the injection current, side lobes did arise next to the main outcoupling lobe. Furthermore, the far-field angle slightly increased. The peaks are referenced to the output powers that were measured in this single lobed beam. At 1.5 A, only small side lobes were present. At higher injection currents the side lobes in the background became stronger.

In Fig. 4.10 (b), the corresponding far-fields behind an adjustable rectangular aperture are depicted for the same operation conditions. The squares represent the measured data and the black solid lines are Gaussian fit curves through this data. The peaks of the far-fields are normalized to the measured power behind the aperture. The powers before and
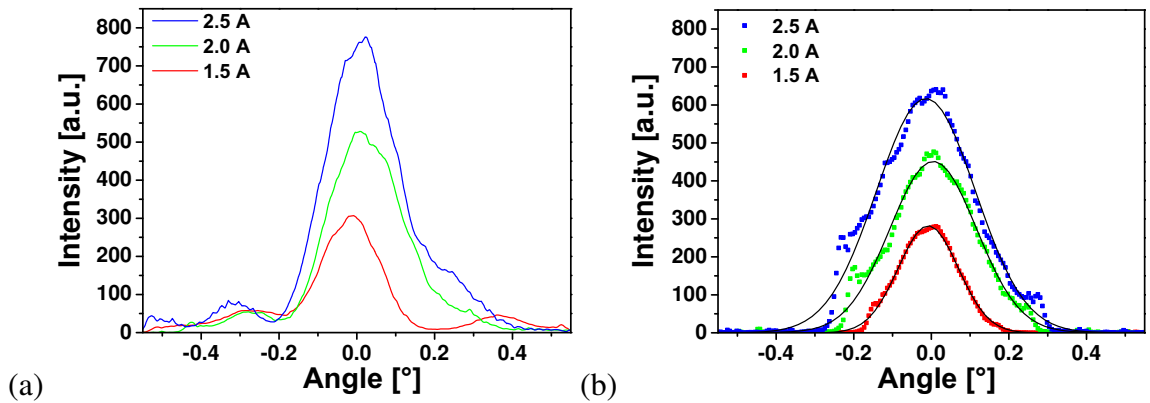
Figure 4.10: Far-field intensity distribution of the outcoupling lobe at different injection currents (a) without aperture and (b) with aperture.

behind the aperture and the corresponding measured M^2 values following the ISO standard are summarized in table 4.1. Furthermore, the beam propagation factors calculated from the far-field angles ($M^2_{x,\text{FWHM}}$) are given. The power in the side lobes reached values of nearly 20% at higher injection currents. If the beam quality is measured without aperture, the presence of the side lobes leads to too high values for M^2_x. In contrast the FWHM approximation is too optimistic if side lobes are present. Thus, the use of an aperture to select the central lobe and the ISO standard for measuring the beam quality will be used from hereon unless otherwise stated.

J[A]	P [mW] w/o aperture	P [mW] with aperture	M^2_x w/o aperture	M^2_x with aperture	$M^2_{x,\text{FWHM}}$
1.5	307	280	1.44	1.15	1.05
2.0	528	478	1.58	1.17	1.18
2.5	772	642	2.15	1.40	1.23

Table 4.1: Output power and beam propagation factors in the single lobe at the outcoupling side with and without the adjustable rectangular aperture.

4.3   Summary

In this chapter, the far-field emission behavior of a standard and a stripe-array amplifier with angular selective feedback was investigated by using two different external cavity designs. The two main results are:

- The stripe-array amplifier showed a preferred off-axis emission angle that matched to an out-of-phase coupling of adjacent emitters. This was predicted by the models described in the previous chapter and was also a result of the simulations. In contrast, the standard BA amplifier did not show such strong angular dependence and can be operated at arbitrary feedback angles.

- The spherical aberrations of the plano-convex lens alone were insufficient to build an off-axis external cavity, while the off-axis external cavity with the plane mirror had a high angular selectivity. This off-axis ECDL worked without apertures and slow-axis lenses.

Although a selection of the out-of-phase supermode of the stripe-array was achieved, the external cavities presented here did not feature wavelength selective elements. Thus, the individual emitters can operate at different wavelengths. Even though a coupling to the next neighbor can exist, a complete synchronization of the array to form a stable supermode can not be achieved without wavelength stabilization. However, the experimental investigations that were performed in this chapter confirm the assumptions made from the literature and the simulations. Thus, the theoretical and experimental results can be used as a basis for the design of an off-axis external cavity that comprises additional wavelength filters. This will be discussed in the subsequent chapter.

Chapter 5

Wavelength stabilized external cavity stripe-array amplifiers

Based on the simulations and the theoretical framework given in chapter 3, the techniques for transversal mode selection of BA and stripe-array amplifiers with off-axis external cavities have been investigated in the preceding chapter. The lateral modes of the stripe-array amplifier could be stabilized by supporting the out-of-phase supermode of the stripe-array. The standard BA amplifier did not show such a susceptibility to angular feedback. Thus, the experiments presented from hereon have only been performed using the stripe-array amplifier.

In this chapter, the investigation with external cavities is extended to the longitudinal mode selection and wavelength stabilization. The aim was to increase the stability of the coupling between the emitters of the stripe-array. The Littrow type external cavity was chosen because it could be easily adapted to the asymmetric off-axis feedback scheme described in the preceding chapter. Reflective diffraction gratings were chosen as wavelength selective elements. Because Bragg gratings such as volume Bragg gratings and reflective Bragg gratings can not provide a sufficiently large wavelength tuning range.

In the first section, an on-axis ECDL system is discussed. This ECDL did not comprise angular selectivity and was used to investigate the stripe-array emission characteristics with wavelength stabilized but arbitrary angular feedback. In the second section, wavelength stabilization with an off-axis external cavity will be presented. Furthermore, the experimental results are compared with numerical results.

5.1   On-axis ECDL

Experimental setup

The on-axis ECDL consisted of the stripe-array amplifier, an FAC, a cylindrical lens in direction of the slow-axis (slow-axis collimator - SAC) and a diffraction grating. A sketch of the external cavity setup is depicted in Fig. 5.1.

In direction of the fast-axis, a Littrow style resonator was realized (Fig. 5.2). In this direction, the emission of the stripe-array was nearly diffraction limited. The highly diverging light was collimated by the FAC with a high numerical aperture (NA > 0.9) and a focal length of $f_{\mathrm{FAC}} = 0.9$ mm. The collimated beam had a diameter of 2 mm and a residual divergence of $\theta \approx 0.4$ mrad. The grating was positioned with the grating lines parallel to the slow-axis. This resulted in wavelength selection along the fast-axis. In slow-axis direction,
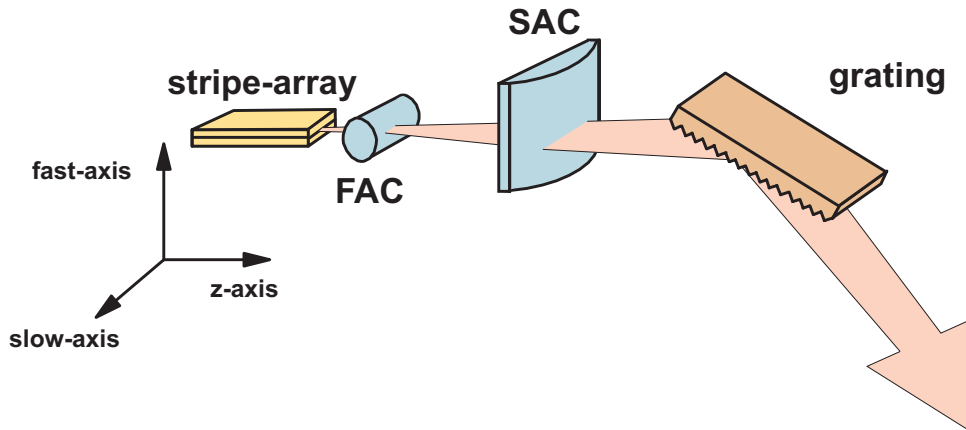
Figure 5.1: Schematic drawing of the on-axis stripe-array ECDL. FAC: fast-axis collimator, SAC: slow-axis collimator, grating with g = 1800 lines/mm. Outcoupling of the emission is managed via the zeroth diffraction order of the grating.

no wavelength selection was present and the grating did act similar to a plane mirror.

The diffraction grating was set up in a standard Littrow configuration, where the first order of diffraction is reflected back into itself. The angle between the surface normal of the grating and the first order of diffraction has to satisfy the Littrow condition $\lambda = d_G \cdot 2\sin\alpha_L$. The grating constant was g = 1800 lines/mm, giving a pitch of the grating lines $d_G = 0.55\,\mu$m. For a wavelength of $\lambda = 976.0$ nm, a Littrow angle of $\alpha_L = 62.5°$ was calculated. The well collimated light (fast-axis) was incident at the grating with an angle of 28.6°. Thus, approximately N = 7700 grating lines were illuminated. The wavelength resolution of the grating can then assumed to be $\Delta\lambda \approx \lambda/N$. This gives a theoretical grating resolution of $\Delta\lambda \approx 120$ pm.

The light emitted by the stripe-array was TE polarized with the electric field vector oscillating in the plane of the slow-axis. Thus, the light incident at the grating is polarized parallel to the grating lines. The diffraction efficiency of the grating for this polarization was determined to be $\approx 30\%$ and therefore, the zeroth diffraction order of the grating could be used to couple out the on-axis ECDL emission. The grating shows much higher diffraction efficiency of $> 90\%$ for light that is polarized perpendicular to the grating lines.
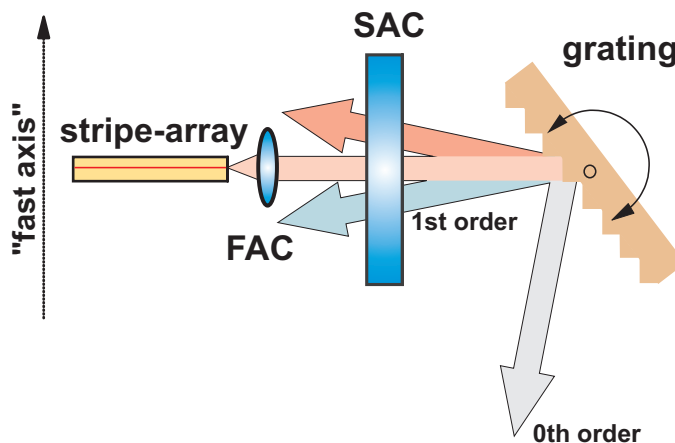
Figure 5.2: Schematic drawing of the on-axis ECDL in direction of the fast-axis. A standard Littrow setup is realized in this direction.

In slow-axis direction, the SAC collects nearly all light that is emitted by the amplifier. The lens transforms the angular distribution into a spatial distribution in the focal plane, where the grating is located. The grating can be treated as a plane mirror in slow axis direction. This means, that no angular selectivity is realized in slow-axis direction. Rather, nearly all slow-axis emission angles are supported by this external cavity. This allows the stripe-array to operate at any supermode. The possible array mode number is only limited by the NA of the SAC and the width of the grating. However, since the grating has a width of 5 mm this effect should be negligible.

Experimental results

Output power and beam quality: The optical output power of the on-axis ECDL is depicted in Fig. 5.3 as a function of the injection current. Two SAC lenses with different focal lengths have been used. With a focal length of f_{SAC} = 50 mm (NA ≈ 0.28), a laser threshold of 660 mA was observed. With this lens, a maximum output power of 6.8 W could be achieved at an injection current of 9 A. Up to an injection current of 8.5 A, the slope efficiency was determined to be 0.85 W/A. Above that injection current, a slight saturation behavior was observed, which indicates the onset of thermal rollover.

At an injection current of 4 A, an optical output power of 3.1 W was obtained. This equals to 89 % of the output power from a free running (and non AR coated) stripe-array diode laser. At this operating current, and an applied voltage of 1.4 V the electro-optical efficiency of the on-axis ECDL system still exceeded 55 %.
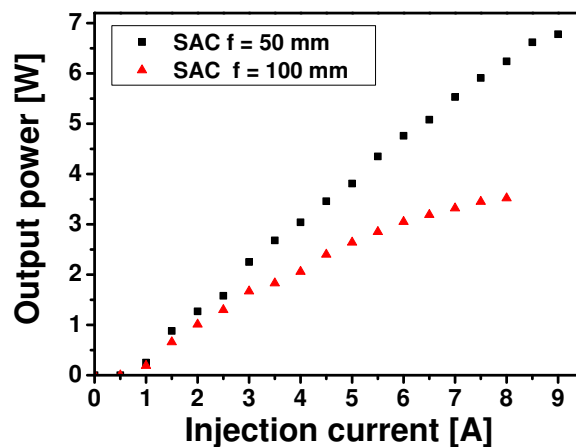
Figure 5.3: Optical output power of the on-axis ECDL emission as a function of the injection current for two different SAC lenses.

By using an SAC lens with a focal length of f_{SAC} = 100 mm (NA ≈ 0.14), the laser threshold was shifted to 700 mA. Furthermore, the resulting slope efficiency of 0.6 W/A was significantly lower compared to the shorter resonator. At an injection current of 8 A, a maximum output power of 3.5 W was measured. At 4 A, an output power of 2 W could be achieved. This corresponds to approximately 60 % of the output power of the free running stripe-array diode laser. With this SAC lens, the on-axis ECDL emission showed saturation behavior above 5 A and the slope efficiency diminished drastically at higher injection currents. This is presumably caused by the lower numerical aperture of the slow-axis lens with the longer focal length. Additionally, the higher losses inside the cavity with f = 100 mm lead to a stronger heating of the laser chip. Therefore, the onset of thermal

rollover was shifted to lower injection currents. In both experiments, the injection current was increased until the first sign of saturation to avoid a damage of the stripe-array amplifier.

Because of the better performance of the on-axis ECDL using the SAC with a focal length of $f_{SAC} = 50$ mm, all further investigations have been performed with this lens.

The caustic of the beam along the slow-axis is depicted in Fig. 5.4. At an injection current of 9 A and an optical output power of 6.8 W, a slow-axis beam propagation factor of $M_x^2 < 35$ was measured. In direction of the fast-axis a beam propagation factor of $M_y^2 < 1.3$ was obtained.
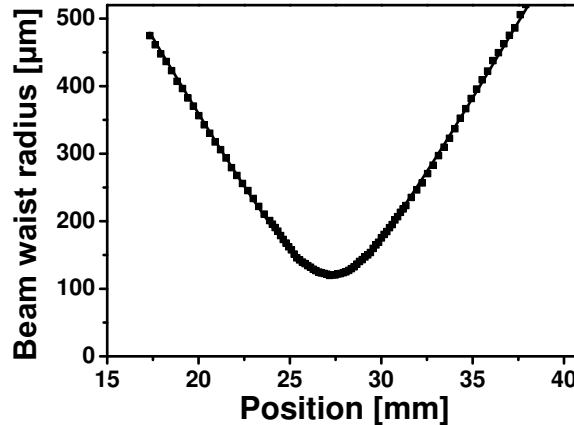
Figure 5.4: Caustic of the on-axis ECDL emission in the slow-axis at an injection current of 9 A.

Spectrum and tuning range: Figure 5.5 shows the spectrum of the on-axis ECDL emission measured with an optical spectrum analyzer (OSA) at the maximum optical output power of 6.8 W. At a center emission wavelength of 967 nm, a bandwidth of 100 pm (FWHM) and a side mode suppression of nearly 45 dB could be achieved. Compared to the free running diode laser without AR-coating and external cavity, the bandwidth could be reduced by a factor of about 20.
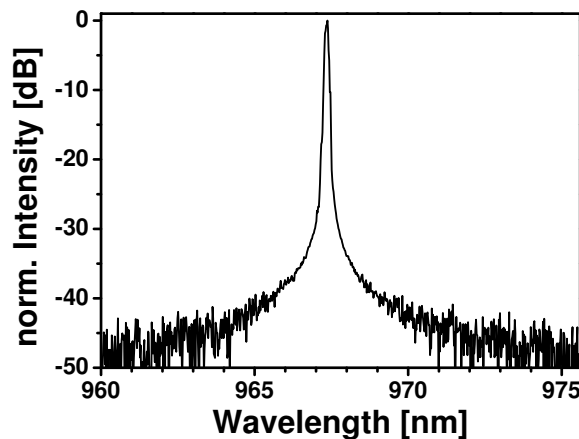
Figure 5.5: Spectrum of the on-axis ECDL emission at an injection current of 9 A measured with an optical spectrum analyzer.

By tilting the grating and changing the Littrow angle, it was possible to tune the center wavelength of the emission. The optical output power of the on-axis ECDL as a function of the emission wavelength is depicted in Fig. 5.6. The ECDL emission was tunable over a

range of 40 nm from 950 nm to 990 nm. At an injection current of 4 A, more than 2.5 W of optical output power where obtained and the emission wavelength was tunable from 952 nm to 980 nm. A power of more than 3 W was measured between 950 nm and 986 nm at 6 A injection current while the maximum output power was obtained around 970 nm.
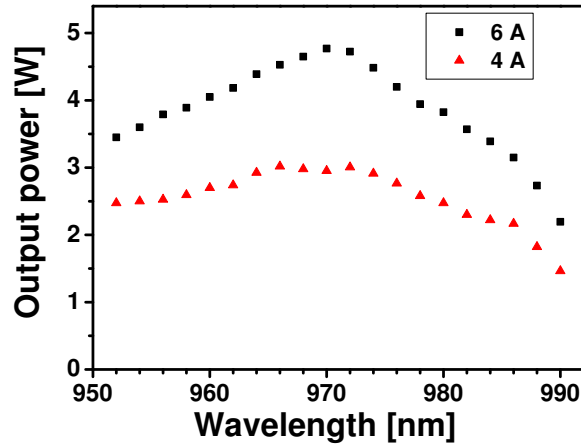
Figure 5.6: Optical output power of the on-axis ECDL as a function of the emission wavelength for two different injection currents.

Discussion

With the stripe-array amplifier operated in an on-axis Littrow external cavity, narrow bandwidth laser emission with a cw output power of up to 6.8 W could be achieved. The bandwidth of the emission was measured to be below 100 pm (FWHM) and it was possible to tune the laser emission wavelength over a range of 40 nm. Compared to the free running stripe-array diode laser, the spectral width was reduced by a factor of 20. A low laser threshold and a high slope efficiency of 0.85 W/A was achieved. However, the output power decreased to 89 % compared to the free running stripe-array diode laser. The electro-optical efficiency was higher than 50 % in all cases.

Beam propagation factors of $M_x^2 < 35$ and $M_y^2 < 1.3$ have been measured at the maximum output power and a brightness of 15.6 MW/cm^2·str was determined. The poor lateral beam quality is owed to the lack of angular selectivity of the on-axis external cavity design. Thus, this ECDL can not be used as pump laser for nonlinear frequency conversion. However, the investigation of the stripe-array with wavelength stabilization and without angular selective feedback is useful for the interpretation of the results obtained with the off-axis ECDL that will be described in the next section.

A possible application of the on-axis ECDL is the pumping of advanced solid state lasers or alkali vapor lasers (like rubidium, cesium or potassium lasers). In this case, wavelength stabilized, narrow bandwidth emission with cw output powers of a few Watt is required and the raw optical output power is more important than the beam quality of the laser emission.

Usually, ECDLs comprising volume Bragg gratings have been used for this purpose. Gourevitch et al. achieved narrow bandwidth emission below 100 pm and a cw output power of 2 W with a single BA diode laser [71]. However, the tunability of volume Bragg gratings is constricted. Wang et al. could realize an output power of 2.3 Watts, a bandwidth of 70 pm and a tuning range of 1.6 nm by operating a BA diode laser array of three uncoupled 200 μm emitters in a Littman-Metcalf style ECDL [72].

Higher output powers were demonstrated with BA diode laser bars. Gourevitch et al. used a laser bar with 24 emitters each with a width of 150 μm stabilized with a volume Bragg grating and were able to obtain $\approx$ 30 W of cw emission at an injection current of 50 A [73]. Liu et al. realized 12.5 W of output power at an injection current of 50 A by operating a laser bar with 49 emitters each with a 100 μm aperture in a Littrow type ECDL [74].

In conclusion, the results obtained with the on-axis ECDL represent the highest bandwidth narrowed output power achieved with a (single element) BA or stripe-array diode laser.

5.2   Off-axis ECDL

The on-axis stripe-array ECDL described in the preceding section yielded high output power, wavelength stabilized emission with narrow bandwidth and a large wavelength tuning range. However, the beam quality of the slow-axis emission remained poor because the stripe-array was not operated at a specific angle to stabilize a certain array supermode. Therefore, the resulting brightness was insufficient for nonlinear application.

In this section, a new off-axis external cavity scheme with a tilted diffraction grating is presented. This design is based on the investigations made with a plane mirror as described in subsection 4.2.2. This scheme was extended with the fast-axis Littrow setup described in the previous section to achieve a stable coupling of the array emitters.

Experimental setup

The experimental setup of the off-axis ECDL is depicted in Fig. 5.7. The cavity consisted of the stripe-array amplifier, an FAC, a half wave plate and a holographic reflective diffraction grating (g = 1800 lines/mm). The grating was placed with the grating lines parallel to the slow-axis, following the scheme used with the on axis resonator (Fig. 5.2). Thus, a standard Littrow setup was realized in direction of the fast-axis direction, while the grating did act similar to a plane mirror for the slow-axis. The main difference to the standard Littrow setup was that the outcoupling was not managed via the zeroth order of diffraction of the grating. Instead, a half wave plate was used to rotate the polarization of the electric field emitted by the stripe-array by 90°. Thus, the light incident at the grating is polarized perpendicular to the grating lines. In this case, the diffraction efficiency was > 90% and the reflection into the zeroth order of diffraction was minimized. Outcoupling of the diode laser emission was realized similar to the scheme described in section 4.2.2. While feedback was provided on one of the lobes, outcoupling of the usable light was realized on the other lobe.

This external cavity is best described by treating both axes separately. In fast-axis direction, wavelength stabilization and bandwidth narrowing was realized. Each emitter is stabilized on the same wavelength resulting in a wavelength synchronization of the stripe-array. By tilting the grating, the Littrow angle is changed and the emission wavelength can be tuned. The resolution of the Littrow cavity is about the same as with the on-axis ECDL (see page 42).

In slow-axis direction, the grating possesses no wavelength selectivity. Thus, it can be used to select the feedback angle α_{FB} in the same way as with a plane mirror. Depending on the slow-axis tilting angle, a specific supermode of the stripe-array amplifier is supported by the resonator. The length of the resonator was not limited by the focal length of a lens
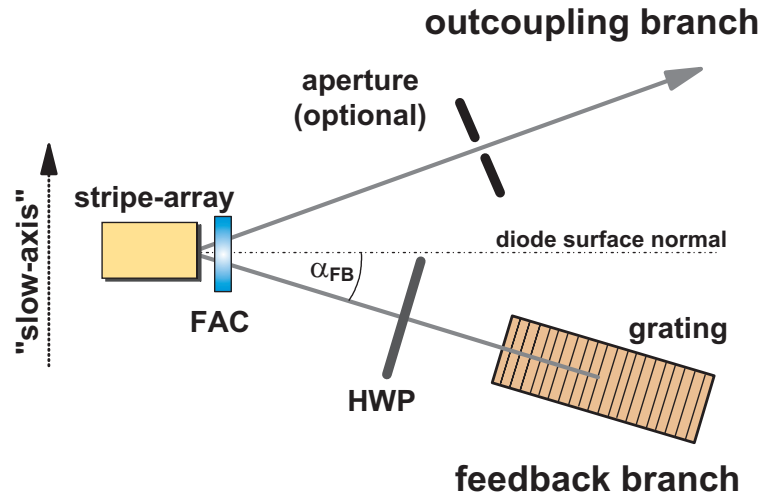
Figure 5.7: Schematic drawing of the off-axis stripe-array ECDL in plane of the slow-axis. FAC: fast-axis collimator, HWP: half wave plate.

and the shortest cavity length that could be realized was 40 mm, mainly limited by the mechanical components.

5.2.1   Lowest order out-of-phase supermode

In the previous chapters, the stripe-array amplifier was investigated both experimentally and theoretically. The simulations and experiments showed a preferred operation in the lowest order out-of-phase supermode, which corresponds to an off axis angle of 2.8°for $\lambda = 976$ nm. In this case, neighboring emitters will oscillate with a phase shift of π. The supermode number is equal to the number of emitters $N =40$. The experimental investigations performed in chapter 4, corroborate this behavior. The stripe-array amplifier showed a distinct preference to this specific feedback angle. In this subsection, the off-axis external cavity was setup at a feedback angle $\alpha_{FB} =2.8°$ to operate the amplifier at its "native" out-of-phase supermode.

Output power with and without aperture: The output power of the off-axis ECDL emission with and without aperture in the outcoupling branch is depicted in Fig. 5.8 for the feedback angle set to support the lowest order out-of-phase supermode. The laser threshold was 740 mA. Without aperture (represented by the squares in the graph), a maximum output power of 2060 mW was achieved at an injection current of 4.1 A.

Up to an injection current of 2.5 A, the slope efficiency was 0.75 W/A. Above 2.5 A, the slope decreased to 0.58 W/A. This kink in the light current characteristic indicates the onset of higher order transversal mode operation.

The circles in the graph represent the output power measured with the on-axis ECDL to have a figure of merit of the off-axis device. Compared to the on-axis ECDL the off-axis ECDL showed a higher threshold and a decrease of the slope efficiency by 13%. Furthermore, the onset of thermal rollover was shifted from more than 8 A to about 4 A. The electro-optical efficiency achieved with the off-axis ECDL was 35% at an injection current of 4.0 A.

As described in subsection 4.2.2, an additional aperture can be used at the outcoupling branch to suppress amplified spontaneous emission and higher order transversal modes.

Figure 5.8: Optical output power of the off-axis ECDL emission for the lowest order out-of-phase supermode as a function of injection current with and without mode aperture in the outcoupling branch.

The aperture was adjusted to block all emission except the central far-field lobe as depicted in Fig. 4.10 on page 39.

The output power measured behind this aperture is represented by the crosses in Fig. 5.8. The laser threshold remained at 740 mA. At an injection current of 3.7 A, a maximum output power of 1160 mW was achieved. Up to an injection current of 2.5 A, the slope efficiency was 0.55 W/A. The lower slope efficiency is simply caused by the blocking of the light emitted in higher modes and amplified spontaneous emission. Above an injection current of 2.5 A, a the slope efficiency drops to 0.35 W/A and the slope efficiency nearly flattens above an injection current of 3.2 A.

While the laser output power without aperture saturated at injection currents of about 4 A, the power in the central lobe saturates at lower injection currents. The saturation at 4 A is caused by thermal rollover. The onset of thermal rollover is shifted to lower injection currents compared to the on-axis ECDL described in the previous section because of the threshold shift from 660 mA to 740 mA. Thus, more heat is dissipated in the active region which is also indicated by the lower slope efficiency. However, the saturation of the output power in the central lobe is caused by the fact that more power is emitted into the side lobes.

Beam quality and brightness: The beam propagation factors measured with and without aperture in slow axis direction are shown in Fig. 5.9 (a) as a function of the injection current. Both curves show increased M_x^2 values for higher injection currents. Without the aperture (represented by the black squares), higher M_x^2 values than with aperture (crosses) are measured as expected. Furthermore, the kink in the curve indicates the presence of higher modes at about 2.2 A. A beam propagation factor of $M_x^2 \approx 4.3$ was measured at an injection current of 4.2 A.

The beam propagation factors measured behind the apertures for the different injection currents corresponding to the power measurement are depicted in Fig. 5.9 (a) in slow-axis direction and (b) in fast-axis direction.

With the aperture, the M_x^2 values increased more linearly. Near threshold (0.8 A), a beam propagation factor in slow-axis direction of $M_x^2 \approx 1.1$ was measured. Above 2.2 A injection current the slope of the M_x^2 values did slightly increase. At an injection current of 4.2 A values of $M_x^2 \approx 2.4$ have been measured.
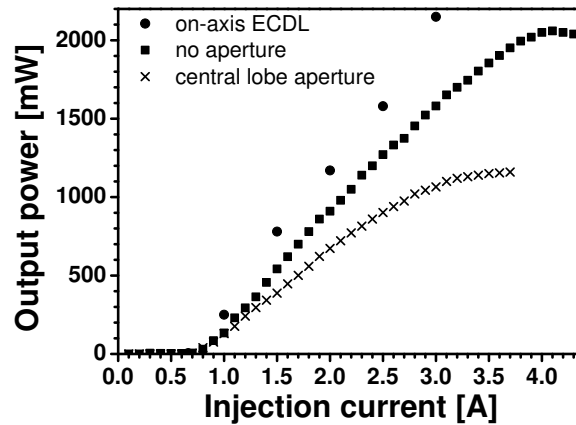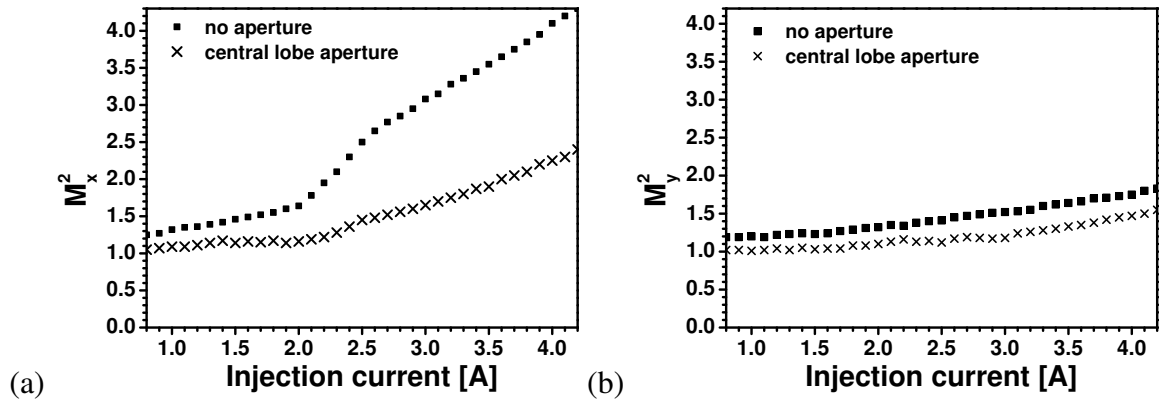
Figure 5.9: Beam propagation factors of the off-axis ECDL emission for the lowest order out-of-phase supermode as a function of injection current measured with and without aperture for (a) the slow-axis and (b) the fast-axis.

The beam propagation factors measured in the fast-axis direction are depicted in Fig. 5.9 (b). Slightly above threshold at an injection current of 0.8 A, values of $M_y^2 \approx 1.2$ were obtained without aperture. Up to an injection current of 4.2 A, a linear increase of the beam propagation factors to values of $M_y^2 \approx 1.9$ was observed. With the aperture, a linear degradation of the beam quality from $M_y^2 \approx 1.02$ to $M_y^2 \approx 1.25$ was measured.

Since the beam quality measuring technique using the ISO standard overweights side lobes as can be seen in the kink in Fig. 5.9 (a), all power and beam quality measurements presented from hereon have been measured behind the aperture.

To get a more transparent picture of the off-axis ECDL performance, the brightness values have to be compared. In Fig. 5.10, the calculated values for the brightness with aperture are depicted. The brightness did increase linearly up to injection currents of about 2.0 A. Between 2.1 and 2.9 A, a diminished slope was observed. At higher injection currents than 3.0 A, the brightness rather decreased. This is attributed to both, the degradation of the beam quality and the saturation of the power transmitted through the aperture at higher injection currents.
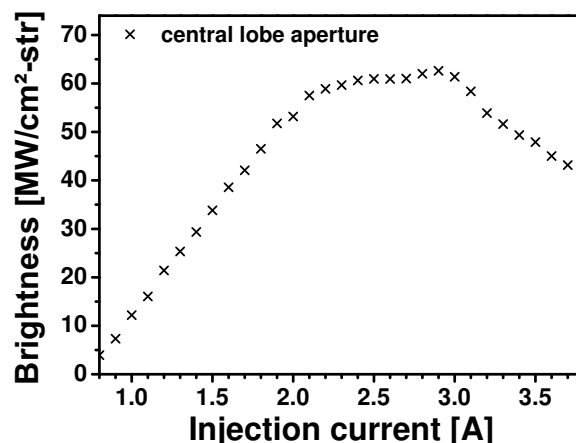
Figure 5.10: Calculated brightness of the off-axis ECDL emission as a function of the injection current.

The maximum brightness of $B = 62.5$ MW/cm^2-str was achieved at an injection current of 2.9 A, where the ECDL yielded emission with a power of 1044 mW. The caustics of the off-axis ECDL emission for both axes measured at this operating point are shown in
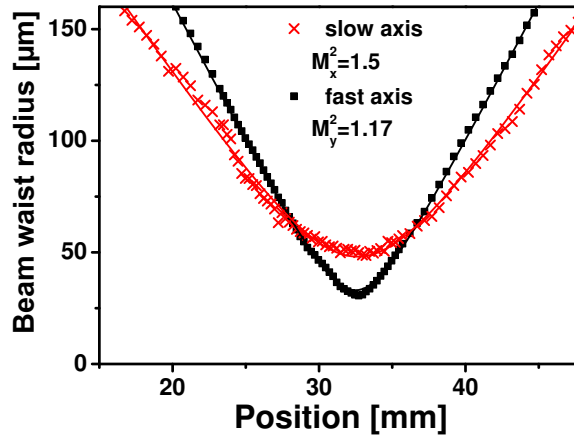
Figure 5.11: Beam caustics for the fast-axis and the slow-axis at an injection current of 2.9 A.

Fig. 5.11. Beam propagation factors of $M_x^2 = 1.5$ in slow-axis (crosses) and $M_y^2 = 1.17$ in fast-axis (squares) were determined. Compared to the free running diode laser with a slow-axis beam propagation factor of $M_x^2 > 60$, the beam quality was improved by a factor of 40. The electro-optical efficiency of the off-axis ECDL at this operating point was 38% for the power measured without aperture. However, the power in the central lobe was 70% from the overall power giving an electro-optical efficiency of 26.5%.

Influence of the resonator length: As stated before, the length of the external cavity was limited to 40 mm by the mechanical components. However, the emission of such an ECDL can depend strongly on the cavity length. In Fig. 5.12 the output power of the off-axis ECDL emission as a function of the injection current is depicted for three different resonator lengths. The measurement was performed with aperture in the outcoupling branch. By increasing the distance between the grating and the diode laser, the laser threshold was shifted to higher injection currents and the slope efficiency was decreased. At 60 mm length the laser threshold was 760 mA and a maximum output power of 800 mW could be achieved. At a resonator length of 80 mm, a threshold of 800 mA was observed and the output power was 650 mW. Furthermore, saturation effects came into play which is caused by thermal effects. Thus, the off-axis ECDL was investigated further with the shortest possible length of 40 mm.
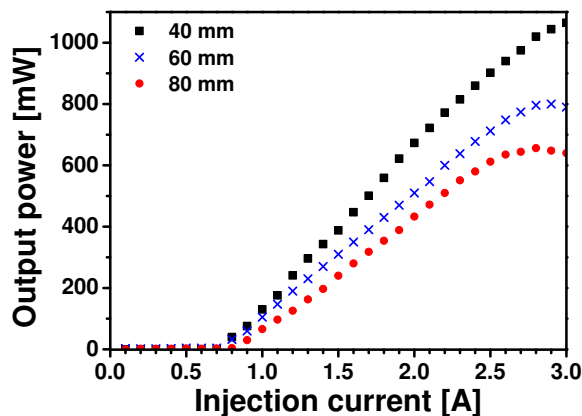
Figure 5.12: Optical output power for three different resonator lengths of the off-axis ECDL as a function of injection current measured behind the aperture.

Spectrum and tunability: By changing the Littrow angle of the grating, the center wavelength of the ECDL emission could be tuned. Figure 5.13 (a) shows the optical output power of the off-axis ECDL emission as a function of the wavelength for four different injection currents. At 2.0 A, the maximum of the output power is centered around 970 nm and shifts to lower wavelengths with higher injection currents. A tuning range of 35 nm at FWHM from 953 nm to 988 nm could be achieved at an injection current of 2.7 A. The total tuning range was 50 nm from 945 nm to 995 nm.

(a)   (b)
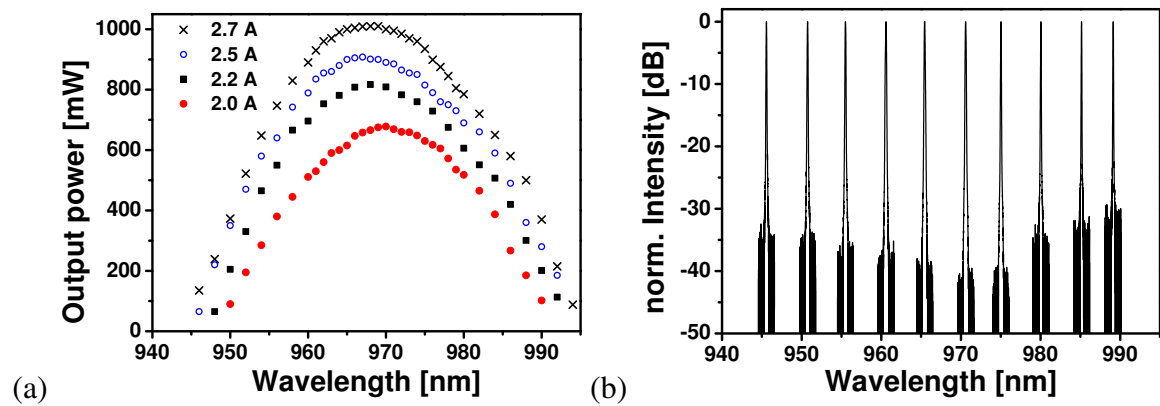
Figure 5.13: (a) Optical output power as a function of the center wavelength for four different injection currents. (b) Normalized spectra for different center wavelengths at an injection current of 2.5 A.

Figure 5.13 (b) shows the normalized spectra at different center wavelengths at 2.5 A injection current corresponding to the tuning curve. The spectra have been measured with an OSA. Even at the edges of the tuning curve the side mode suppression was well above 30 dB. In all cases, bandwidths around 50 pm (FWHM) were obtained, which equals the resolution limit of the used OSA.

A single spectrum close to the gain maximum at 969 nm is depicted in Fig. 5.14 (a). At an injection current of 2.9 A, an optical output power of 1044 mW was measured. A side mode suppression of better than 45 dB and a bandwidth of 50 pm was observed. By using a Fabry Perot interferometer (FPI) with a free spectral range (FSR) of 8 GHz, a bandwidth of < 80 MHz was measured. This is well below the resolution limit of the OSA and near the resolution limit of the FPI.

(a)   (b)
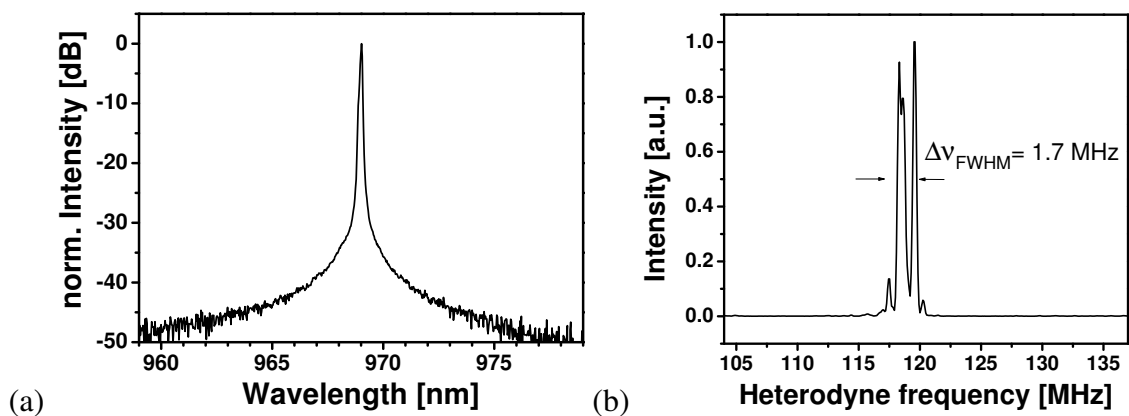
Figure 5.14: (a) Optical spectrum of the off-axis ECDL emission at an injection current of 2.9 A. (b) Beat signal of ECDL and reference laser ($\Delta\nu_{REF} = 1$ MHz) emission [75].

For further investigation of the bandwidth, a heterodyne interference analysis was performed. In this experiment the emission of a reference laser with a known bandwidth of $\Delta\nu_{\mathrm{REF}} = 1$ MHz (*SACHER LASERTECHNIK* TEC 300-960-500) was used to interfere with the emission of the off-axis ECDL. The beat signal depicted in Fig. 5.14 (b) was detected using a photo diode and an electronic spectrum analyzer with a resolution of 40 kHz at a measuring time of 1 ms (40 MHz/ms).

The beat signal had a width (FWHM) of $\Delta\nu_{\mathrm{BEAT}} = 2$ MHz. By the known bandwidth of the reference laser $\Delta\nu_{\mathrm{REF}} = 1$ MHz, this results in a bandwidth of $\Delta\nu_{\mathrm{ECDL}} = 1.73$ MHz for the ECDL emission. The measurement was made at an injection current of 2.9 A. Compared to the free running diode with a bandwidth about 2 nm, this is an improvement by five orders of magnitudes.

Near and far-field distribution: To obtain the near and far-field distributions, a pellicle beam splitter was inserted into the ECDL. The near-field patterns were obtained by imaging the front facet onto a CCD camera and the far-field distributions were measured with the moving slit of the *Beamscope*.

The far-field intensity distribution of the off-axis ECDL at an injection current of 2.5 A is shown in Fig. 5.15 (b). The typical double lobed emission with two peaks at $\alpha_{\mathrm{FB}} = \pm 2.8°$ can be seen. As typical for asymmetric off-axis feedback, the feedback lobe is suppressed while the outcoupling lobe has a higher intensity. The feedback side is located on the left in both graphs, respectively.

The corresponding near-field distribution is depicted in Fig. 5.15 (a). The feedback angle of $\alpha_{\mathrm{FB}} = 2.8°$ corresponds to the lowest order out-of-phase supermode which has the mode number $L = N$, whereas $N = 40$ is the number of emitters. Here, 38 emitters of the 40 emitters could be resolved which is presumably caused by the optical imaging system that was used.

(a)   (b)

Figure 5.15: (a) Far-field and (b) near-field intensity distribution of the off-axis ECDL operated at the lowest order out-of-phase supermode.

5.2.2   Second order in-phase supermode

Following the discussion about array modes provided in chapter 3, other array supermodes than the "native" lowest order out-of-phase supermode can be selected. Hadley et al. studied higher supermodes by injection locking [76]. However, if an array supermode is selected that does not provide a phase shift of $m_{order} \cdot \pi$ between adjacent emitters, whereas m_{order} is an integer, no satisfying results have been obtained. Thus, most studies of these arrays have

been concentrated on the lowest order in-phase and out-of-phase supermode. Nevertheless even higher array supermodes are possible as demonstrated by Epler et al. [77].

A special case is the second order in-phase supermode, whereas the mode number is $L = 2 \cdot N$. This mode is investigated in this subsection. In this case, a phase shift of $\Delta \phi = 2\pi$ between the neighboring emitters is present. For the stripe-array amplifier with an emission wavelength of 976 nm used in this work, this supermode corresponds to a feedback angle of α_{FB} =5.6° .

Output power and beam quality: The output power of the off-axis ECDL emission measured without aperture in the outcoupling branch is depicted in Fig. 5.16 for two different feedback angles. The squares in the graph represent the lowest order out-of-phase supermode as discussed before. The triangles represent the powers obtained with feedback angle set to support the second order in-phase supermode. Compared to the smaller angle, the threshold was shifted by 150 mA to 890 mA. Furthermore, the slope efficiency of 0.65 W/A was lower and the ECDL showed thermal rollover at about 2.3 A. A maximum output power of 700 mW could be achieved at 2.4 A.

In this case, 450 mW were concentrated in the central lobe. With aperture, beam propagation factors of $M_x^2 = 1.58$ in slow-axis and $M_y^2 = 1.15$ in fast-axis have been measured. This gives a brightness of 26.1 MW/cm^2-str which is more than two times lower than with the smaller feedback angle.
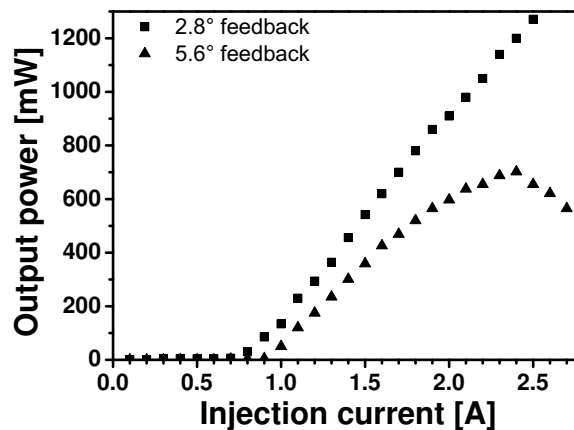
Figure 5.16: Optical output power of the off-axis ECDL emission for two different feedback angles.

The spectral behavior was about the same as with the smaller angle. At 2.4 A, the wavelength was tunable between 940 nm and 990 nm and bandwidths below 50 pm have been determined with the OSA.

Near and far-field distribution: The far-field distribution of the off-axis ECDL is depicted in Fig. 5.17 (a) at an injection current of 2.5 A. The typical double lobed emission with two peaks at α_{FB} =±5.6° was observed. As typical for asymmetric off-axis feedback, the feedback lobe was suppressed while the outcoupling lobe had a higher intensity. The feedback branch was located on the left side in both graphs, respectively.

The corresponding near-field distribution is shown in Fig. 5.17 (b). The feedback angle of α_{FB} =5.6° corresponded to the second order in-phase supermode or the mode number $L = 2 \cdot N$. In the near-field, 76 emitters could be resolved which corresponds to approximately an emitter number of $2 \cdot N$. The measured intensity distribution with this feedback angle was more asymmetric than in the lowest order out-of-phase supermode operation.
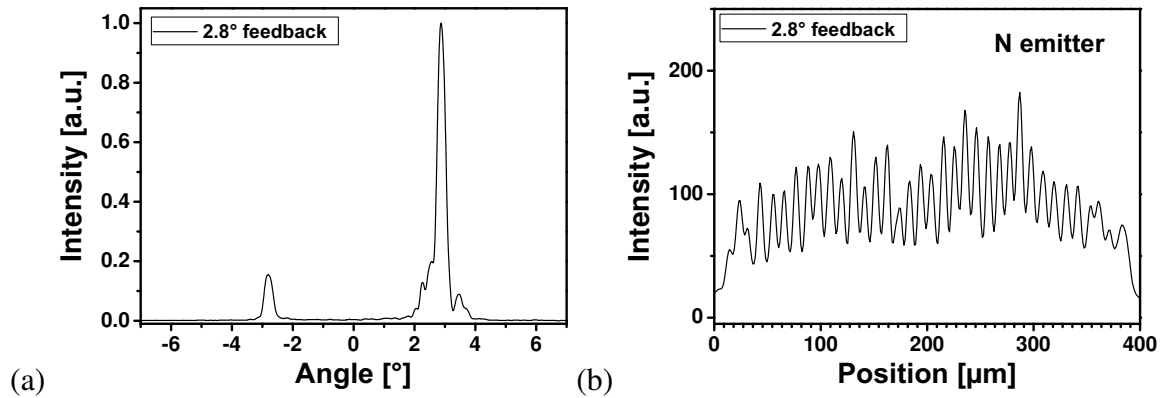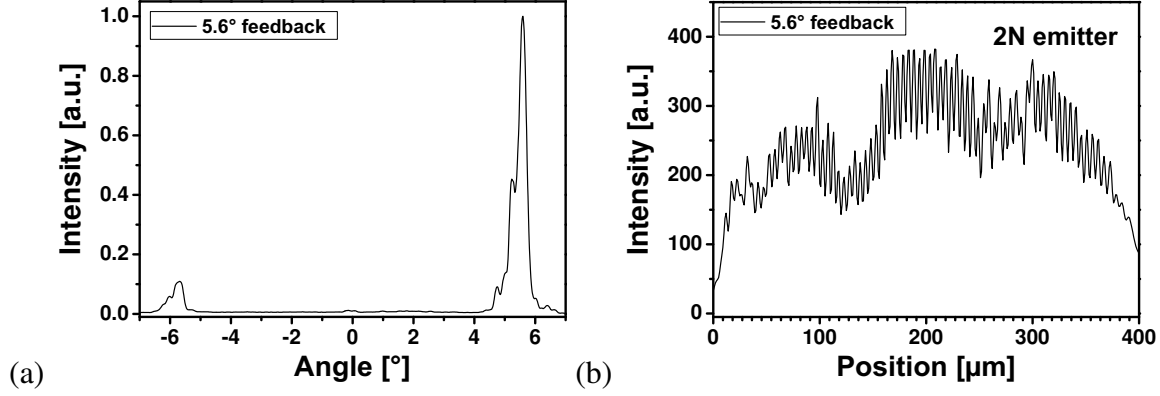
Figure 5.17: (a) Far-field and (b) near-field intensity distribution of the off-axis ECDL operated at the second order in-phase supermode.

5.2.3 Modeling the off-axis ECDL

External cavity feedback model: For the modeling of the off-axis ECDL, the same model that was used for the simulation of the stripe-array diode laser has been applied. This model includes a direct time domain numerical approach, which treats the gain guided stripe-array as a broad-area resonator whose optical properties are modified by the injection of carriers into each stripe. A traveling wave equation for two counterpropagating forward $(+)$ and backward $(-)$ complex waves $E^{\pm}(t, z, x)$ along the propagation z direction was used.

The model includes field diffraction along the lateral x axis (slow-axis). The effective index method has been used to provide an effective refractive index in the (x, z) plane. To model the carrier density profile and therefore the gain and index profiles along the longitudinal z and lateral x plane, a carrier density equation including lateral carrier diffusion was used. A Lorentzian gain dispersion was assumed in the modeling with an effective polarization equation. Heating due to the injection of carriers at the contact stripes locations is included. The equations and parameters used for the simulations can be found in section 3.2, where this model was used to simulate the stripe-array as diode laser (without AR coated front facet).

To take into account the external off-axis feedback from the grating, it was assumed that the optical field is reflected from a infinite plane mirror located at a distance of $D_m = 40$ mm which is tilted by the angle α_{FB}. The optical field $E_{FB}(t, x_0)$ is reinjected into the stripe-array through the front facet at a time t. The lateral input coordinate x_0 is calculated by using the Fresnel integral:

$$E_{FB}(t, x_0) = \sqrt{\frac{1}{i\lambda_0 2D}} \int_{-w/2}^{w/2} E^{+}(t - \tau, l, x) e^{-i2\pi \frac{\mathrm{dist}(x, x_0)}{\lambda_0}}\, dx. \qquad (5.1)$$

Here, $\tau = \frac{2D_m}{c_0}$ is a fixed time delay given by the grating distance, λ_0 is the central wavelength, l is the length and w the width of the stripe-array amplifier. The term $\mathrm{dist}(x, x_0)$ represents the shortest distance between two lateral points x and x_0 at the front facet of the stripe-array which the light takes to travel via the reflection from the grating plane.

A first order approximation $\mathrm{dist}(x, x_0) \approx 2D_M + (x + x_0)\sin\alpha_{\mathrm{FB}}$ that neglects higher order terms of order $\left(\frac{x}{2D_M}\right)^2 \ll 1$ was used. The wavelength selectivity of the grating is modeled by applying a Gaussian spectral filter to the delayed time sequence $E_{FB}(t - \tau, x_0)$.

A bandwidth of $\Delta\lambda = 0.1$ nm was used in the simulations. Such a narrow spectral filter was required to obtain a stable single compound cavity mode CW operation.

Numerical results: With this model, the two cases of off-axis feedback to support the lowest order out-of-phase mode and the second order in-phase mode were simulated.

Figure 5.18 (a) shows the calculated near-field distributions over the whole width of the stripe-array for a feedback angle of $\alpha_{FB} = 2.8°$. The phases of all emitters are depicted in Figure 5.18 (b).

The near-field intensity distribution is relatively homogeneous showing ≈ 40 intensity maxima with a nearly flat profile and equal comparable amplitudes. Just the outer emitters have a slightly lower intensity than the inner emitters and a slight asymmetry due to the asymmetric feedback can be guessed. Compared to the measured near-fields presented in the last section (Fig. 5.15 (b)), the simulation showed very good qualitative agreement.

In Fig. 5.18 (c) the near-field distribution for four stripes of the same simulation is zoomed in. The gray bars in this graph represent the contact stripes where the carriers are injected through. The simulations show, that the field is concentrated underneath the stripes.

In Fig. 5.18 (d) the phases are zoomed in for four of the stripes. A phase shift of π between the fields concentrated underneath the emitters can be observed. This agrees well with the supermode theory discussed in section 3.1.2, since the supermode $L = 40$ should lead to a coupling of the emitters with a $\Delta\phi = \pi$ phase shift.

In Fig. 5.19 (a), the corresponding calculated near-field distributions for a feedback
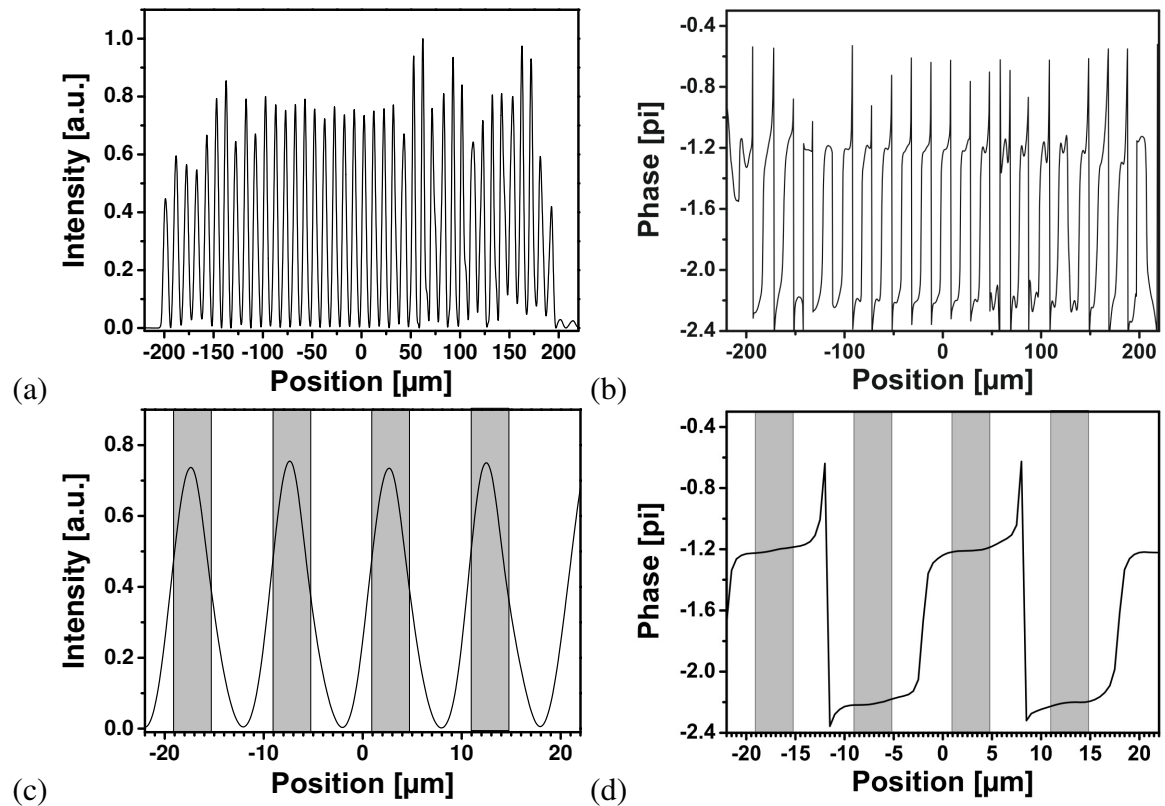
Figure 5.18: Calculated near-field intensity distribution (a) and phases (b) for the lowest order out-of-phase mode $\alpha_{FB} = 2.8°$ for all 40 stripes, (c) shows the near-field intensity distribution and (d) the phases for four of the stripes. The vertical bars indicated the location of the contact stripes. (With permission of M. Lichtner)

angle of $\alpha_{\mathrm{FB}} = 5.6°$ are shown. Here, the near-field profile is not homogeneous and possesses varying amplitudes with a dip where the light is reinjected. In good agreement to the measurement shown in Fig. 5.17 (b), ≈ 80 intensity maxima were found.

In Fig. 5.19 (c), four stripes are zoomed in. For this feedback angle, the field is not fully concentrated underneath the stripes. Rather, a strong field maximum is located between the contact stripes. Thus, the presence of leaky waves and a strong antiguiding effect leads to the creation of a virtual emitter between the physical contact stripes. The consequence is the bisection of the emitter distance and the doubling of the number of field maxima compared to the number of contact stripes.

The zoomed in graph for the phases (Fig. 5.19 (d)) show a phase shift of $\Delta\phi = 2\pi$ between the fields beneath the contact stripes. However, neighboring emitters (or field maxima, respectively) are lasing with a π phase shift. Since the distance between the field maxima is halved, the angle of the farfield peaks is doubled as in the experiment. At $\alpha_{\mathrm{FB}} = 5.6°$, not all field maxima are located exactly beneath the pumped regions. Thus, the area of the emitters divided by the area of the stripes is reduced and the conversion of carriers into photons is reduced due to stimulated recombination and spatial hole burning. Correspondingly, an optical power drop of about 50% was observed in the simulations which also agrees with the measured data.

The calculated far-fields are shown in Fig. 5.20 (a) for $\alpha_{\mathrm{FB}} = 2.8°$ and (b) for $\alpha_{\mathrm{FB}} = 5.6°$. As expected by the theory and the measurements feedback and off-axis angle are the same and both calculated far-fields show the characteristic asymmetric distribution. The lower

(a)

(b)

(c)

(d)

Figure 5.19: Calculated near-field intensity distribution (a) and phases (b) for the second order in-phase mode ($\alpha_{\mathrm{FB}} = 5.6°$) for all 40 stripes, (c) shows the near-field intensity distribution and (d) phases for four of the stripes. The vertical bars indicated the location of the contact stripes. (With permission of M. Lichtner)
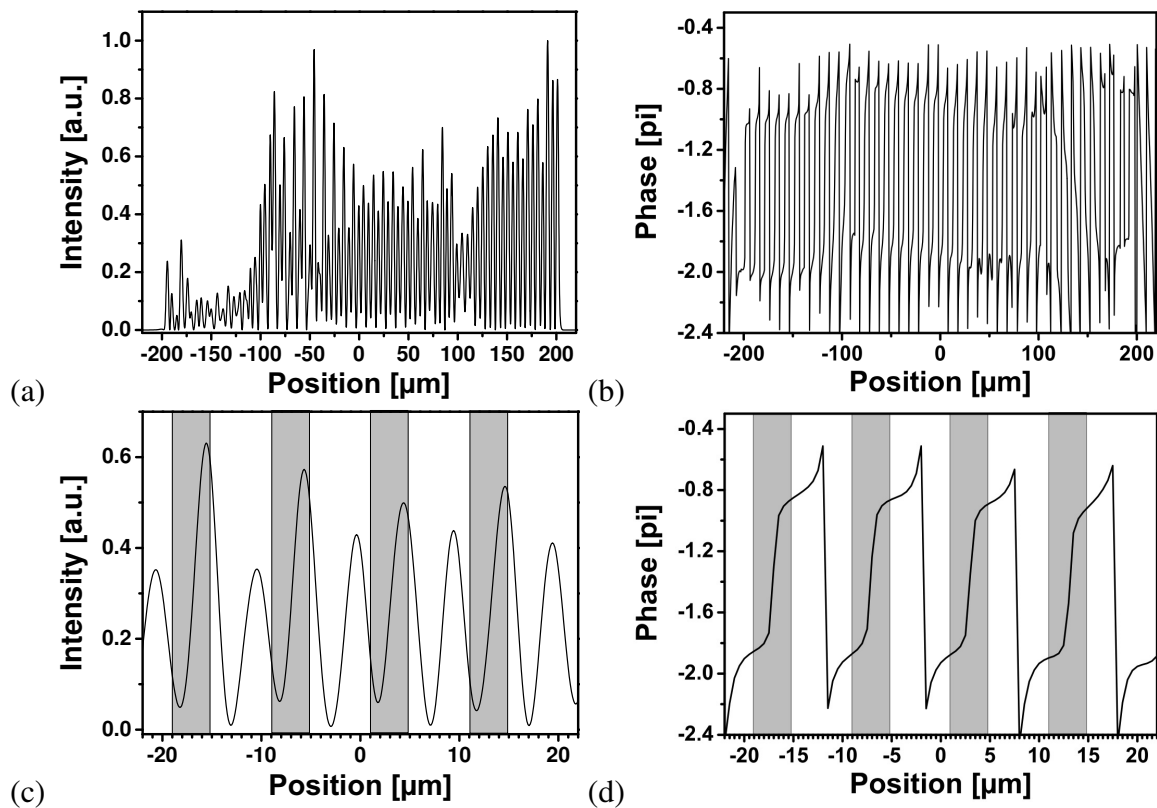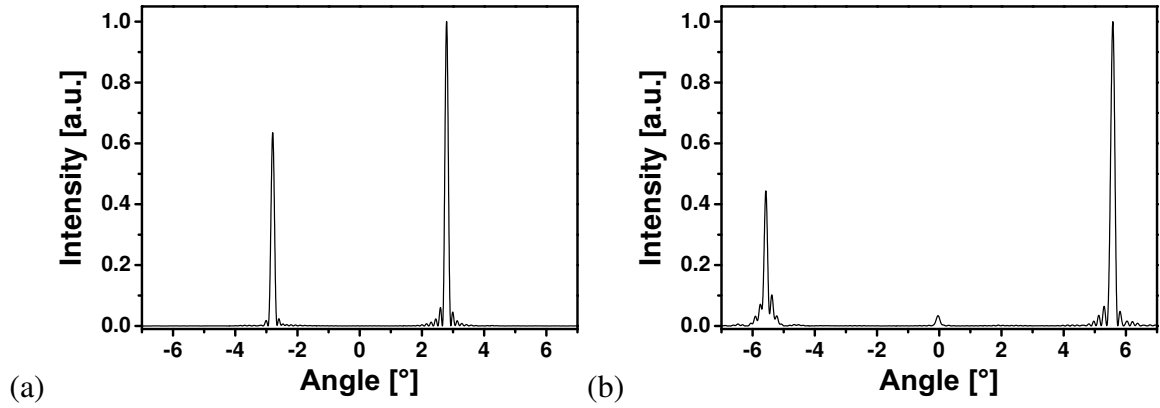
Figure 5.20: Calculated far-field intensity distribution for (a) the lowest order out-of-phase super-
mode at $\alpha_{\text{FB}} = 2.8°$ and (b) the second order in-phase supermode at $\alpha_{\text{FB}} = 5.6°$.

peaks represent the grating position or the incident field, respectively. Both show good
agreement with the measured far-fields (Fig. 5.15 (a) and Fig. 5.17 (a)).

5.3 Summary

In this chapter, the longitudinal mode selection and stabilization of stripe-array amplifiers
was studied. In the first section, an on-axis Littrow ECDL with arbitrary angular feedback
was used. High output powers in combination with wavelength stabilization and narrow
bandwidth emission could be realized. At the maximum output power of 6.8 W, a band-
width below 100 pm was determined and the center wavelength was tunable over a range
of more than 40 nm. However, because of the lack of transversal mode selectivity of the
external cavity, no specific array supermode could be stabilized in lateral direction. Thus,
the beam quality along the slow-axis remained as poor as for the free running stripe-array
diode laser. Therefore, the on-axis ECDL is not suitable for nonlinear application like SHG.
Nevertheless, a demand for such laser systems exists. It can be applied for the pumping of
advanced solid state lasers or alkali vapor lasers as an alternative to volume Bragg grating
stabilized BA lasers and laser bars.

Following the investigations made in chapter 4, an asymmetric off-axis Littrow ECDL
with a high angular selectivity was developed to realize a stabilization of an array super-
mode. By realizing a π phase shift between neighboring emitters, the lowest order out-
of-phase mode corresponding to $\alpha_{\text{FB}} = 2.8°$ at $\lambda = 976$ nm was selected. The near field
pattern showed a homogeneous distribution. The far-field showed an asymmetric double
lobed distribution, whereas each lobe was nearly diffraction limited.

With the stripe-array stabilized in this supermode, emission with high brilliance could
be realized. Near diffraction limited emission with an output power of more than 1 W
could be achieved. The slow-axis beam quality could be improved from about $M_x^2 \approx 60$
to $M_x^2 \approx 1.5$, while in fast-axis a beam quality of $M_y^2 \approx 1.17$ was measured. This
gives a brightness of $B = 62.5$ MW/cm²-str. Furthermore, wavelength stabilization and a
large tuning range of more than 35 nm was obtained. The bandwidth was measured to be
1.73 MHz which is more than five orders of magnitudes better than for the free running
stripe-array diode laser without external cavity. However, some limitations were observed.
Compared to the on-axis ECDL, the threshold was shifted to higher injection currents, the
slope efficiency was lower and thermal rollover started at lower injection currents. This is

mainly caused by heating of the stripe-array amplifier. Furthermore, higher lateral modes arose at higher injection currents. This limited the output power in the central lobe and lead to a degradation of the beam quality. This behavior is attributed to current spread and the presence of leaky waves. Thus, the stripe-array will behave rather similar to a standard BA device because the current spread smears out the stripe pattern. Since the external cavity only supports a certain lateral mode, this can be the reason for the heating of the device.

By operating the stripe-array amplifier at a feedback angle of α_{FB} = 5.6°, the second order in-phase mode ($L = 2N$) could be stabilized. This resulted in a doubling of the number of intensity maxima in the near-field. A similar effect was observed by Epler et al. [77], where an on-axis external grating cavity and an AR-coated 10 element stripe-array was investigated. They could operate the array in the $L = 2N$ supermode by detuning the wavelength of a stripe-array. Although this supermode was found to be stable in the present work, the output power was significantly lower than with the lowest order in-phase-mode. Furthermore, the beam quality was degraded and the off-axis ECDL was stronger limited by thermal effects compared to the other supermode investigated.

To explain the experimental results, the numerical model presented in the third chapter was extended with a feedback model in cooperation with the WIAS-Berlin. The calculated far and near field distributions showed a good agreement with the measurements. If feedback was applied at the native out-of-phase array supermode the field was concentrated beneath the stripes and the field inside the chip was homogeneous. If the feedback angle was increased in the model, field strength inside the chip was also present between the stripes. This behavior can be explained by the presence of leaky waves and a strong antiguiding effect. Thus, the stripe-array behaves similar to a BA device under certain circumstances. The model was useful for the interpretation of several of our experimental observations.

The values reported here represent the highest brightness achieved with a wavelength stabilized BA or stripe-array diode laser or amplifier. Chang-Hasnain et al. used an off-axis external cavity with a stripe mirror and a 10 element stripe-array and could realize 140 mW diffraction limited output power [7]. Later, higher powers of up to 400 mW with M^2 = 1.03 have been demonstrated by Raab et al. with a 20 element stripe-array [65]. However, no wavelength stabilization or bandwidth narrowing was realized in these attempts. Raab et al. used a grating stabilized ECDLs utilizing off-axis feedback and could achieve up to 380 mW with $M^2 < 1.05$ and a bandwidth of 0.02 nm with a 20 element stripe-array [64]. Samsoe et al. could achieve up to 400 mW near diffraction limited emission with $M^2 \approx 3.6$ and $\Delta\lambda < 0.08$ nm [66, 78] with a BA diode laser in a Littman ECDL. Løbel et al. used additional phase conjugating crystals and could realize up to 465 mW with $M^2 \approx 1.5$ and $\Delta\lambda < 0.03$ nm with a 10-element stripe-array [79].

In summary, high brilliance emission from a stripe-array amplifier could be realized by investigating the physical characteristics theoretically and experimentally. As a result an off-axis ECDL was developed. Due to the good lateral beam quality and the narrow bandwidth of emission it is possible to utilize this off-axis ECDL as pump laser for the nonlinear frequency conversion. Furthermore, the off-axis ECDL setup stands out by its simplicity and compactness. It consists of only four optical components (or five considering the optional aperture). The resonator length was 40 mm and a footprint of 60 mm x 50 mm could be realized.

Part II

Nonlinear frequency conversion with diode lasers

Chapter 6

Second harmonic generation

In the first part of this thesis, the selection and stabilization of the longitudinal and transversal modes of BA and stripe array amplifiers was investigated with external cavities. One aim of this work was to realize tunable, wavelength stabilized high brightness emission from these devices.

The second goal pursued in this thesis was the application of diode laser systems to nonlinear frequency conversion. With the stripe-array operated in the off-axis ECDL, more than 1 W of near-diffraction limited output power with a bandwidth below 2 MHz was achieved. This qualifies this newly developed ECDL device for the efficient generation of visible radiation by frequency doubling.

In this chapter, the foundations of SHG will be discussed briefly for the orientation of the reader. This includes phase-matching, nonlinear material properties, limitations and damage mechanisms as well as the requirements to achieve a high nonlinear conversion efficiency.

SHG was first demonstrated in 1961 by Franken et al. [80] and is the most exploited nonlinear process to date. Since the availability of periodically poled nonlinear materials have opened the door for efficient frequency doubling using diode lasers as pump sources, the emphasis is laid on these new materials.

6.1   Nonlinear polarization

The polarization $\mathbf{P}$ inside a dielectric medium is described as the sum of the linear and all nonlinear polarization components of the n-th order with the susceptibilities χ of the n-th order:

$$\mathbf{P}_{\mathrm{res}} = \sum_n \mathbf{P}_n = \varepsilon_0 \sum_n \chi^{(n)} \mathbf{E}^n. \tag{6.1}$$

The following sequence is obtained:

$$\mathbf{P}_{\mathrm{res}} = \varepsilon_0 \chi^{(1)} \mathbf{E} + \varepsilon_0 \chi^{(2)} \mathbf{E}^2 + \varepsilon_0 \chi^{(3)} \mathbf{E}^3 + \varepsilon_0 \chi^{(4)} \mathbf{E}^4 + \cdots . \tag{6.2}$$

As stated before, only second order processes will be discussed here so only the first two terms on the right hand side of this equation are of interest. A monochromatic wave $\mathbf{E}(\omega) = \mathbf{E}_0 e^{-i\omega t} + c.c.$ with a high intensity will induce a polarization wave inside a dielectric nonlinear medium with a second order susceptibility $\chi_{ijk}^{(2)}$. The polarization will read:

$$\mathbf{P}_i = \varepsilon_0 \sum_j \chi_{ij}^{(1)} \mathbf{E}_j(\omega) + \varepsilon_0 \sum_{jk} \chi_{ijk}^{(2)} \mathbf{E}_j(\omega) E_k(\omega), \tag{6.3}$$

whereas the right term is the second order polarization. For the monochromatic wave $\mathbf{E}(\omega)$ the second order polarization will read after a trigonometric transformation:

$$\mathbf{P}_i^{(2)} = 2 \cdot \varepsilon_0 \sum_{jk} \chi_{ijk}^{(2)} \mathbf{E}_{0,j} \mathbf{E}_{0,k} \cos(2\omega t) + 2 \cdot \varepsilon_0 \sum_{jk} \chi_{ijk}^{(2)} \mathbf{E}_{0,j} \mathbf{E}_{0,k}^*. \tag{6.4}$$

Here, the left term is the second harmonic and the right term the optical rectification. This polarization wave is the source for the second harmonic light wave.

Since several simplifications can be made in the case of SHG, the second order nonlinearity is mostly described in the contracted notation by the d_{il} coefficient: $2 \cdot d_{il} = \chi_{ijk}^{(2)}$ (see appendix A.1). Depending on the propagation direction of the participating fields to the corresponding axis of d_{il}, an effective nonlinear coefficient d_{eff} is used in most cases [81].

6.2   Quasi phase-matching

In a second order nonlinear process three waves participate. The law of the conservation of energy demands for the following relationship concerning the frequencies of the three waves:

$$\omega_1 + \omega_2 = \omega_3. \tag{6.5}$$

The phase-mismatch Δk describes the deviation between the wave vectors:

$$\Delta k = k_1 + k_2 - k_3 \tag{6.6}$$

For the special case of SHG with $k_1 = k_2 = k_{\mathrm{FUN}}$ and $k_3 = k_{\mathrm{SHG}}$ this can be simplified to:

$$\Delta k = k_{SHG} - 2k_{FUN} \tag{6.7}$$

and the phase-mismatch Δk becomes zero at:

$$n_{\mathrm{FUN}} = n_{\mathrm{SHG}}. \tag{6.8}$$

Phase-matching can be realized by using birefringent material [82].

If the phase-mismatch Δk between the participating waves in a nonlinear process is not zero, the intensity of the generated light will oscillate with a certain length L_c called the coherence length of the crystal. Up to L_c, the energy of the fundamental wave will flow into the second harmonic wave. At longer distances than L_c, destructive interference will occur and the SHG intensity will decrease to zero at $2L_c$. The coherence length L_c is linked to the phase-mismatch Δk by:

$$L_c = \frac{\pi}{|\Delta k|}. \tag{6.9}$$

For perfect phase-matching with $\Delta k = 0$ the coherence length will become infinite and the energy of the pump wave will completely flow into the second harmonic.

The concept behind quasi phase-matching (QPM) is that the crystal domain is reversed periodically at the coherence length, so that destructive interference between the participating waves will not occur [83]. Rather, the phase of the generated nonlinear polarization wave will be shifted by π at the domain inversion boundary. The conversion process will be initiated again, leading to constructive interference. This is illustrated in Fig. 6.1 for SHG, showing the intensities for all three cases: perfect phase-matching (red line), no phase-matching (black line) and quasi phase-matching (green line).
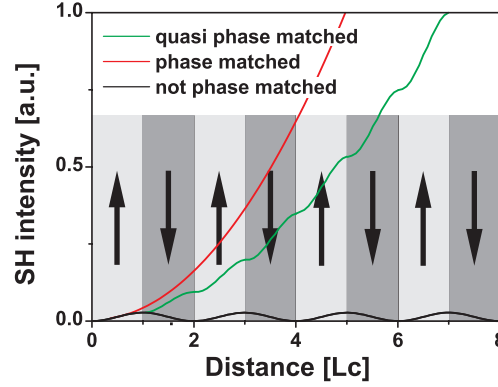
Figure 6.1: SHG intensity as a function of the coherence length L_c for perfect phase-matching (red line), quasi phase-matching (green line) and no phase-matching (black line). The arrows indicate the orientation of the domains of a periodically poled crystal.

The spatial period Λ_{QPM} for QPM is given by:

$$\Lambda_{\mathrm{QPM}} = 2L_c = \frac{2\pi}{\Delta k}. \tag{6.10}$$

It can be derived for the refractive indices of the participating waves by:

$$\frac{1}{\Lambda_{\mathrm{QPM}}} = \frac{n_{\mathrm{SHG}}}{\lambda_{\mathrm{SHG}}} - \frac{2n_{\mathrm{FUN}}}{\lambda_{\mathrm{FUN}}}. \tag{6.11}$$

The efficiency of QPM is lower compared to perfect PM and the resulting d coefficient $d_{\mathrm{il,QPM}}$ is reduced by a factor of $2/\pi$:

$$d_{eff,QPM} = m_{order} \cdot \frac{2}{\pi} d_{eff}, \tag{6.12}$$

where m_{order} is the QPM grating order.

However, this drawback is outweighed by several other advantages of QPM compared to birefringent phase-matching: Birefringent phase-matching is not possible for copolarized waves which limits the accessible nonlinear coefficients d_{il} (see appendix A.1). However, the nonlinear coefficients where copolarized waves participate are usually very high. For example the d_{33} coefficient in lithium niobate is ≈ 28.4 pm/V and can only be accessed with QPM. This is nearly seven times higher than the d_{31} coefficient ≈ 4.3 pm/V, which is used with birefringent phase-matching. Additionally, spatial "walk-off" can be avoided completely at QPM, which makes long interaction lengths feasible. A detailed investigation on SHG with QPM materials is given in [84], a review of several QPM processes and materials can be found in [85].

6.3 Nonlinear materials for QPM

The idea of quasi phase-matching is as old as birefringent phase-matching [82] and was proposed by Armstrong et al. in 1962 [83]. The first QPM material was successfully demonstrated by Bloembergen 1970 by growing alternating layers of GaAs and GaP for SHG of CO_2 lasers [86].

The first attempt for frequency doubling to the visible using ferroelectrics was done by Feng et al. 1980 [87] and later the principle of periodically poling of ferroelectrics was

established [88]. In a ferroelectric crystal there exists a small electric dipole moment below the Curie temperature which is caused by a slight offset in the position of the ions in its unit cell. One possibility to reverse the domain direction is applying an intense electric field of (≈ 20 kV/mm) to the crystal. First order poled ferroelectrics for frequency doubling to the blue spectrum were first demonstrated in 1993 [89]. A schematic drawing of a periodically poled crystal is shown in Fig. 6.2.

6.3.1   Periodically poled ferroelectrics

The three most commonly used ferroelectrics for the manufacturing of QPM crystals are periodically poled lithium niobate (PPLN), periodically poled lithium tantalate (PPLT) and periodically poled potassium titanyl phosphate (PPKTP).

Lithium niobate $LiNbO_3$ (LN) is the most widespread and versatile material among the ferroelectrics used for frequency conversion and QPM applications. It is transparent from 320 nm to about 4.6 μm. Besides the high second order nonlinearity of $d_{33} \approx 28.4$ pm/V [90], it possesses high electro-optical and acousto-optical coefficients.Thus, it is also used for electro-optical switches such as Pockels cells, Q-switches and phase modulators. The damage threshold is in the range of 300 MW/cm^2 [91]

The coercive field of congruent LN is ≈ 22 kV/mm [92], which leads to a limited substrate thickness of about 500 μm. The coercive field reduces at elevated temperatures ($250°C$), by magnesium oxide (MgO) doping [92] and by using stoichiometric LN. With these techniques, poling of up to 5 mm thick substrates have been realized [93].

The achievable intensity of the SHG light is mainly limited by photo-refractive effects, which can be suppressed by MgO doping. Poling periods as short as 1.4 μm for SHG at a wavelength of 340 nm have been demonstrated [94].

Lithium tantalate $LiTaO_3$ (LT) has a nonlinear coefficient of $d_{33} \approx 15.1$ pm/V. The transparency of LT reaches deeper into the UV spectrum with 275 nm [95] and the shortest SHG wavelength achieved with PPLT is 325 nm [96]. The shortest period reported for first order QPM is 1.3 μm resulting in efficient SHG of light at 336 nm [97].

The coercive field of congruent LT is ≈ 21 kV/mm, but is reduced for stoichiometric crystals (≈ 1.7 kV/mm) [98]. This promises the poling of much thicker crystals. So far, 3 mm thick samples have been reported [99]. Furthermore, near stoichiometric lithium tantalate shows low susceptibility to photo-refraction and can be used for high power visible light generation near room temperature [100].

Potassium titanyl phosphate $KTiOPO_4$ (KTP) is also used as material for electro-optical modulators and directional couplers. It is transparent from 360 nm to 2.7 μm [101] and has a nonlinear coefficient of $d_{33} \approx 18.5$ pm/V [102]. Non-poled KTP bulk material was mainly used for intracavity SHG of solid state lasers, because it possesses a higher optical damage threshold than LN and LT of 10 GW/cm^2 [103, 104].

KTP shows nearly no photo-refractive effects even at room temperature. Furthermore, the wavelength acceptance bandwidth is larger and therefore the temperature tuning curve is broader than in LN and LT [105]. Thus, the requirements for the temperature controller are more relaxed compared to the other two materials.

However, KTP tends to a kind photo darkening or photochromic damage that is called gray tracking [106] which is usually a reversible process, but also permanent damage might
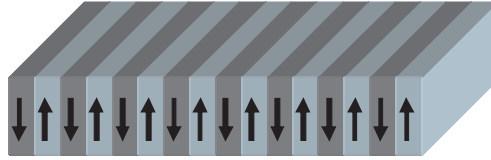
Figure 6.2: Sketch of a periodically poled crystal. Arrows indicate the orientation of the ferroelectric domains.

occur at high peak powers. This effect occurs mainly in pulsed operation at very high peak powers and depends on the pulse length and the repetition rate. Gray tracking is not likely in cw operation, even not in waveguide devices.

6.3.2 Waveguides and waveguide fabrication

QPM materials are available as bulk crystals or with channel and planar waveguide structures. In a bulk crystal no optical confinement or index step is realized. In a planar waveguide the optical confinement is realized in only one dimension, while in a channel waveguide this is realized in two dimensions, as shown in Fig. 6.3. Beside their relevance in integrated optics (e.g. for telecommunication), those waveguides are of importance for frequency conversion. The early work for obtaining blue light with QPM structures was actually based on planar waveguides because of the limitation of the domain inversed layer thickness [88]. Nowadays high quality crystals with lengths > 30 mm are commercially available with channel waveguides.

Proton exchanged waveguides Waveguides in LN and LT crystals can be fabricated by proton exchange [107, 108]. During proton exchange the substrate is immersed into benzoic or pyrophosphoric acid. The lithium ions inside the crystal are exchanged with protons in the melt, resulting in a proton-enriched surface layer. The index profile with $\Delta n \approx 0.1$ is step like and a waveguide for one polarization with strong optical confinement is formed. In principle this will lead to a planar waveguide over the whole width of the sample. To obtain a channel waveguide a further mask (e.g. made out of silica) has to be applied, so that the proton exchanged region has the appropriate width of a few μm.

However, the proton exchanged layer will show a dramatically decrease of the second order nonlinearity. This can be overcome by annealing, whereby the protons will diffuse deeper into the substrate. Annealed proton exchange results in the recovery of the nonlinear coefficient. However, with this technique an asymmetric index profile is formed, which can be avoided by rediffusion of lithium ions into the surface layer of the substrate. This is possible by immersing the sample into a melt with high lithium concentration, so

Figure 6.3: Waveguides in nonlinear crystals.

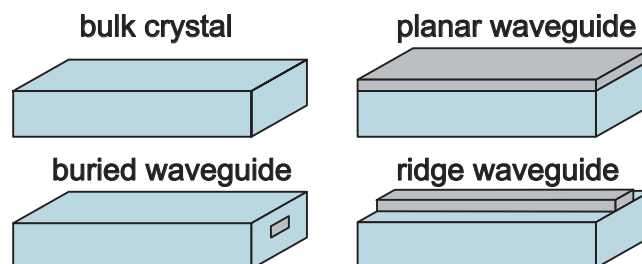that the protons will diffuse out of the surface layer and will be replaced by lithium ions. This method is called reverse proton exchange and will result in a buried waveguide with symmetric index profiles and low losses [109].

Ion exchanged waveguides   Ion exchange is used to obtain optical waveguides in KTP. Here rubidium ions are diffused through a mask into the substrate for several tens of minutes at temperatures around 300 °C [110]. The optical damage resistance of ion-exchanged KTP waveguides was reported to be very high compared to LN waveguides [111].

Ridge waveguides   Ridge waveguides are manufactured by poling a thin substrate and adhering it to a bulk substrate. In a second step the substrate is polished to a few μm thickness for optical guidance in one dimension resulting in a planar waveguide. The ridge itself can be manufactured by an etching process [112] or by micro-machining, e.g. with a diamond blade saw [113]. Poling of the ridge waveguide after adhering has been reported as well [114].

6.3.3   Limitations and damage mechanisms

Photo-refraction   The most limiting issue for frequency conversion in ferroelectrics is photo-refraction [115], which causes a QPM wavelength shift, degradation of the SHG output power and can lead to severe beam distortions. It was shown experimentally that this effect can be suppressed by operating the QPM materials at elevated temperatures [116] or by doping the material with MgO or ZnO [117, 118]. In both cases, the reduction is a consequence of the screening of the induced space charge field due to the higher conductivity.

An explanation for the photo refractive effect is that impurities in the crystal such as Fe^{3+} ions can absorb light and a free carrier will be photoexcited into the conduction band. At the same time an electron hole is generated and the conductivity will increase. The free electron in the conduction band can diffuse throughout the crystal and might recombine with one of the holes. A photovoltaic current will flow because of the noncentrosymmetric structure of the crystal. This space charge field will lead to a change of the refractive index due to the electro-optical effect.

Induced absorption   Furthermore, induced absorption of infrared light was observed in ferroelectrics when they were illuminated by short wavelength radiation. The so called green induced infrared absorption [119] and blue light induced infrared absorption [120] are highly unwanted effects, especially for frequency doubling to the visible. Both effects result in an additional heating of the material and cause a disturbance of the QPM structure. It can even cause a thermal lens inside the crystal.

One reason for the induced absorption is that color centers due to polarons, which are possibly caused by two-photon absorption, will arise. In most cases these effects are reversible, but permanent photochromic damage can occur when the material is illuminated over a long time. Polarons are also responsible for the gray tracking in KTP. Beside the suppression of photo-refractive effects and induced absorption by doping it was observed that both effects are far less pronounced in stoichiometric structures.

6.4 Second harmonic conversion efficiency

6.4.1 Bulk crystals

Focusing of Gaussian beams into a nonlinear bulk crystal: The high intensities that drive the nonlinear processes originate typically from laser beams. Thus, in most cases the field distribution is Gaussian shaped. Although the intensity of the generated wave depends strongly on the intensity of the applied field, it is also important to have a long interaction length for efficient conversion. In practice, a trade off between strong focusing to get a high peak intensity and loose focusing to maintain a high average intensity over a long interaction length has to be made (Fig. 6.4).
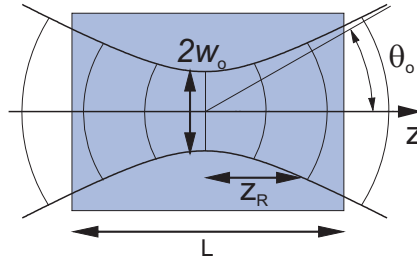
Figure 6.4: Focusing of a Gaussian beam in a nonlinear crystal.

Boyd and Kleinman have analytically investigated this problem for a Gaussian beam inside a bulk nonlinear crystal [121]. For low conversion efficiencies, the output power of the generated wave will depend quadratically on the power of the fundamental light and scale linearly with the crystal length:

$$P_{\mathrm{SHG}} = \frac{16\pi^2 d_{eff}^2 L}{n_{\mathrm{FUN}} n_{\mathrm{SHG}} c_0 \varepsilon_0 \lambda_{\mathrm{FUN}}^3} P_{\mathrm{FUN}}^2 h\left(B_{\mathrm{wo}}, \xi, \sigma\right). \tag{6.13}$$

Where $h\left(B_{\mathrm{wo}}, \xi, \sigma\right)$ is the focusing function that depends on the focusing parameter or the confocal parameter:

$$\xi = \frac{L}{b},$$

the spatial "walk-off" factor:

$$B_{\mathrm{wo}} = \varphi\sqrt{Lk_{\mathrm{FUN}}}/2,$$

and the phase-matching:

$$\sigma = b\Delta k/2.$$

The factor b is twice the Rayleigh length:

$$b = 2 \cdot z_{\mathrm{R}} = \frac{2 \cdot \pi \cdot n \cdot w_0^2}{\lambda},$$

L is the crystal length and the φ is the spatial "walk-off" angle .

For the case of QPM no spatial "walk off" occurs. In this case, the h-function will has its maximum of $h = 1.07$ at $\xi = 2.84$ and the optimum beam waist radius becomes:

$$w_0 = \sqrt{\frac{\lambda \cdot L}{2 \cdot 2.84 \cdot \pi \cdot n}}. \tag{6.14}$$

Confocal focusing where $\xi = 1$ and therefore b = L is also very commonly used. In this case, h will become 0.78 with the cost of $\approx 27\%$ conversion efficiency. However, due to the more loose focusing, the peak intensity in the material is lower which can shift the onset of photo-refractive effects or induced absorption to higher pump powers. Again a trade off has to be made: If the system is limited by photo-refractive or induced absorption confocal focusing should be considered. Otherwise, tighter focusing following the Boyd Kleinman analysis should be chosen.

The equation 6.13 can be simplified by introducing the conversion efficiency η_{bulk} with units $\%/W \cdot$cm:

$$P_{\text{SHG}} = \eta_{\text{bulk}} \cdot P_{\text{FUN}}^2 \cdot L. \tag{6.15}$$

The low power approximation is only useful up to opto-optical conversion efficiencies of $\eta_{opto} \approx 15\%$, otherwise pump depletion has to be taken into account giving:

$$P_{\text{SHG}} = P_{\text{FUN}} \cdot \tanh^2 \left(\sqrt{\eta_{\text{bulk}} \cdot L \cdot P_{\text{FUN}}} \right). \tag{6.16}$$

The use of non-diffraction limited beams   However, if non-diffraction limited beams with beam propagation factors of $M^2 > 1$ are used, the SHG conversion efficiency will be lower. As a rule of thumb the impact of the pump laser beam quality on the achievable SHG output power can be estimated by:

$$P_{\text{SHG}} \approx \eta_{\text{bulk}} \cdot \frac{P_{\text{FUN}}^2}{M_x^2 \cdot M_y^2}. \tag{6.17}$$

The influence of the beam propagation factor on the SHG conversion efficiency and the Boyd-Kleinman focusing conditions for non-diffraction limited, astigmatic and elliptic beams has been studied in detail in [122, 123].

6.4.2   Waveguides

In a nonlinear waveguide with strong optical confinement, the intensity of the pump wave will be high over a long distance. Thus, very high conversion efficiencies and long inter-action lengths are possible. Moreover, no compromise between interaction length and peak intensity in the focus has to be made. On the other hand, a waveguide demands for sophisticated coupling optics and coupling losses can become very high. Due to the high power densities inside the waveguide, photo-refractive effects and induced absorption have to be taken into account as possible limitations.

In a waveguide the generated power depends quadratically on the length L of the crystal and the fundamental power and the case of pump depletion has to be considered. Equation 6.16 then becomes:

$$P_{\text{SHG}} = P_{\text{FUN}} \cdot \tanh^2 \left(\sqrt{\eta_{\text{wg}} \cdot P_{\text{FUN}} \cdot L^2} \right), \tag{6.18}$$

with the waveguide conversion efficiency η_{wg} (with units $\%/W \cdot$cm^2).

6.4.3   Wavelength and temperature acceptance bandwidth

Since QPM is most commonly realized as noncritical phase-matching, the crystal temperature has to be controlled with a precision of ≈ 0.1K. The so called temperature acceptance

bandwidth ΔT (FWHM) is [84]:

$$\Delta T_{\text{FWHM}} = \frac{0.4429 \cdot \lambda_{\text{pump}}}{L} \left| \left(\frac{\partial n_{\text{FUN}}}{\partial T} + \frac{\partial n_{\text{SHG}}}{\partial T} \right) - \alpha_L \left(n_{\text{FUN}} - n_{\text{SHG}} \right) \right|^{-1}, \quad (6.19)$$

with the pump laser wavelength λ_{pump} and the linear expansion coefficient α_L. The refractive indices can be calculated using the Sellmeier equations.

Furthermore, the conversion efficiency depends on the wavelength acceptance bandwidth $\Delta\lambda_{\text{Crystal}}$ of the crystal, which is inversely proportional to its length L. With the pump laser wavelength λ_{pump} the wavelength acceptance bandwidth reads [84]:

$$\Delta\lambda_{\text{Crystal}} = \frac{0.442 \cdot \lambda_{\text{pump}}}{L} \left| \frac{n_{\text{SHG}} - n_{\text{FUN}}}{\lambda_{\text{pump}}} + \frac{\partial n_{\text{FUN}}}{\partial\lambda_{\text{pump}}} + \frac{\partial n_{\text{SHG}}}{2\partial\lambda_{\text{pump}}} \right|^{-1}. \quad (6.20)$$

If the pump laser bandwidth exceeds the wavelength acceptance bandwidth or the crystal temperature is not precisely controlled, the conversion efficiency will be lowered. If the pump wavelength is slightly shifted from the ideal QPM wavelength λ_{QPM} the SHG output power will be lower following a sinc function [105]:

$$P_{\text{SHG}} = P_{\text{SHG,ideal}} \cdot \text{sinc} \left[0.08858\pi \left(\frac{\lambda_{\text{pump}} - \lambda_{\text{QPM}}}{\Delta\lambda_{\text{Crystal}}} \right) \right]. \quad (6.21)$$

This is only valid if the laser has a negligible bandwidth. However, in practice a laser has a certain bandwidth that can be close or even exceed the acceptance bandwidth of the crystal. The deviation from the ideal SHG output power if light with a broader bandwidth is used was investigated by Kontur et al. [105]. The resulting SHG output power as a function of the ratio between the laser bandwidth $\Delta\lambda_{Laser}$ and the acceptance bandwidth of the crystal $\Delta\lambda_{Crystal}$ is depicted in Fig. 6.5.
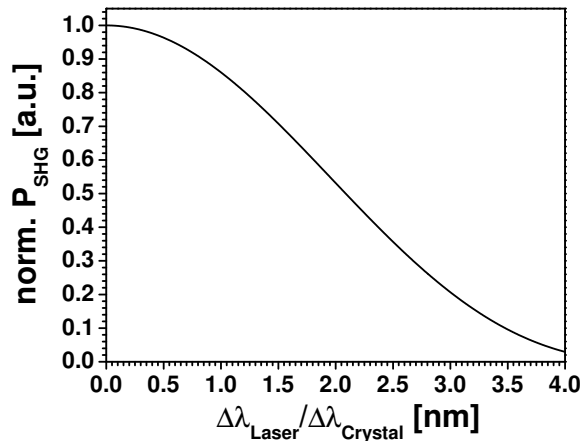

Figure 6.5: SHG output power as a function of the ratio between the bandwidth of the laser and the wavelength acceptance bandwidth of the nonlinear crystal following [105].

Chapter 7

Efficient frequency doubling of high brilliance diode laser emission

As stated before not all emission wavelengths, especially in the visible can be realized directly with diode lasers. A huge gap in the visible spectrum between 480 nm and 630 nm exists where no efficient laser light from diode lasers is available.

Frequency doubling is a common way to generate laser radiation where lasers are not readily available. To achieve a high conversion efficiency, high power densities are necessary for this nonlinear process. Furthermore, the bandwidth of the pump laser light has to be below the acceptance bandwidth of the nonlinear crystal, as presented in the previous chapter. Because of the high requirements on the pump laser emission, mainly diode pumped solid state lasers [124], optically pumped semiconductor disk lasers [125] and fiber lasers [126] have been used to pump SHG. The brightness and the spectral purity of cw diode laser emission was not sufficient. However, because of the outstanding electro-optical efficiency of diode laser emission the direct frequency doubling of edge emitting diode lasers was attempted. The first frequency doubling using a diode laser was performed by Edmonds et al. [127] with a gain switched narrow stripe laser diode and an α-iodic acid crystal in a resonator enhanced SHG setup. With 1 W fundamental power, enhanced to 4.5 W inside the SHG cavity, 15 μW blue light at 452 nm were generates. The opto-optical conversion efficiency was 10^{-5}.

With the emerging of highly efficient periodically poled nonlinear materials that make use of QPM, SHG has become possible with cw emission at moderate pump powers. Since those periodically poled materials are also available as waveguides, it is also possible to achieve efficient high conversion efficiencies with relatively low pump powers in a single pass setup. The single pass configuration is less susceptible to external influences than resonant SHG. Furthermore, it has certain advantages like easy modulation capability of the generated light. However, pump laser emission with a high brilliance and highly efficient nonlinear materials are still required. Since the off-axis ECDL developed in the first part of the thesis yields 1 W emission with a very good spatial mode quality and narrow bandwidth, this device is qualified as pump source for single pass SHG.

In the first section of this chapter, the crystals used in this work are characterized. PPLN and PPKTP were chosen as nonlinear material. In the second section, the experimental results with the off-axis ECDL will be presented. To evaluate the performance of the off-axis ECDL, SHG was performed with a tapered amplifier (TA) ECDL and a DFB ridge waveguide diode laser. The results will be discussed in sections 7.3 and 7.4, respectively.

7.1 Characterization of the nonlinear crystals

For the frequency conversion experiments performed in this thesis four different nonlinear crystals have been utilized. A picture of the four crystals is shown in Fig. 7.1. From left to right: A 40 mm and a 10 mm long bulk PPLN crystal, a 10 mm PPLN waveguide crystal and a 12 mm long PPKTP waveguide crystal.
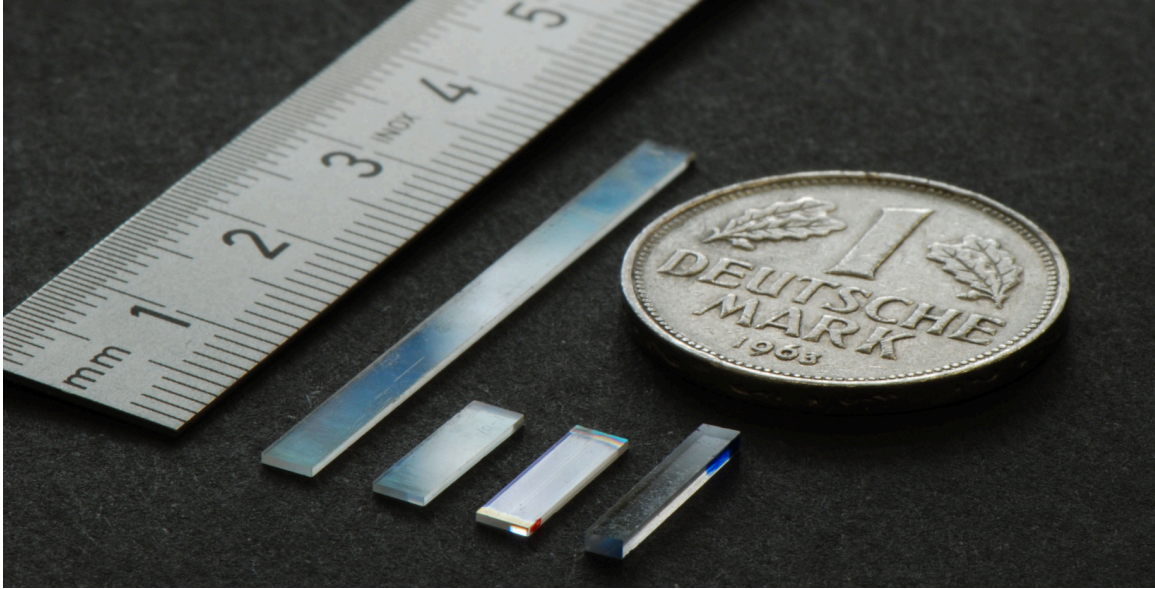
Figure 7.1: Picture of the four nonlinear periodically poled crystals that have been investigated in this work. From left to right: 40 mm bulk PPLN, 10 mm bulk PPLN, 10 mm waveguide PPLN and 12 mm waveguide PPKTP.

All four crystals have been designed for type-0 QPM SHG at a wavelength of 488 nm. Thus, in all cases copolarized waves along the z-axis of the crystals were involved to exploit the high d_{33} coefficient of the materials. The wavelength and temperature acceptance bandwidths of the different crystals presented in the following subsections have been measured using a DFB ridge waveguide diode laser. This DFB diode laser showed a linear temperature tuning behavior with a coefficient of 82 pm/K. The temperature of the diode laser could be controlled with a precision of < 10 mK giving a theoretical resolution of better than 0.82 pm. A detailed characterization of this laser can be found in section 7.4. The calculated and measured values are listed in table 7.1 at the end of this section.

PPLN bulk crystals

The two bulk PPLN crystals were manufactured by *HCPhotonics*, Tawain, from the same wafer. Congruently grown z-cut LN with 5% MgO doping was used. The poling period was 5.26 μm to achieve QPM for SHG at a temperature of $\vartheta \approx 40\text{-}50°$ C for the design wavelength of 488 nm. Two samples with sizes of 10 x 3 x 0.5 mm^3 and 40 x 3 x 0.5 mm^3 were fabricated. To avoid back reflection and Fresnel losses, both facets were flat polished and a double AR coating was applied for fundamental and pump wavelength, respectively. The reflectivities were determined to be R $< 0.25\%$ at 976 nm and R $< 0.50\%$ at 488 nm for vertical incident light.

The SHG output power using the 10 mm long PPLN bulk crystal is depicted in Fig. 7.2 (a) as a function of the crystal temperature. The pump wavelength was 976.6 nm.

Figure 7.2: Temperature (a) and wavelength (b) acceptance bandwidth of the 10 mm long PPLN bulk crystal. The solid line indicates the theoretically expected sinc^2 function.

The temperature acceptance bandwidth at FWHM was determined to be $\Delta T = 2.05$ K. To achieve 90% of the peak conversion efficiency the crystal temperature has to be stabilized with a precision of 0.8 K. In Fig. 7.2 (b) the SHG output power using the 10 mm long PPLN bulk crystal as a function of the pump wavelength is depicted for a constant crystal temperature of $\vartheta = 51.0°$C. The wavelength acceptance bandwidth at the FWHM was $\Delta\lambda = 162$ pm. The solid line indicates the theoretical sinc^2 function.

The corresponding measurements using the 40 mm long PPLN bulk crystal are depicted in Fig. 7.3 (a) and (b), respectively. The wavelength acceptance bandwidth at the FWHM was $\Delta\lambda = 39$ pm for a pump wavelength of 976.2 nm. The temperature acceptance bandwidth at FWHM was $\Delta T = 0.51$ K. The crystal temperature was $\vartheta = 50.5°$C. Both values are a factor four smaller than with the four times shorter crystal, which matches well to the predicted inversely proportional scaling with the crystal length.

The data supplied by the manufacturer were $\Delta T = 2.10$ K for the 10 mm long and $\Delta T = 0.62$ K for the 40 mm long PPLN crystal. From the equations 6.19 and 6.20 theoretical values of $\Delta\lambda = 192$ pm·cm and $\Delta T = 2.01$ K·cm were calculated for 5% MgO doped congruent LN at an operating temperature of $60°$ C. While the calculated data for the temperature acceptance matched well with the measured data, the measured wavelength accpetance bandwidth was lower than the theoretical values following the Sellmeier coefficients given in [128].
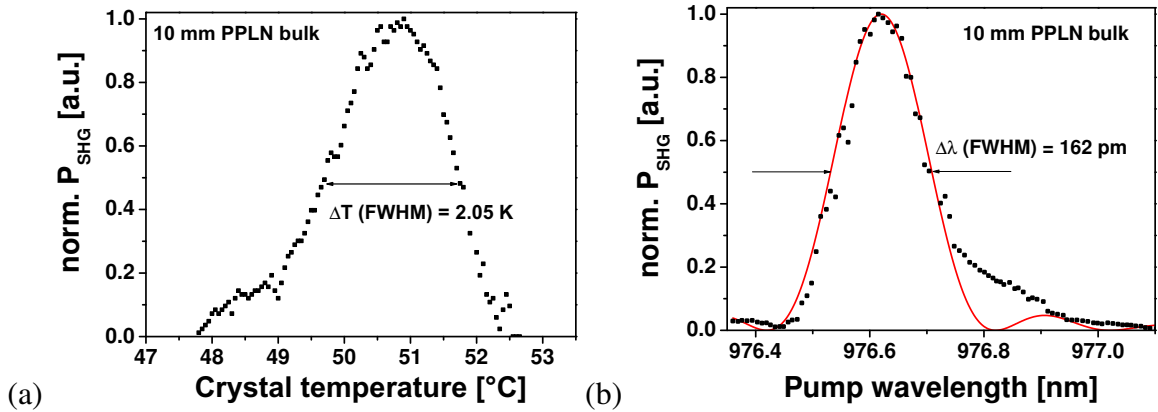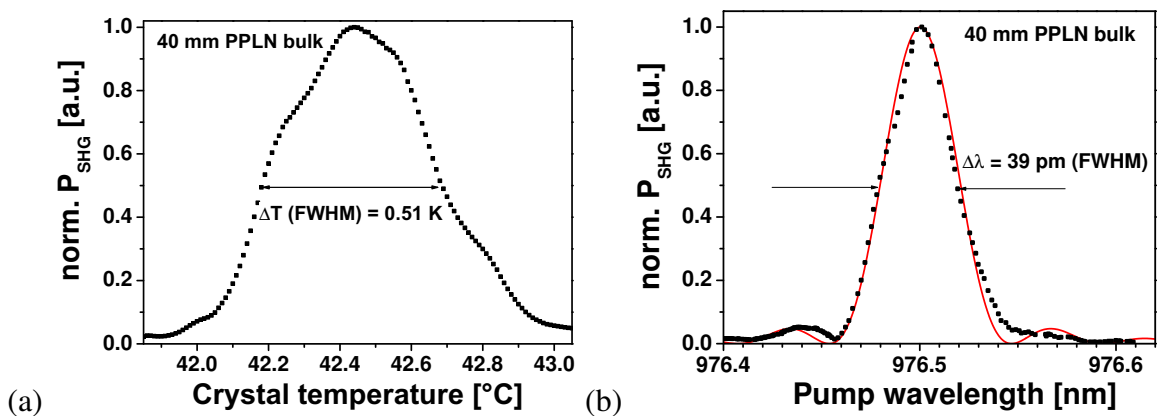

Figure 7.3: Temperature (a) and wavelength (b) acceptance bandwidth of the 40 mm long PPLN bulk crystal. The solid line indicates the theoretically expected sinc^2 function.

PPLN waveguide crystal

The PPLN waveguide crystal had a length of 10 mm and was also manufactured by *HCPhotonics* using 5% MgO doped z-cut congruent LN. The poling period was chosen to be 5.0 μm to realize QPM for SHG at 488 nm at higher temperatures of $\vartheta > 100°$ to avoid photo refraction. Buried waveguide channels with a width of 5 μm and a height of 3 μm have been applied to the crystal by a reverse proton exchanged process as described in section 6.3.2. The crystal had the same AR coating as the bulk PPLN crystals.

The SHG output power using this crystal is depicted in Fig. 7.4 (a) as a function of the crystal temperature. The pump wavelength was 974.8 nm. The temperature acceptance bandwidth at FWHM was determined to be $\Delta T = 1.55$ K. To achieve 90% of the peak conversion efficiency the crystal temperature has to be stabilized with a precision better than 0.4 K. In Fig. 7.4 (b) the SHG output power using the 10 mm long PPLN waveguide crystal as a function of the pump wavelength is depicted for a constant crystal temperature of $\vartheta = 133.5°$ C. The wavelength acceptance bandwidth at the FWHM was 134 pm. These values are slightly lower than the data measured using the bulk crystal of the same length.

Figure 7.4: Temperature (a) and wavelength (b) acceptance bandwidth of the 10 mm long PPLN waveguide crystal. The solid line indicates the theoretically expected sinc^2 function.

PPKTP waveguide crystal

The PPKTP waveguide crystal used in this work was provided by *ADVR-Inc*, Montana, USA. It was fabricated using photo-lithography on a flux grown, z-cut KTP wafer. A direct contact mask designed for 4 μm wide channel waveguides was used to pattern a layer of aluminum onto the +z surface of the wafer. The wafer was diced into 2.25 mm x 12 mm chips and the optical surfaces were angle polished. The chip was placed in a molten bath of rubidium salt at a temperature of 400° C for 120 minutes, where the bare areas of the patterned surface underwent ion exchange. In this process, rubidium ions were diffused into the KTP and the potassium ions were replaced to a depth of around 4-9 μm. During ion exchange, a surface index step of approximately $\Delta n = 0.02$ relative to the surrounding KTP was formed. The periodic domain grating with 7 μm period was designed for SHG near room temperature ($\vartheta \approx 28°$) and applied after the manufacturing of the waveguides.

The PPKTP waveguide crystal had no AR coating applied to its facets. To avoid back reflections back into the pump laser it had wedged facets with an angle of 5°. With a given refractive index of $n_{\mathrm{KTPP}} = 1.84$ the Fresnel losses can be calculated to be 8.7% at each boundary. Thus, the maximum transmission could not exceed 82%. Figure 7.5 shows
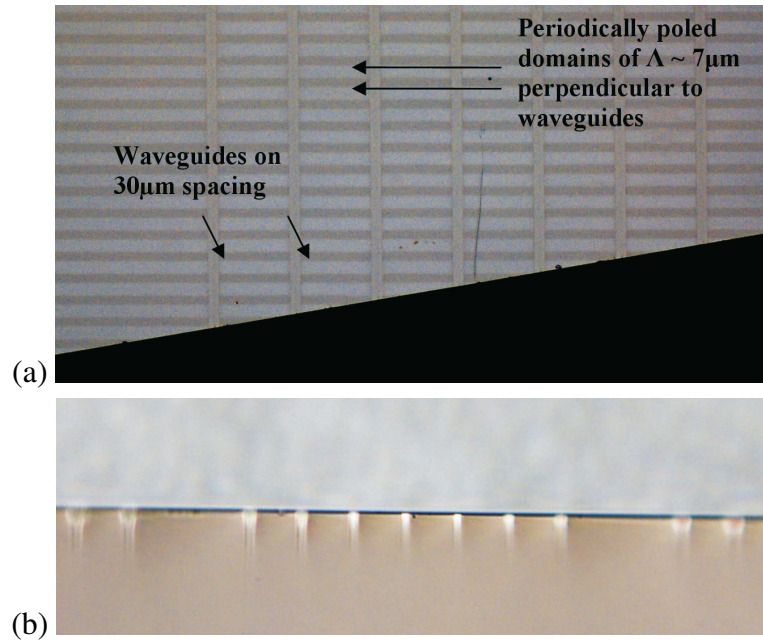
Figure 7.5: (a) Top view of the PPKTP waveguide crystal. (b) View of the front facet of the PPKTP waveguide crystal.

magnified images of a typical PPKTP chip with embedded waveguides. The top picture (a) shows a top view of the PPKTP chip at one of the angled input facets. The 4 μm wide waveguide channels run along the length of the crystal (vertical in the picture) and the periodically poled domains run perpendicular to the waveguides (horizontal). The bottom picture (b) shows the end face of the crystal. Each waveguide was approximately 4 μm wide by 8 μm high.

The measurements to determine the temperature acceptance bandwidth and the wavelength acceptance bandwidth of the 12 mm long PPKTP waveguide crystal are depicted in Fig 7.6 (a) and (b), respectively. The temperature acceptance was $\Delta T = 5.2$ K, which gives a value of $\Delta T = 6.24$ K·cm referenced to the crystal length. The pump wavelength was 976.0 nm. This is very close to the theoretical value of $\Delta T = 6.47$ K·cm calculated from equation 6.19. The wavelength acceptance bandwidth $\Delta\lambda_{\mathrm{PPKTP}}$ was measured to be 280 pm, resulting in $\Delta\lambda = 336$ pm·cm referenced to the crystal length. The crystal temper-
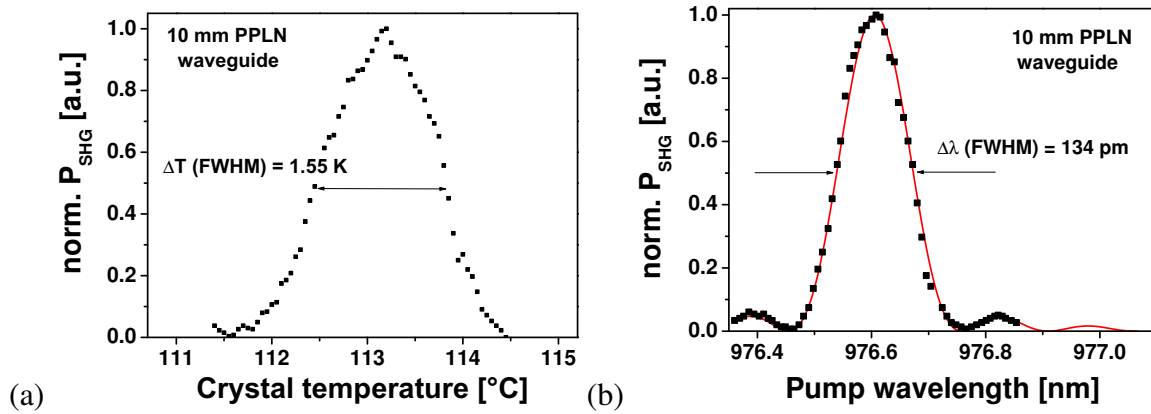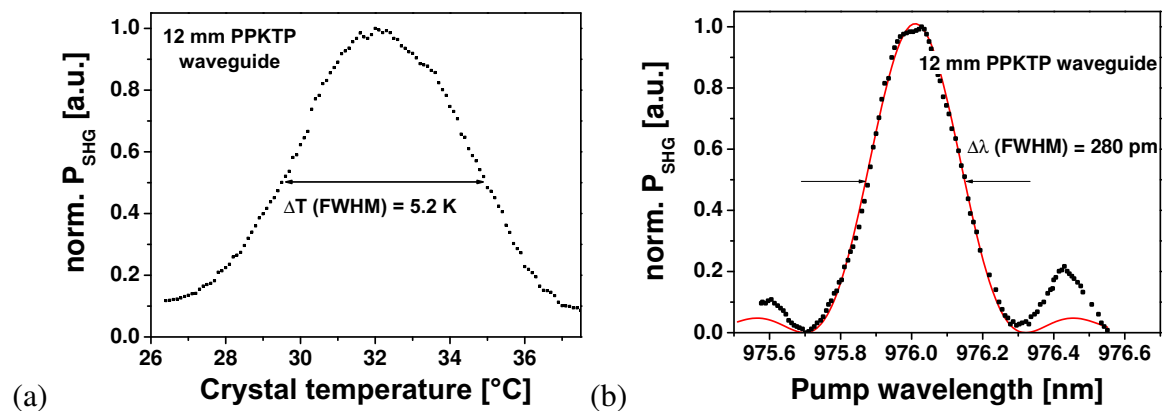

Figure 7.6: Temperature (a) and wavelength (b) acceptance bandwidth of the 12 mm long PPKTP waveguide crystal. The solid line indicates the theoretically expected sinc^2 function.

ature was held constant at 32.0°C. The theoretical value calculated from equation 6.20 was lower with $\Delta\lambda = 294$ pm·cm. The values given in the references were obtained using bulk KTP, while the ion exchanged KTP has a slightly changed refractive index.

Overview

The measured and calculated values for the wavelength acceptance bandwidth and the temperature acceptance bandwidth of the three different crystal materials are shown in table 7.1.

	$\Delta\lambda$ [pm · cm]		ΔT [K · cm]	
	measured	calculated	measured	calculated
PPLN, bulk	162	192	2.05	2.01
PPLN, waveguide	134	191	1.55	1.69
PPKTP	336	294	6.24	6.47

Table 7.1: Measured and calculated values for the temperature acceptance bandwidth and the wavelength acceptance bandwidth for the three different materials.

7.2 Frequency doubling using the off-axis ECDL

In this section, the off-axis ECDL described in section 5.2 is used to generate blue radiation at a wavelength of 488 nm. Single pass SHG has been performed using all four crystals characterized in the previous section.

7.2.1 SHG with bulk crystals

Experimental setup: The experimental setup for SHG using the off-axis ECDL and the bulk crystals is depicted in Fig. 7.7. The off-axis ECDL was operated in the lowest order out-of-phase mode. A detailed description of the ECDL setup and the supermode stabilization was given in section 5.2. The PPLN bulk crystal was placed with the z-orientation
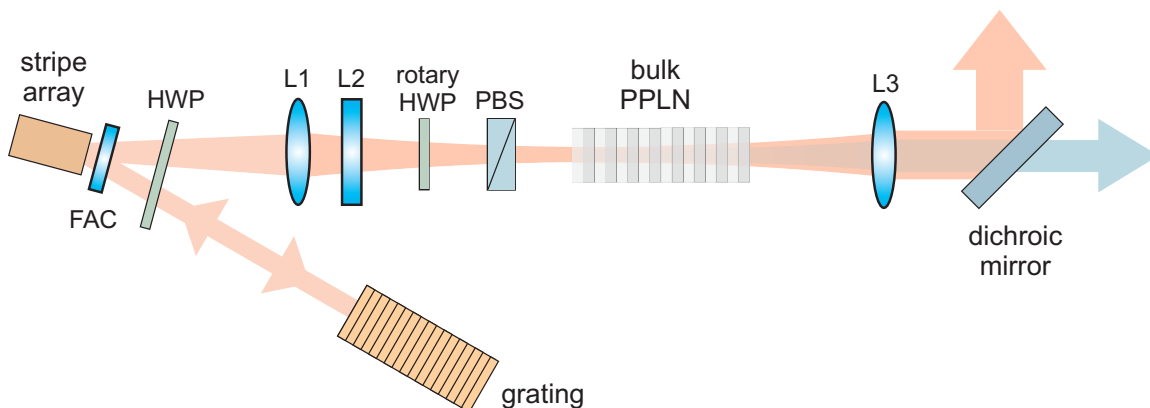
Figure 7.7: Schematic drawing of the frequency doubled off-axis ECDL using PPLN bulk crystal. FAC (fast-axis collimator), HWP (half wave plate), L1 cyl. lens (slow-axis), L2 cyl. lens (fast-axis), L3 collimation lens, PBS (polarization beam splitter).

in direction of the fast-axis. Thus, it was necessary to rotate the electric field of the (TE polarized) emission of the amplifier by 90°. This was realized by using the half wave plate of the ECDL in feedback and outcoupling branch. The emission of the off-axis ECDL showed a residual ellipticity and astigmatism. A beam shaping lens system consisting of two crossed cylindrical lenses L1 in the slow-axis and L2 in the fast-axis was been used to correct ellipticity and astigmatism. With these two lenses, a symmetric focus was formed inside the bulk PPLN crystal. A third lens (L3) was used to collimate the emission behind the crystal. The infrared pump light and the generated blue light were separated with a dichroic mirror. This mirror was highly reflecting (HR) for the infrared light ($\lambda = 976$ nm) and highly transmissive (HT) for the blue light ($\lambda = 488$ nm).

The properties of the two bulk PPLN crystals have been described in section 7.1. Both crystals were manufactured from the same wafer and had to be operated at a temperature around 40-50°C to achieve phase-matching at the wavelength of 488 nm. A 10 mm and a 40 mm long crystal have been used, respectively. The crystals were temperature stabilized by using a thermo-electric cooler that could be controlled with a precision of 0.1 K.

An attenuator consisting of a rotary half wave plate and a polarization beam splitter was used to adjust the amount of light incident at the nonlinear crystal. This has the advantage, that the stripe-array can be operated at a fixed injection current. This attenuator is not mandatory, but thermal drift or a change of the ellipticity and astigmatism (which can shift if the injection current is varied) can be avoided. However, about 10% of the power is lost at the attenuator.

Output power of the blue light: To achieve the highest possible SHG conversion efficiency, an injection current of 2.9 A was chosen as operating point. At this injection current the highest brightness of $B = 62.5$ MW/cm^2·str was achieved (see Fig.5.10 on page 49). At a wavelength of 976 nm the off-axis ECDL yielded emission with a maximum optical output power of 850 mW incident at the crystal. This was slightly lower compared to the value presented in section 5.2. This lower power was attributed to the loss at the polarization beam splitter and the fact that the stripe-array amplifier was not operated at the gain maximum at 972 nm.

An optimum beam waist radius of $w_0 = 31.8\mu$m was calculated for the 40 mm long crystal following the Boyd-Kleinman analysis. With a lens combination of $f_{L1} = 100$ mm and

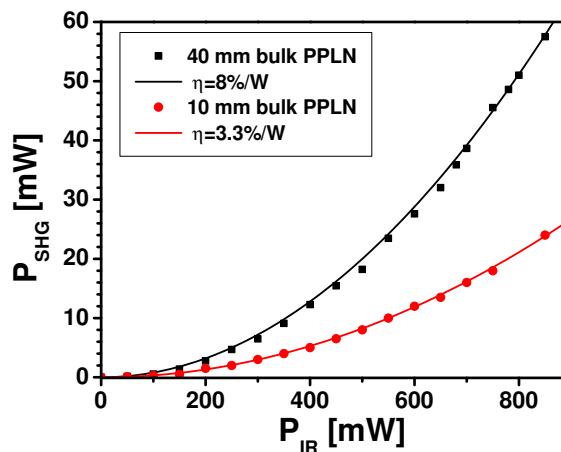**Figure 7.8:** Power of the generated blue light (P_{SHG}) as a function of the infrared pump power (P_{IR}) using the off-axis ECDL as pump source with the two different bulk PPLN crystals.

f_{L2} = 60 mm a beam waist radius of $w_{0,slow}$ = 32.4μm and $w_{0,fast}$ = 31.5μm was measured with a residual astigmatism below 3%. For the 10 mm long crystal the optimum beam waist radius was w_0 = 15.9μm and a lens combination of f_{L1} = 60 mm and f_{L2} = 30 mm was used. In this case, the beam waist radii of $w_{0,slow}$ = 17.3μm and $w_{0,fast}$ = 16.2μm were determined.

Figure 7.8 shows the power of the generated blue light as a function of the power of the incident infrared light for the two different bulk crystals. A maximum SHG output power of 57.5 mW was obtained with 850 mW of incident infrared light by using the 40 mm long crystal. This equals to an opto-optical conversion efficiency of η_{opto} = 6.7%. The measured SHG output power showed a quadratic function to the power of the fundamental wave as theoretically expected (equation 6.15 for undepleted SHG). The quadratic fit through the measured data in Fig. 7.8 resulted in a normalized conversion efficiency of η_{bulk} = 8%/W (or 2%/W·cm, respectively) for the 40 mm long PPLN crystal.

By using the 10 mm long crystal, a maximum SHG output power of P_{SHG} = 22 mW could be generated with 850 mW pump power. The normalized conversion efficiency was calculated to be η_{bulk} = 3.3%/W·cm, which was higher than that of the longer crystal. The bandwidth of the pump laser light was determined to be well below the wavelength acceptance bandwidth of both PPLN crystals and can be excluded as a possible reason for the lower conversion efficiency. Rather, the QPM period might not be perfect since a uniform domain inversion over a long crystal length is difficult to manufacture. A slight deviation in the QPM grating will lower the overall efficiency [84].

Beam quality of the blue light: The beam propagation factors of the generated blue light were determined to be better than M^2 = 1.25 in all cases with both crystals. The caustics of the generated blue light using the 40 mm long PPLN crystal are depicted in Fig. 7.9 at the maximum SHG output power. Beam propagation factors of M_x^2 = 1.21 for the slow-axis and M_y^2 = 1.14 for the fast-axis have been determined. For this measurement a lens with f = 50 mm was used. The beam waist position were measured to be $z_{0,fast}$ = 43.8 mm and $z_{0,slow}$ = 43.7 mm which indicated a good astigmatic correction. However, the astigmatism of the pump light had only low impact on the opto-optical conversion efficiency.

Spectrum and tunability of the blue light: Figure 7.10 shows a logarithmic plot of the spectrum of the blue laser emission at an injection current of 2.9 A. The bandwidth of the
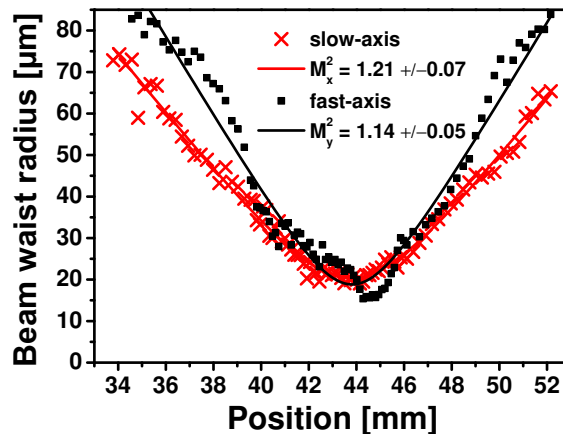
Figure 7.9: Caustics of the beam waist radii for slow and fast-axis of the generated blue light measured at maximum SHG output power using the 40 mm long PPLN bulk crystal and the off-axis ECDL.

blue laser radiation was measured to be 55 pm which is almost resolution limit of the OSA. A side mode suppression of better than 40 dB was determined.

The bandwidth of the off-axis ECDL emission was measured to be in the range of 1.8 MHz (see figure 5.14 b on page 51). This is well below the wavelength acceptance bandwidth of the two bulk crystals, which was measured to be 160 pm/cm (see table 7.1 on page 76). During the measurement, the bandwidth of the pump laser emission was monitored with an FPI with an FSR of 50 GHz and no multimode behavior was observed. Thus, the bandwidth of the blue light is assumed to be well below the 50 pm of the OSA measurement. However, an FPI for the blue spectrum was not available.
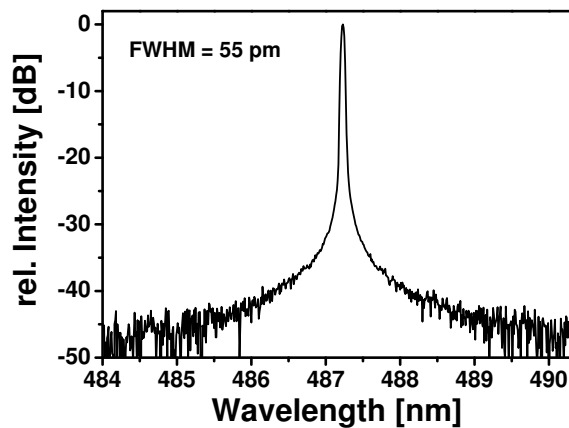
Figure 7.10: Spectrum of the generated blue light at the maximum SHG output power using the 40 mm long PPLN bulk crystal and the off-axis ECDL.

By changing the crystal temperature, the QPM grating and therefore the SHG wavelength could be changed. If the pump laser wavelength was simultaneously changed and adjusted to achieve maximum SHG conversion efficiency, the wavelength of the generated blue light was tunable. The SHG wavelength for the 40 mm long PPLN bulk crystal is depicted in Fig. 7.11 as a function of the crystal temperature. From near room temperature (T = 21°) to a temperature of 80°C the blue light was tunable over a range of more than 2 nm from 487.1 nm to 489.3 nm. The 10 mm crystal showed a very similar tuning behavior. The temperature coefficients were ≈ 0.04 nm/K for both crystals.
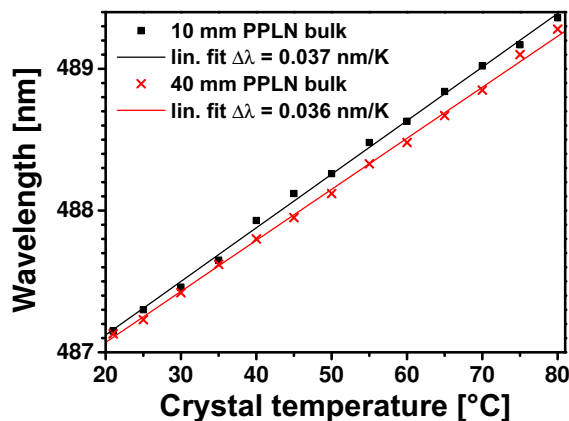
Figure 7.11: SHG wavelength as a function of the crystal temperature using the 40 mm long PPLN bulk crystal and the off-axis ECDL.

7.2.2 SHG with waveguide crystals

Experimental setup: For the frequency doubling using the waveguide crystals, the experimental setup was modified compared to the bulk crystal setup as is shown in Fig. 7.12. The setup of the off-axis ECDL remained unchanged. This time only one cylindrical lens (L1) with $f = 150$ mm was used to collimate the ECDL emission in slow-axis direction. To control the astigmatism this lens was mounted on a precision translation stage.

The PPLN waveguide crystal had a length of 10 mm a width of 3 mm and a height of 0.5 mm. Buried waveguide channels each with dimensions of 3.5 μm x 5 μm were applied by proton exchange. The QPM grating was optimized for SHG at a wavelength of 488 nm and a temperature of approximately 120°C. The infrared light was coupled into a waveguide channel of the PPLN crystal by using an aspherical lens L2 with f = 3.3 mm and NA = 0.47 (*Thorlabs C414TM-B*).

The 12 mm long PPKTP waveguide crystal had waveguide channels with dimensions of 4 μm x 8 μm. In this case, an aspherical lens (L2) with a focal length of f = 4.5 mm and NA = 0.55 (*Thorlabs C230TM-B*) was used. Both aspherical lenses had an AR coating for the pump wavelength. For both crystals, the highly diverging light at the output facet of the waveguide crystal was collimated with another aspherical lens (L3) with f = 8 mm and NA = 0.5 (*Thorlabs C240TM-A*). This lens was AR coated for the visible spectral range.
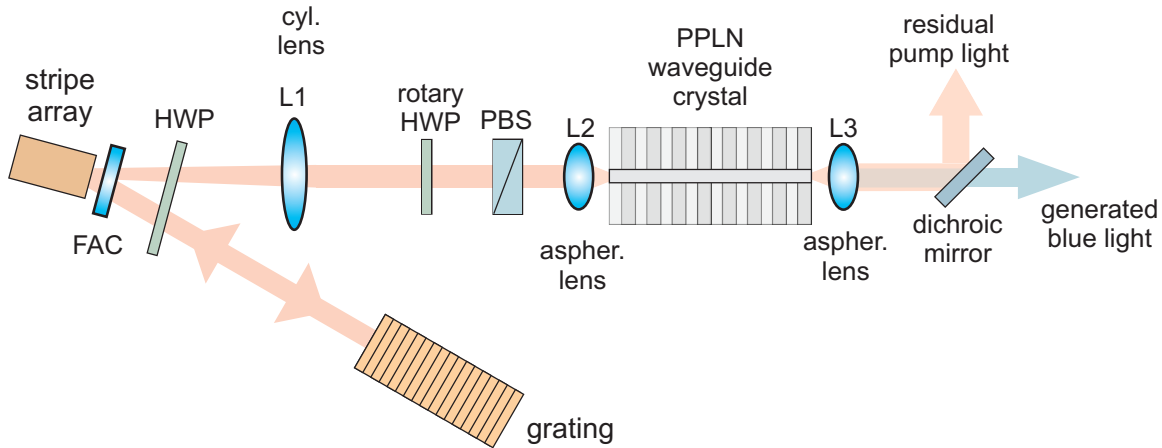
Figure 7.12: Schematic drawing of the frequency doubled off-axis ECDL using PPLN waveguide crystals. L1 cylindrical lens (slow-axis), L2 aspherical coupling lens, L3 aspherical collimation lens, HWP (half wave plate), PBS (polarization beam splitter).

Laser to waveguide coupling efficiency: For both crystals, the astigmatism of the ECDL emission was a critical value for the coupling efficiency. The caustic behind the aspherical lenses could not be measured with the *Beamscope*. Thus, the astigmatism was pre-adjusted by measuring the caustics behind a round lens with $f = 50$ mm and aligning the position of the slow-axis collimation lens. The laser to waveguide coupling was optimized during the SHG experiments by fine tuning the position of this lens. Because the astigmatism changed for different injection currents, the off-axis ECDL was operated at a fixed injection current and the astigmatism was optimized for this operating point. If the laser to waveguide coupling was not optimized, higher waveguide modes could be excited. This is shown in Fig. 7.13 for (a) the excitation of higher waveguide modes (TEM$_{2,0}$) due to an insufficient astigmatic correction and (b) good astigmatic correction.
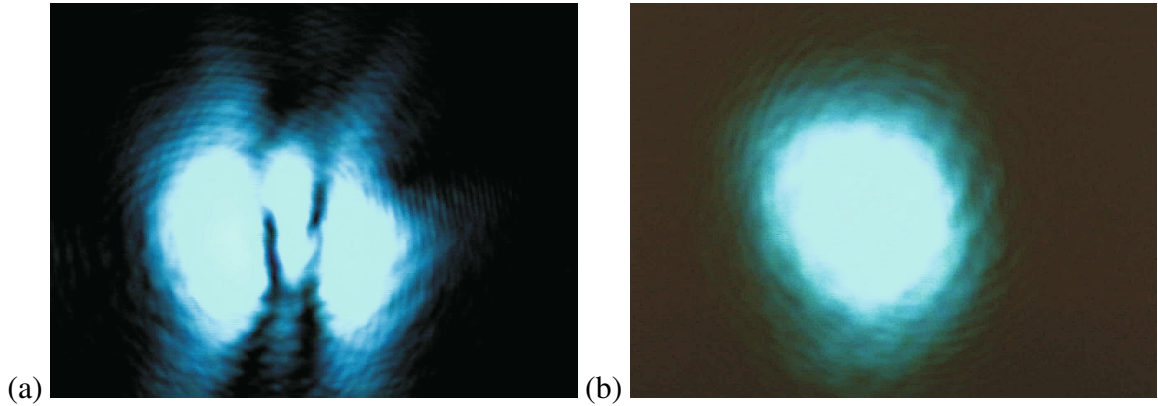
Figure 7.13: Beam profile of the generated blue light using the PPLN waveguide crystal for (a) insufficient astigmatic correction and (b) good astigmatic correction.

Table 7.2 shows the output power P_{IR} of the off-axis ECDL emission incident at the crystal, the coupled power $P_{IR,coupled}$ into the waveguide and the coupling efficiency for different injection currents J_{pump} with the PPLN waveguide crystal. The highest power of 322 mW could be coupled into the waveguide at an injection current of 1.8 A. At lower injection currents the coupling efficiency was slightly higher.

At injection currents higher than 2.0 A, the coupling efficiency decreased to values below 50%. Since the brightness of the off-axis ECDL emission did not increase significantly for injection currents higher than 2.2 A (see Fig. 5.10 on page 49), the SHG experiment was not performed at higher injection currents to prevent a damage of the crystal. A further increase of the injection currents would have resulted in high intensities at the input facets of the waveguide crystal.

The beam quality had a strong impact on the coupling efficiency. As can be seen from the measurement of the beam propagation factors as a function of the injection current (see Fig. 5.9 on page 49) the beam quality decreased more rapidly above injection currents of 1.9 A. This can also be seen in Fig. 5.10 on page 49.

The coupling efficiency achieved with the PPKTP waveguide crystal was significantly lower, because of the uncoated crystal facet and the strongly asymmetric waveguide. At an injection current of 1.8 A and 500 mW of pump power incident at the crystal, a maximum infrared power of 180 mW could be coupled into the waveguide PPKTP. This results in

J_{pump}[A]	P_{IR}[mW]	$P_{IR,coupled}$ [mW]	coupling eff. [%]
1.6	402	270	67.1
1.7	451	299	66.2
1.8	503	322	64.0
1.9	558	320	57.3
2.0	605	300	49.6
2.1	649	305	46.9
2.2	694	312	45.8

Table 7.2: Output power P_{IR} of the off-axis ECDL emission incident at the crystal, coupled power $P_{IR,coupled}$ into the waveguide and coupling efficiency for different injection currents J_{pump} determined with channel 9 of the PPLN waveguide crystal.

a coupling efficiency of 45% referenced to the Fresnel losses due to the uncoated facets of the crystal (which results in a maximum transmission of 82%). The beam quality of the pump light had approximately the same impact on the coupling efficiency as with the PPLN crystal.

Output power of the blue light: The power of the generated blue light P_{SHG} as a function of the coupled power of the infrared pump light $P_{IR,coupled}$ with the off-axis ECDL as pump laser is shown in Fig. 7.14 (a) for the 10 mm long PPLN waveguide crystal and Fig. 7.14 (b) for the 12 mm long PPKTP waveguide crystal.

The PPLN waveguide crystal had 16 waveguide channels applied. The measurements from the two channels with the best performance are depicted in Fig. 7.14 (a). With channel number 9 (black squares), the highest SHG output power could be achieved while channel 4 (red dots) showed the highest conversion efficiency. The injection current of the stripe-array was fixed at 1.8 A, where the ECDL yielded an infrared optical power of 500 mW incident at the crystal. At this operating condition, it was possible to couple 322 mW into channel 9 which represents a coupling efficiency of 64%.

With this coupled power, a maximum blue output power of 142 mW could be obtained in channel 9. This gives a conversion efficiency of 44.1% inside the crystal. In channel 4, up to 280 mW could be coupled and a maximum output power of 133.5 mW was achieved which corresponds to 47.6% conversion efficiency.

To calculate the conversion efficiency in this case, pump depletion has to be taken into account. The power of the generated light will have a $\tanh^2$ dependency on the power of the pump light (see equation 6.18 on page 68).

The $\tanh^2$ fit of the data measured with the PPLN crystal resulted in normalized conversion efficiencies of $\eta_{wg} = 230\%/W\cdot cm^2$ (channel 9) and $\eta_{wg} = 270\%/W\cdot cm^2$ (channel 4), respectively. At higher optical powers, a slight deviation from the predicted dependence was observed which is presumably caused by absorption. Furthermore, a quadratic fit curve (dashed line) with $220\%/Wcm^2$ was added to the graph. It shows a good agreement to the approximation for the lower conversion efficiencies. To avoid damage of the crystal surface the injection current was not raised above 2.2 A during the measurements because the laser to waveguide coupling efficiency dropped far below 50% for higher injection currents. It was not possible to couple more than 320 mW of the infrared light into the waveguide.

(a)   (b)
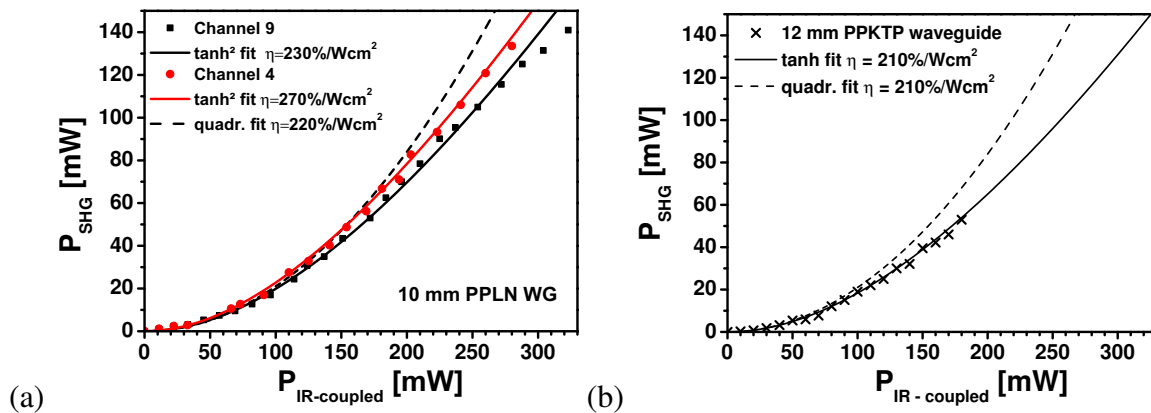
Figure 7.14: Power of the generated blue light (P_{SHG}) as a function of the infrared pump power coupled to the waveguide channel ($P_{IR,coupled}$) of (a) the 10 mm long PPLN waveguide crystal for two different channels and (b) the 12 mm long PPKTP waveguide crystal.

   With the PPKTP waveguide crystal blue light with a maximum SHG output power of 53 mW could be generated as shown in Fig. 7.14 (b). The normalized conversion efficiencies of $\eta_{wg} = 210\%/W\cdot cm^2$ obtained from the $\tanh^2$ fit of the data was in the same range as for the PPLN waveguide. The main limiting factor of the achieved output power was the coupling efficiency.

Beam quality of the blue light: Beam propagation factors of better than $M^2 = 1.15$ have been obtained in all cases with the PPLN waveguide crystal. Figure 7.15 (a) shows the caustics of the blue light generated with the PPLN waveguide crystal at optical output power of 88 mW. The beam quality with $M_x^2 = 1.01$ and $M_y^2 = 1.1$ was better than for the pump laser and with the bulk SHG. Since the waveguide acts as a spatial filter, only the diffraction limited part of the pump light is coupled to the waveguide and converted, respectively. Thus, the beam quality of the generated light depends on the quality of the waveguide, while the beam quality of the pump light has a huge impact on the coupling efficiency. The slightly elliptical beam and the asymmetric beam propagation factors are caused by the different size of the waveguide channels in x- and y- direction, respectively.

   From the caustics of the blue light generated using the PPKTP waveguide as depicted in Fig. 7.15 (b) beam propagation factors of better than $M^2 = 1.4$ have been calculated. The M^2 values indicate a lower beam quality than with the PPLN waveguide, which can be caused by the larger waveguide channel size of the PPKTP crystal.
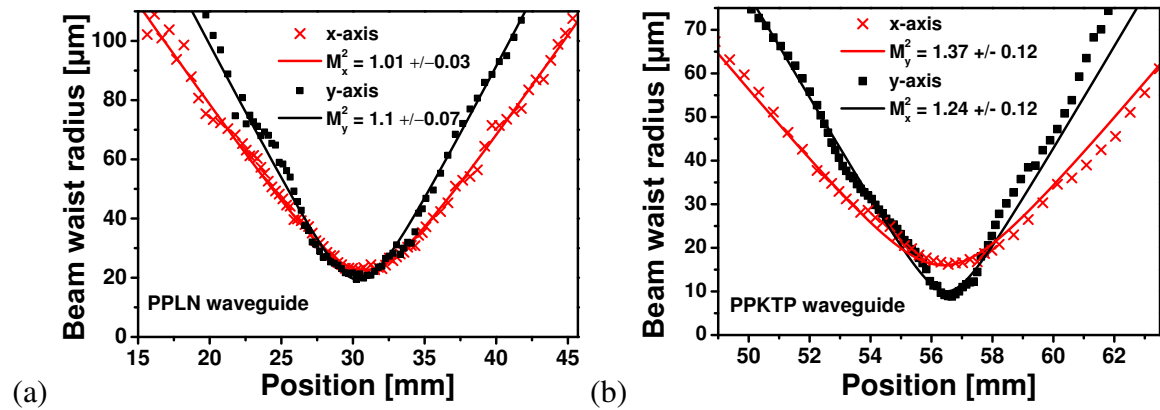
Figure 7.15: Caustics of the beam waist radii for slow and fast-axis of the generated blue light using (a) the 10 mm long PPLN waveguide crystal and (b) the 12 mm long PPKTP waveguide crystal.

Spectrum and tunability of the blue light: The spectra of the blue laser emission are shown in Fig. 7.16 (a) for the PPLN waveguide and (b) for the PPKTP waveguide. The PPLN waveguide was operated at a crystal temperature of $\vartheta = 130°C$. A wavelength of 488.2 nm was determined at an optical output power of 88 mW.

   A wavelength of 487.89 nm was measured with the PPKTP crystal at a crystal temperature of $\vartheta = 26°C$ and an optical output power of 51 mW. In both cases, the measured bandwidth of 50 pm was near the resolution limit of the OSA and side mode suppression ratios in the range of 50 dB were observed. Again the bandwidth of the pump laser was monitored using an FPI with an FSR of 50 GHz without the detection of higher longitudinal modes. As with the bulk crystals, the SHG wavelength could be tuned by changing the crystal temperature. With the PPLN waveguide crystal it was possible to obtain a tuning range

(a)   (b)
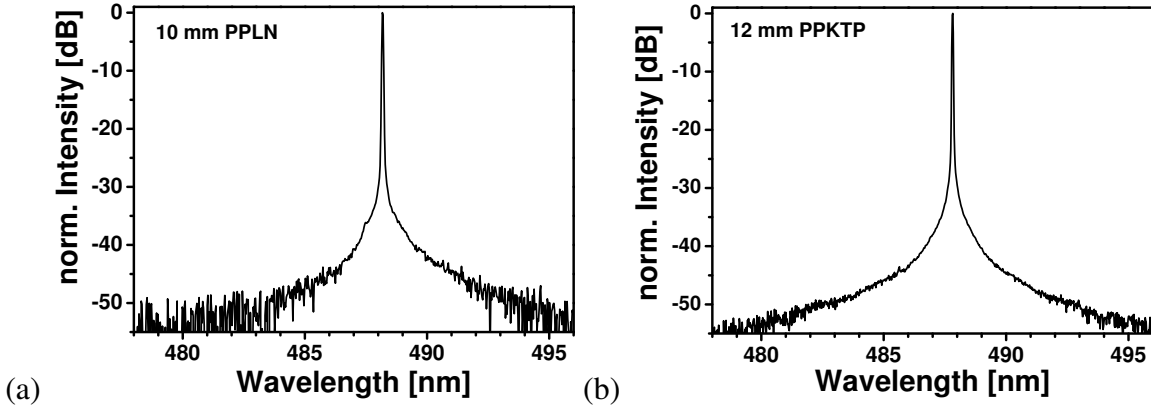
Figure 7.16: Spectra of the generated blue light using (a) the 10 mm long PPLN waveguide crystal and (b) the 12 mm long PPKTP waveguide crystal (right).

of more than 5.6 nm in the blue spectrum by changing the crystal temperature as shown in Fig. 7.17 (a). Near room temperature at $\vartheta = 25°C$ the SHG wavelength was 484.0 nm and at $\vartheta = 165°C$ an SHG wavelength of 489.7 nm was measured. The temperature tuning coefficient was 0.04 nm/K.

Even near room temperature, output powers of more than 90 mW have been obtained. The frequency doubled off-axis ECDL was running stable at an injection current of 1.5 A and this output power for several hours. The maximum power fluctuations were below 1%. No phase distortions or SHG wavelength shift that would indicate photo-refractive effects were observed during the measurements.

With the PPKTP crystal, the SHG wavelength could be tuned over a range of 1.5 nm, as shown in Fig. 7.17 (b). By changing the crystal temperature from $\vartheta = 22°C$ to $\vartheta = 80°C$ the wavelength of the blue light could be changed from 487.7 nm to 489.2 nm. The temperature tuning coefficient of PPKTP was lower than for PPLN with 0.025 nm/K. Furthermore, the PPKTP crystal was stabilized with a different heat sink that was only capable to achieve a maximum temperature of $\vartheta = 80°C$. However, the PPKTP crystal was explicitly designed for SHG near room temperature. In both cases, the tuning range was limited by the range of the crystal temperature controllers.

(a)   (b)

Figure 7.17: SHG wavelength as a function of the crystal temperature with (a) the 10 mm long PPLN waveguide crystal and (b) the 12 mm long PPKTP waveguide crystal.

7.2.3 Summary

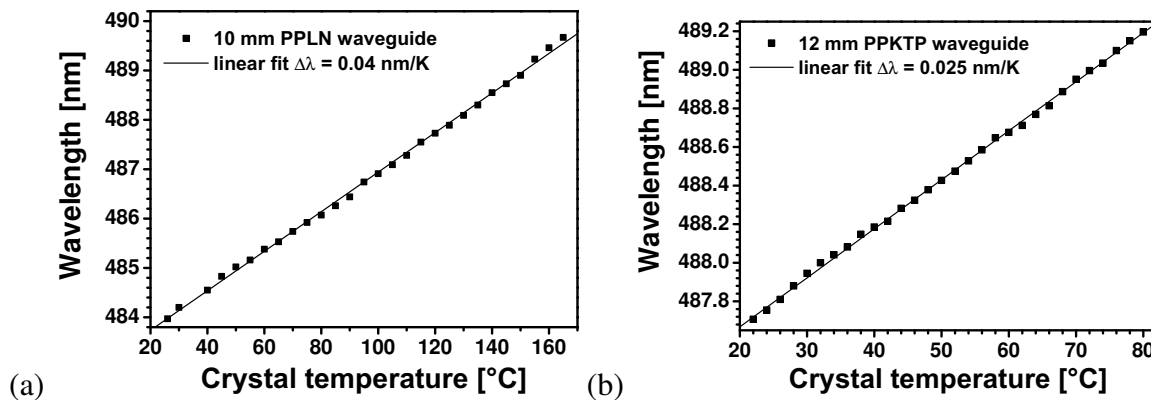With the off-axis ECDL that was developed in the first part of this thesis, it was possible to realize highly efficient frequency conversion from the infrared to the blue spectral range. Single pass SHG at a wavelength of 488 nm was performed using four different nonlinear crystals.

With the bulk PPLN crystals, output powers in the blue spectral range of up to 57.5 mW could be achieved. An opto-optical conversion efficiency of 6.7% and an electro-optical efficiency of 1.5% could be obtained by using the 40 mm long PPLN bulk sample. Furthermore, the generated light showed excellent beam quality, a narrow bandwidth and was tunable over a range of more than 2 nm. The bulk crystal SHG setup was not susceptible to astigmatism and mainly limited by the output power and the beam quality of the off-axis ECDL system. The SHG output power was approximately two orders of magnitudes higher than that reported in the literature with similar setups.

Samsøe et al. used a BA ECDL system to generate blue light with a PPKTP bulk crystal in a single pass configuration [78]. In this approach a 10 mm long PPKTP crystal was used. The ECDL comprised a standard BA diode laser and yielded 405 mW cw emission at 808 nm with an $M_x^2 \approx 3$. Blue light at 405 nm with an output power of 0.5 mW was generated.

Furthermore, it was possible to demonstrate single pass SHG using PPLN and PPKTP waveguide crystals pumped with the off-axis ECDL. By using a 10 mm PPLN waveguide crystal operated at a temperature of approximately 125°C, blue light at 488 nm with output powers of up to 142 mW could be generated. The blue light showed a very good beam quality and a narrow emission bandwidth. At an injection current of 1.8 A and an infrared pump power of 503 mW, a maximum optical power of 322 mW could be coupled into the waveguide channel. The laser to waveguide coupling efficiency in this case was 64%. An internal conversion efficiency of 47.6% inside the crystal could be achieved, while the opto-optical conversion efficiency was 28.2% including the laser to waveguide coupling losses. The normalized conversion efficiency was calculated to be 270%/Wcm^2. The electrical power was 2.4 W, resulting in a wall plug efficiency of 5.9%. The output power of the frequency doubled off-axis ECDL was not limited by photo-refraction. Rather, the coupling efficiency of the pump light decreased at higher injection currents which was the bottleneck of the SHG with the off-axis ECDL utilizing the waveguide crystals.

However, the PPLN waveguide crystal was designed to be operated at high temperatures to avoid photo-refractive damage. This made the thermal management and a further decrease of the setup size challenging.

As an alternative to PPLN, a PPKTP waveguide designed for SHG near room temperature was investigated. With this crystal, blue light at 488 nm with an output power of 53 mW could be generated. The output power of the blue light was limited by the high coupling losses because of the uncoated facets of the crystal and the asymmetric shape of the waveguide. Nevertheless, the normalized conversion efficiency achieved with the PPKTP crystal was not much lower than the values obtained with the PPLN waveguide crystal.

With a flat polished PPKTP waveguide with a more symmetric and smaller waveguide, higher output powers comparable to the PPLN waveguide should be feasible. KTP has the advantage that the wavelength and temperature acceptance bandwidths are higher than in LN. Therefore, the requirements to temperature controlling are lower even if longer crystals are used. Furthermore, KTP possesses a higher damage threshold and is less susceptible to photo refraction and induced absorption. The lower nonlinear coefficient does not come into play in waveguide crystals. Thus, PPKTP is the more promising solution for further

work despite the lower performance in this experiment.

The resulting electro-optical efficiency for the blue light generated with the PPLN waveguide was 5.9% which represents the highest wall plug efficiency achieved with a BA or off-axis ECDL system and single pass frequency conversion.

Apart from work not included in this thesis [129], this is the first time that BA or stripe-array diode lasers could be utilized for efficient SHG with waveguide crystals. Due to the in depth study of the stripe-array amplifier, the overall efficiency could be increased and the footprint could be diminished. The waveguide SHG setup fitted a breadboard with a size of 100 mm x 250 mm. Since the limiting factor for the size was the focal length of the optics, it should be possible to reduce the size further by using commercially available beam shaping optics.

7.3 Frequency doubling using an external cavity enhanced tapered amplifier

Tapered lasers are capable to deliver several Watts of output power with very good beam quality and are state of the art high brightness diode lasers [32, 130]. To achieve narrow bandwidth emission, they can be fabricated with on chip Bragg gratings [131]. Furthermore, when AR coatings are applied on both facets a TA is realized. Such TAs can be operated in a MOPA setup or in an external cavity [132, 133]. All three schemes are suitable for nonlinear frequency conversion.

In this chapter, an external cavity enhanced TA is used for SHG with the 40 mm bulk PPLN crystal. The experimental results are compared with the results obtained with the off-axis ECDL.

Experimental setup

The experimental setup of the frequency doubled TA-ECDL utilizing the 40 mm long PPLN bulk crystal is depicted in Fig 7.18. The TA (*m2k-BTAL-970-2000*) had a chip length of 2.5 mm and featured a 2 mm long tapered section with a full tapered angle of 6°, resulting in a emitter size of 1 x 215 μm^2. The ridge section was 500 μm long and had a width of ≈ 5 μm. In vertical direction a 1.06 μm AlGaAs waveguide core with 20% Al that comprised an InGaAs quantum well with a thickness of about 7 nm was sandwiched between two 1.06 μm thick AlGaAs claddings with an Al content of 40%. This layer structure is comparable to the large optical cavity design of the stripe-array as described in section 2.3.1 (see page 13 Fig. 2.5 (a)). However, the waveguide structure of the TA was slightly larger than for the stripe-array.

A rear Littrow configuration (section 2.4.1) was realized on the ridge section of the TA. For this purpose, the light emitted from the ridge was collimated with an aspherical lens (L1) with a focal length of $f = 4.5$ mm and NA = 0.47. In a distance of 250 mm a ruled diffraction grating with 1200 lines/mm was placed. The first order of diffraction of this grating was reflected back onto itself to form the oscillator. The grating lines were aligned parallel to the slow-axis and a half wave plate was used to suppress the losses at the zeroth order of the grating.

An aspherical lens (L2) with a focal length of $f = 6.5$ mm (NA=0.62) was used for the collimation of the fast-axis emission at the tapered side. Because of the strong astigmatism, this resulted in a focus in slow-axis direction. Furthermore, the beam profile was strongly
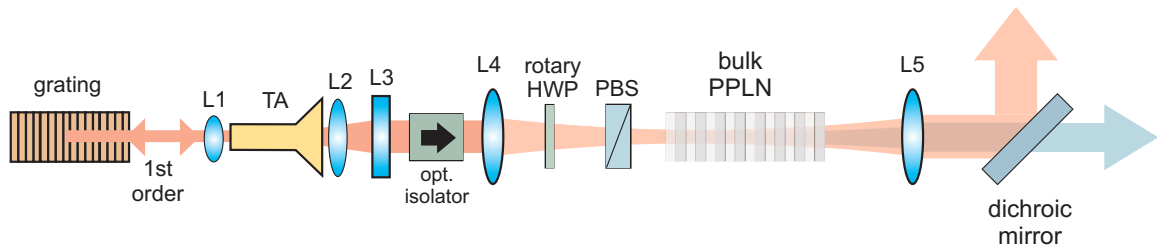
Figure 7.18: Experimental setup of the frequency doubled TA-ECDL utilizing a 40 mm long PPLN bulk crystal. The TA was operated in a rear Littrow external cavity setup using a diffraction grating (g = 1200 lines/mm). L1 aspherical lens f = 4.5 mm, L2 aspherical lens f = 6.5 mm, L3 cylindrical lens f_{slow} = 150 mm, HWP (half wave plate), PBS (polarization beam splitter), L4 focusing lens f = 125 mm, L5 collimation lens f = 100 mm.

elliptical. Both, astigmatism and ellipticity were corrected with a cylindrical lens (L3) with a focal length f_{slow} = 150 mm for recollimation of the slow-axis emission.

To individually control the pump currents injected at the ridge (J_{ridge}) and at the tapered section (J_{taper}), the chip was mounted p-side up and both sections were contacted separately. This has usually the drawback, that the heat conductivity is decreased and that the onset of thermal rollover is shifted to lower injection currents compared to p-side down mounted devices. To avoid thermal rollover a special heat sink was used (Fig. 7.19).

However, the individual current control of both sections has several advantages. If both sections have a common contact, a current overload on the ridge section can result in a severe decrease of the beam quality of the TA emission. Furthermore, facet degradation at the ridge side as well as filamentation and catastrophic optical mirror damage at the tapered section (which are typical BA laser problems), were observed. By controlling the injection currents individually, higher output powers and better beam quality of the emission can be achieved [49].

Figure 7.19: Picture of the tapered amplifier with separate contacts for ridge and tapered section on the high power heat sink. (Picture copyrighted by m2k-laser GmbH).

Experimental results

Infrared emission of the TA-ECDL: The optical output power of the TA-ECDL emission as a function of the injection current is depicted in Fig. 7.20, represented by the black
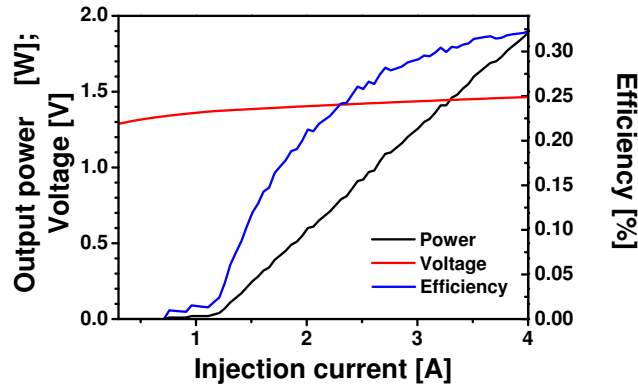
Figure 7.20: Optical output power, applied voltage and electro-optical efficiency of the TA-ECDL laser emission as a function of the injection current.

solid line. In this measurement the TA was operated with both sections connected to one power supply. Furthermore, the grating was adjusted to the gain maximum and no collimation lens was used. The laser threshold was determined to be at 1.2 A and the slope efficiency was 0.67 W/A. No saturation effects or thermal rollover were observed.

The solid line in Fig. 7.20 shows the applied voltage and the blue line is the calculated electro-optical efficiency. At an injection current of $J = 4$ A a maximum output power of $P = 1.9$ W was measured. The electro-optical efficiency was higher than 31% in this case.

However, if both sections are contacted separately a higher output power can be achieved if the ratio between the two injection currents is optimized. Figure 7.21 shows the output power of the TA-ECDL for five different fixed injection currents at the tapered section (J_{taper}) as a function of the injection current at the ridge side (J_{ridge}). At the lowest tapered section injection current of $J_{\text{taper}} = 1.0$ A, the output power remained nearly constant when the injection current at the ridge section was increased. For higher injection currents, the output power can depend strongly on the injection current at the ridge side. For example, at an injection current of 3.0 A at the tapered section the output power of the TA-ECDL laser did increase from approximately 1 W to 1.7 W if the ridge injection current was increased from 50 mA to 150 mA.

The ratio between ridge and tapered injection current is also critical for the slow-axis beam propagation factor and the bandwidth of the TA-ECDL emission. At lower TA in-
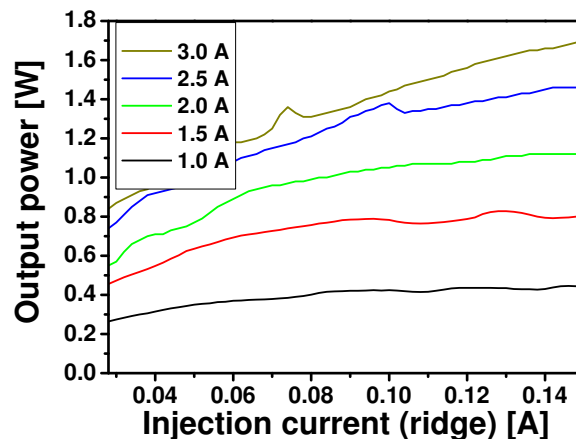
Figure 7.21: Optical output power for different injection currents at the tapered amplifier section (J_{taper}) as a function of the injection current at the ridge side (J_{ridge}).

J_{taper} [A]	J_{ridge} [mA]	P_{opt} [mW]	M_x^2	M_y^2	B [MW/cm^2-sr]	$\Delta\lambda$ [pm]
3.0	50	1100	1.35	1.55	54.8	84
	100	1400	1.41	1.55	66.8	51
	150	1700	1.69	1.56	67.7	51
3.5	50	2200	1.59	1.63	89.1	73
	100	2300	1.61	1.63	92.0	62
	150	2400	1.99	1.62	77.7	63
4.0	50	2300	1.42	1.72	98.9	83
	100	2550	1.58	1.73	97.9	78
	150	2650	2.17	1.71	74.5	86

Table 7.3: Optical output power P_{opt}, beam propagation factors M_x^2 and M_y^2, brightness B and laser emission bandwidth $\Delta\lambda$ of the TA-ECDL emission at different injection currents.

jection currents than 2.5 A, the slow-axis beam propagation factors did not show a strong dependence on the ridge injection currents. This changed at higher TA injection currents, where the slow-axis beam quality depended strongly on the ridge injection currents.

Table 7.3 shows the measured values for three different injection currents at the tapered section, ranging from 3.0 A to 4.0 A. The ridge injection current was changed from 50 mA to 150 mA. In all cases, the TA-ECDL emission had a better slow-axis beam quality for lower ridge injection currents. The impact of the ridge injection current on the beam propagation factors in fast-axis direction was only marginal, where a linear increase with TA injection current was observed.

The highest brightness of 98.9 MW/cm^2-sr was obtained at an injection current of $J_{\text{taper}} = 4$ A at the tapered section and 50 mA injected into the ridge section. However, the emission bandwidth (measured with the OSA) did also increase with higher injection currents at the tapered section. The wavelength acceptance bandwidth of the 40 mm long PPLN crystal used in this experiment was $\Delta\lambda_{\text{Crystal}} = 39$ pm. The bandwidth of the TA-
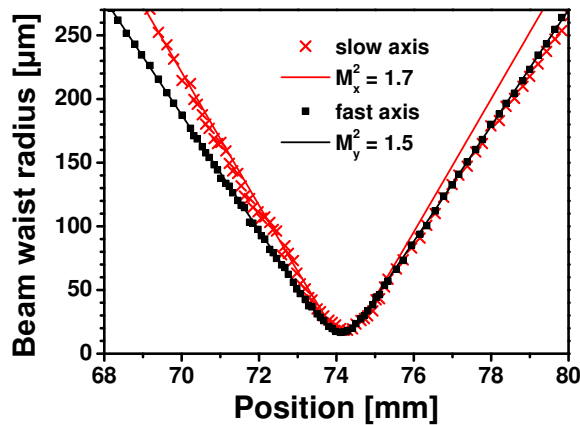
Figure 7.22: Caustics of the TA-ECDL emission for both axes at injection currents of $J_{\text{taper}} = 3$ A $J_{\text{ridge}} = 150$ mA. The optical output power was $P_{\text{opt}} = 1.7$ W.
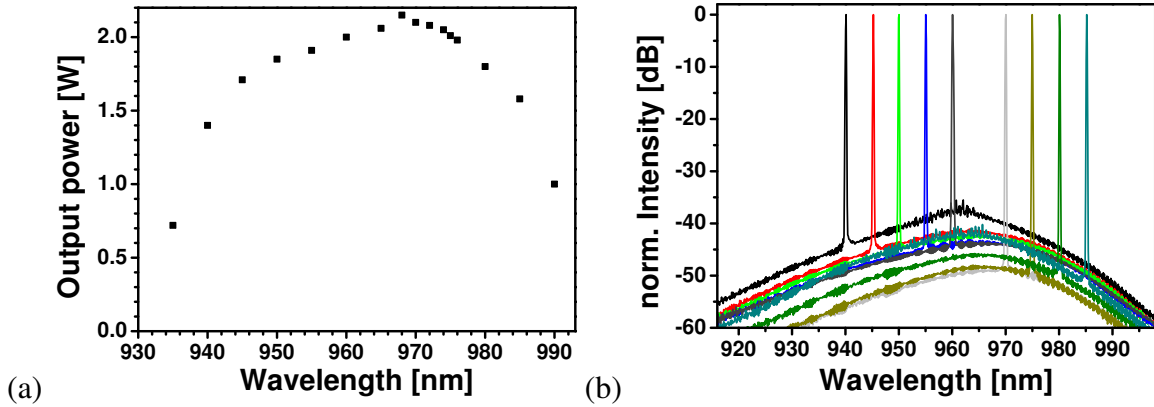
Figure 7.23: (a) Optical output power and (b) spectrum measured with an OSA of the TA-ECDL emission as a function of the emission wavelength at an injection current of $J_{\text{taper}} = 3.5$ A and $J_{\text{ridge}} = 100$ mA.

ECDL emission exceeded this value by a factor of two at an injection current of $J_{\text{taper}} = 4$ A at the tapered section.

The caustics of the TA-ECDL laser emission for both axes at injection currents of $J_{\text{taper}} = 3$ A $J_{\text{ridge}} = 150$ mA are depicted in Fig. 7.22 measured with a spherical lens with $f = 50$ mm. The optical output power was $P_{\text{Opt}} = 1.7$ W at this operating condition. Beam propagation factors of $M_x^2 = 1.69$ in slow-axis direction and $M_y^2 = 1.56$ in fast-axis direction have been measured. The difference between the beam waist radius positions in the two directions was below 0.1 mm in this case, indicating a good correction of the astigmatism.

The output power as a function of the emission wavelength is depicted in Fig. 7.23 (a), the corresponding spectra are shown in Fig. 7.23 (b). The ridge injection current was 100 mA during all these measurements.

The emission wavelength was tunable over a range of 56 nm from 934 nm to 990 nm. The gain maximum was located at 968 nm and a maximum output power of $P_{\text{opt}} = 2.15$ W was measured. At a wavelength of 976 nm the output power was 1.98 W. The tuning range at the FWHM was larger than 40 nm. The spectra measured with the OSA showed side mode suppression ratios of better than 35 dB even at the edges of the tuning range. At a wavelength of $\lambda = 976$ nm, the side mode suppression ratio was above 50 dB.

Frequency doubled TA-ECDL

To avoid back reflections from the nonlinear crystal into the tapered section, an optical isolator was set up behind the collimation optics of the ECDL. To adjust the pump power incident at the crystal and to rotate the polarization of the TA emission, an attenuator consisting of a polarization beam splitter and a rotary half wave plate was used. The half wave plate was necessary, because the z-axis of the nonlinear crystal was positioned perpendicular to the slow-axis of the TA and thus the (TE polarized) emission of the TA-ECDL had to be rotated by 90°.

With a spherical lens with $f = 125$ mm, a focus with a slight residual ellipticity and beam waist radii of $w_{0,\text{fast}} = 31$ μm and $w_{0,\text{slow}} = 36$ μm was generated. The deviation from the optimum focusing condition (equation 6.14) ($w_0 = 31.8$ μm) was only marginal. Collimation of the generated blue light was realized with another spherical lens having a focal length of $f = 100$ mm. The generated blue light was separated from the residual pump light by using a dichroic mirror (HT for 488 nm and HR for 976 nm).

The generated SHG output power at a wavelength of 488 nm is shown in Fig. 7.24 as a function of the infrared pump power incident at the 40 mm long PPLN bulk crystal. The TA-ECDL emission was tuned to an emission wavelength of 976.0 nm, which was slightly off the gain maximum. Furthermore, the optical system introduced loss and the pump power incident at the crystal was lower than the values given in the table.

The first five data points in Fig. 7.24 (up to a pump power of 1.5 W) have been obtained by operating the TA at $J_{\text{taper}} = 3.0$ A and $J_{\text{ridge}} = 150$ mA. The power incident at the crystal was varied by using the attenuator. In this case, the conversion efficiency was calculated to be $\eta_{\text{bulk}} = 3.6\%/\text{W} \cdot$ which is represented by the solid black line in the graph.

At higher injection currents, the conversion efficiency decreased. At an injection current of 3.25 A at the taper section and 150 mA at the ridge section, a pump power of 1.6 W was incident at the crystal. With this pump power, an SHG output power of 76 mW was realized.

An SHG output power of 93 mW could be generated at $J_{\text{taper}} = 3.5$ A and $J_{\text{ridge}} = 100$ mA. The highest SHG output power of 105 mW was realized at $J_{\text{taper}} = 3.5$ A and $J_{\text{ridge}} = 150$ mA with 2.1 W incident at the crystal.

By further increasing the pump power to 2.3 W ($J_{\text{taper}} = 4.0$ A, $J_{\text{ridge}} = 100$ mA), the power of the generated blue light did not increase. At this injection current, the conversion efficiency was $\eta_{\text{bulk}} = 2.0\%/\text{W}\cdot\text{cm}$.

The dashed line in Fig. 7.24 shows the fit through the data obtained with the same crystal and the off-axis ECDL as pump laser. The slope of the conversion efficiency η_{bulk} was more than two times higher with the off-axis ECDL laser system.
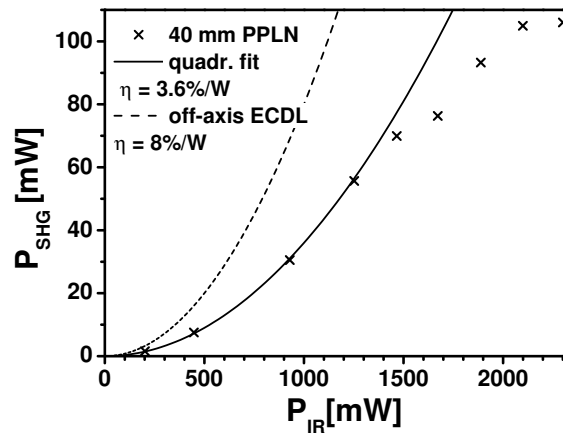
Figure 7.24: Optical output power of the generated blue light (P_{SHG}) as a function of the infrared pump power of the TA-ECDL emission (P_{IR}) using the 40 mm long bulk PPLN crystal.

As discussed in section 6.4, the SHG conversion efficiency depends on the beam quality and the wavelength acceptance bandwidth of the pump laser. The SHG output power scales approximately inversely linear with the beam quality (in both directions) $P_{\text{SHG}} \propto 1/M^4$ (see equation 6.17 on page 68). Furthermore, the SHG output power possesses a sinc dependence on the wavelength acceptance bandwidth as depicted in Fig. 6.5 on page 69.

Table 7.4 shows the two dimensional beam quality M^4, the ratio between acceptance bandwidth of the crystal and the measured bandwidth of the laser $\Delta\lambda_{laser}/\Delta\lambda_{acc}$ and the calculated conversion efficiency for three TA injection currents. As a reference, the values for the off-axis ECDL are given.

It can be assumed that the degradation of the beam quality and the bandwidth are the reasons for the rather low conversion efficiency of the TA-ECDL. However, with the TA-

J_{taper} [A]	M^4	$\Delta\lambda_{laser}/\Delta\lambda_{acc}$	η_{bulk} [%/Wcm]
(TA) **3.0**	2.2	1.3	3.6
(TA) **3.5**	2.6	1.6	2.1
(TA) **4.0**	2.7	2	2.0
off-axis ECDL	1.7	< 1	8.0

Table 7.4: Beam quality, bandwidth referenced to the crystal acceptance bandwidth and conversion efficiency for different TA injection currents. The off-axis ECDL is shown as reference.

ECDL a nearly two times higher SHG output power could be generated compared to the off-axis ECDL with the stripe-array amplifier because a higher pump power could be realized.

The tuning range that could be obtained with this setup was similar to the values obtained with the off-axis ECDL and limited by the range of the temperature controller. The spectra of the generated blue light measured with the OSA showed comparable results to that obtained with the frequency doubled off-axis ECDL. A bandwidth of 50 pm close to the resolution limit of the measurement device was obtained. A broadening of the bandwidth of the blue light was not observed because the wavelength acceptance bandwidth was below the resolution limit of the OSA. Since no FPI for the blue spectrum was available, the effect could not be fully resolved. Furthermore, the bandwidth of the pump light was not monitored with an FPI because it was not available during the measurements.

Summary

With an external cavity enhanced TA, near diffraction limited narrow bandwidth emission with an output power of up to 2.5 W could be realized. The TA-ECDL emission was tunable over a large range of more than 56 nm. This was slightly more than what was achieved with the off-axis ECDL. The influence of the ratio of the injection currents at ridge and tapered section was studied. A strong dependence of the slow-axis beam quality as well as the emission bandwidth was observed.

Finally, more than 100 mW of blue light at a wavelength of 488 nm could be generated in a single pass SHG experiment using the 40 mm long PPLN crystal. The conversion efficiency was two times lower than with the off-axis ECDL and the same PPLN crystal. It is assumed, that the bandwidth of the TA-ECDL emission was the main limiting aspect here. Since the resolution limit of the measurement device was larger than the acceptance bandwidth of the crystal, it was not possible to resolve this effect. However, because of the higher pump power provided by the TA-ECDL, the power of the generated light was two times higher than with the off-axis ECDL. Tuning of the blue light was possible over a range of more than 2 nm as with the off-axis ECDL.

Compared to the values reported in the literature with a similar setup, the output power could be increased by a factor of 4 [134]. Chi et al. used a 4 mm long TA with an emission wavelength of 810 nm operated in a Littrow ECDL. They achieved a blue output power of 24 mW at 405 nm in a single pass SHG setup using a 10 mm long PPKTP crystal.

However, Maiwald et al. could achieve 600 mW at 488 nm by using a MOPA consisting of a DFB master laser and a TA as pump source [135]. This setup was rather large and complex. In a recent work by Jensen et al. SHG output powers of up to 1.5 W have been reported. They used a tapered diode lasers with Bragg gratings to pump SHG in a 60 mm

long PPLN crystal [136].

Therefore, the conversion efficiency is supposed to be increased if the setup is further optimized. One possibility is the use of additional spectral filters such as etalons, other diffraction gratings or volume Bragg gratings to achieve a further decrease of the emission bandwidth.

7.4 Frequency doubling using a DFB ridge waveguide diode laser

The typical size of the emitting area of a single stripe diode laser with a super large optical cavity of 3 μm x 5 μm cross section is in the same range as the typical channel size of a nonlinear waveguide crystal. Thus, efficient coupling of the diode laser emission into such a waveguide channel is feasible with a moderate effort concerning the beam shaping optics. For efficient SHG with waveguide crystals neither need high pump powers nor long interaction lengths are required.

Here, a DFB ridge waveguide diode laser was used to pump SHG inside channel waveguide crystals in a bench top experiment. Therefore, the PPLN and PPKTP waveguide crystals described in section 7.1 have been utilized. The results are compared with the results obtained with the off-axis ECDL system described in section 7.2.

Experimental setup

Figure 7.25 shows the experimental setup. The DFB ridge waveguide diode laser was manufactured by the *FBH*, Berlin and is similar to the diode laser used in [137]. It has a length of 4 mm and an emitter size of 3 μm (fast-axis) x 5 μm (slow-axis). A detailed description of the layer structure can be found in [41]. The DFB diode laser was kindly provided by *Sacher Lasertechnik*. The emission of the DFB ridge waveguide diode laser was collimated with an aspherical lens L1 with a focal length of $f = 2.75$ mm (*Lightpath LPTH350390-B*). Behind this lens an ellipticity of 1:3 and a slight astigmatism was observed. For the correction of the astigmatic beam an anamorphic beam shaping optic L2 (*Schaefter + Kirchhoff 5AN-2A-05*) consisting of two cylindrical lenses was used. Behind this optic the ellipticity could be improved to values below 1:1.05 and the astigmatism nearly vanished.
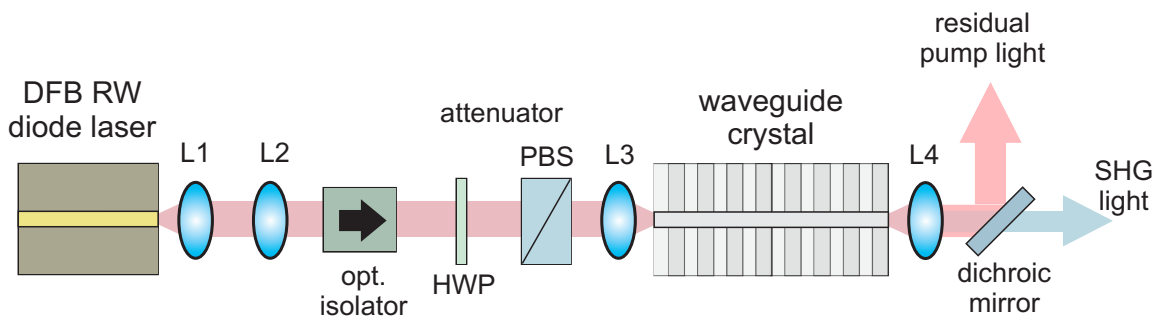

Figure 7.25: Experimental setup of the frequency doubled DFB diode laser using nonlinear waveguide crystals. HWP (half wave plate), PBS (polarization beam splitter), L1 aspherical collimation lens, L2 anamorphic beam shaping optic, L3 aspherical coupling lens, L4 aspherical collimation lens.

To avoid optical feedback from the nonlinear crystal back into the DFB laser, an optical isolator was introduced behind the collimation optics. The emission of the DFB ridge waveguide diode laser was TE polarized and a half wave plate was necessary to rotate the electric field of the laser emission. A polarization beam splitter was used behind the half wave plate adjusted to block TE polarized and transmit TM polarized light. Since the half wave plate was rotary an attenuator was formed. The power of the pump light could be adjusted by rotating the half wave plate, while the diode laser could be operated at a fixed injection current. This scheme provides maximum stability since the astigmatism and ellipticity can slightly change with changed injection current.

The well collimated pump light was coupled into the temperature stabilized waveguide crystals by using an aspherical lens. To focus into the 3 μm x 5 μm waveguide channel of the PPLN waveguide crystal an aspherical lens (L3) with a focal length of f = 3.1 mm (*Thorlabs C330TM-B*) and an NA = 0.68 was used. For the coupling of the pump light into the PPKTP waveguide crystal with a channel size of 4 μm x 8 μm an aspherical lens (L3) with a focal length of f = 6.2 mm (*Thorlabs A110TM-B*) was used. With both crystals, the highly diverging light at the waveguide channel output facet was collimated with another aspherical lens (L4) with a focal length of f = 8 mm (*Thorlabs C240TM-A*, NA = 0.5). For the separation of the fundamental infrared light from the generated blue light a dichroic mirror (HT 488/ HR 976) was used.

Experimental results

Characterization of the DFB ridge waveguide diode laser: The optical output power of the DFB diode laser behind the optical isolator as a function of the injection current is depicted in Fig. 7.26. The isolator had a transmission of 90%. The laser threshold was located at an injection current of 33 mA. Up to an injection current of 450 mA a slope efficiency of 0.74 W/A was observed. Above 450 mA the slope efficiency decreased slightly and the optical output power saturated around 700 mA.

Up to an injection current of 645 mA, the beam propagation factor of the DFB diode laser emission was determined to be better than M^2 <1.1 for both axes and in all cases. At 630 mA, the beam propagation factors were M_x^2 = 1.09 for the slow-axis and M_y^2 = 1.08 for the fast-axis, respectively. With a measured output power of P = 490 mW (before the isolator) this gives a brightness of 43.8 MW/cm^2·str. At injection currents higher than 650 mA, the slow axis beam quality degraded rapidly to $M_x^2 \approx 1.3$.

The bandwidth of the DFB laser emission was determined to be below 100 MHz by
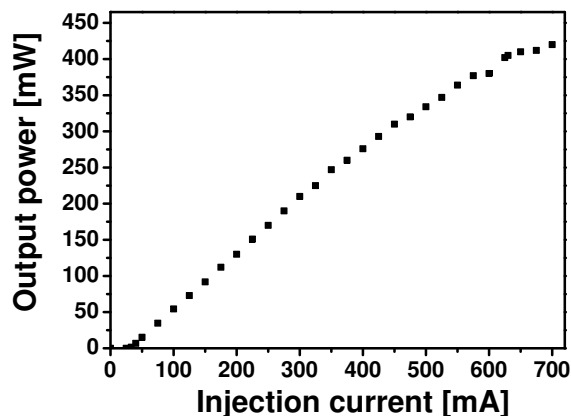
Figure 7.26: Output power of the DFB diode laser as a function of the injection current.
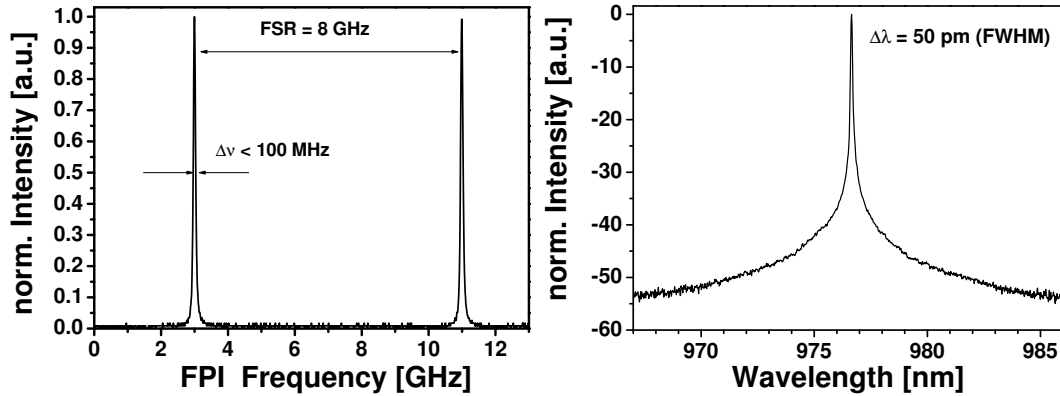
Figure 7.27: Spectrum of the DFB diode laser emission at an injection current of $I_{\mathrm{pump}} = 709$ mA and a temperature of $T_{\mathrm{DFB}} = 19.0°C$ (a) measured with an FPI and (b) measured with the OSA.

using a scanning FPI with an *FSR* of 8 GHz (Fig. 7.27 (a)). Furthermore, the optical spectrum was measured with an OSA as depicted in Fig. 7.27 (b). A side mode suppression ratio of better than 50 dB was observed and no additional peaks could be observed within the resolution limit of the OSA, which was 50 pm.

The emitted wavelength of the DFB laser is a function of the laser chip temperature and the injection current. Figure 7.28 shows the emission wavelength as a function of the diode laser heat sink temperature at an injection current of 709 mA. A tuning range of 0.8 nm was realized by changing the DFB diode laser temperature from $\vartheta = 16°C$ to $\vartheta = 26°C$. The linear fit through the measured data resulted in a temperature coefficient of $\Delta\lambda = 82.3$ pm/K.
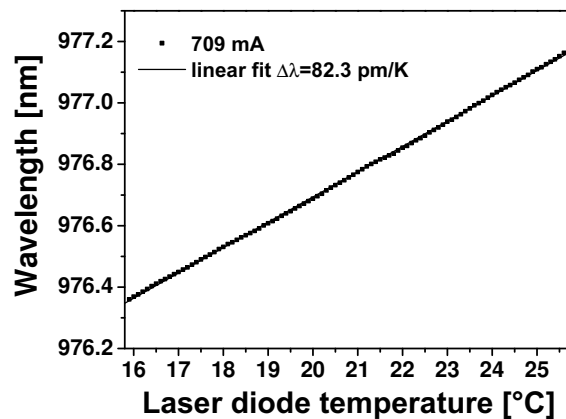
Figure 7.28: Wavelength of the DFB diode laser emission as a function of the diode laser temperature at an injection current $I_{\mathrm{p}} = 709$ mA and an optical output power of 500 mW.

Frequency doubled DFB diode laser using waveguide crystals: The DFB laser was operated at an injection of 630 mA, a voltage of 3.4 V and a temperature of 16° C. This resulted in emission at a wavelength of 975.6 nm with an optical output power of 405 mW incident at the crystal. At this operating point, a maximum laser to waveguide coupling efficiency of 75% was achieved into channel 4 of the PPLN crystal, resulting in a coupled infrared power of 304 mW. This was higher than the values obtained with the off-axis ECDL, because of the better beam quality of the DFB laser. The two dimensional beam quality was $M^4 = 1.17$ while the off-axis ECDL had $M^4 = 1.27$ at the maximum coupled

power. However, astigmatism and ellipticity have also an impact on the coupling efficiency. With the anamorphic beam shaping optics the astigmatism could be adjusted very precisely with the DFB laser. To determine the amount of the light coupled into the waveguide, the temperature of the PPLN crystal was detuned from the phase matching condition so that no blue light was generated and the transmitted infrared light was measured.

With the 12 mm long PPKTP waveguide crystal, a maximum coupled pump power of 220 mW could be achieved at the same operating condition. This gives a coupling efficiency of better than 65% including the Fresnel losses of the non AR coated facets of the PPKTP crystal, which was also better than the value achieved with the off-axis ECDL.

The optical output power of the generated blue light as a function of the optical power of the pump light coupled to the waveguide channel is depicted in Fig. 7.29. The black squares in this graph represent the data measured with the PPLN waveguide crystal. The red squares have been obtained with the PPKTP crystal.

With the maximum coupled power of 304 mW inside the PPLN waveguide channel, up to 159 mW blue laser light emission could be generated. This corresponds to an internal conversion efficiency of 52%. The overall opto-optical conversion efficiency was 39% including the coupling losses. The black line in Fig. 7.29 represents the $\tanh^2$ fit through the data. A normalized waveguide conversion efficiency of $\eta_{WG} = 290\%/\text{W}\cdot\text{cm}^2$ was calculated, which was approximately the same as with the off-axis ECDL.

By using the PPKTP crystal, blue light with a power of up to 66.7 mW was generated from 220 mW of coupled power. In this case, the internal conversion efficiency was 30% and the overall opto-optical conversion efficiency was $\eta_{opto} = 16\%$ including the coupling losses. The red line in Fig. 7.29 gives a normalized waveguide conversion efficiency of $\eta_{WG} = 210\%/\text{W}\cdot\text{cm}^2$ calculated from the $\tanh^2$ fit through the data. The higher output power compared to the off-axis ECDL is caused by the lower coupling losses. The conversion efficiency was the same.

Fig. 7.30 (a) shows the caustics for both axes of the light generated with the PPLN crystal at an injection current of 630 mA and an optical output power of 159 mW. A beam propagation factor of $M^2 < 1.05$ was obtained for both axis. A residual ellipticity of the beam was observed which is caused by the different aperture size of the waveguide in x and y direction. With the PPKTP crystal, beam propagation factors better than $M^2 < 1.4$ have been determined in all cases. Since the beam quality of the pump light was slightly better,
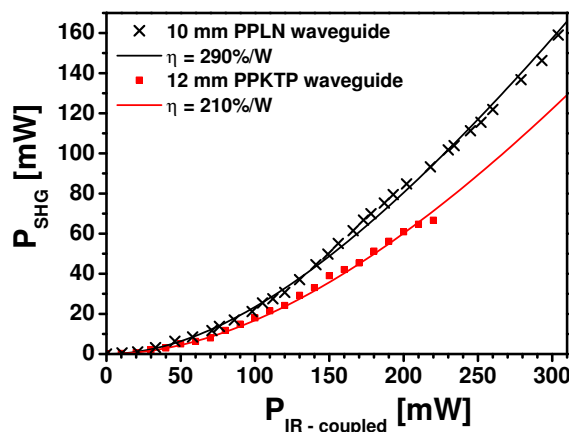
Figure 7.29: Power of the generated blue light (P_{SHG}) as a function of the infrared pump power coupled to the waveguide channel ($P_{IR-coupled}$) of a 10 mm long PPLN waveguide crystal (black) and a 12 mm long PPKTP waveguide crystal (red).

it is assume that the waveguiding in the crystal is not strong enough or that some phase distortions are present in the material. The same ellipticity as with the off-axis ECDL as pump laser was observed.
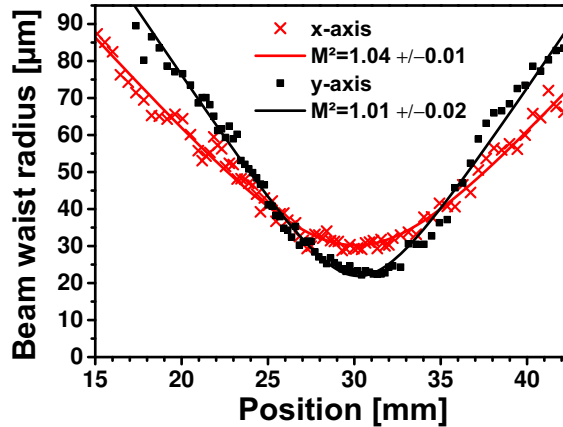
Figure 7.30: Caustics of the beam waist radii for slow and fast-axis of the generated blue light using the 10 mm long PPLN waveguide crystal.

The spectrum of the blue laser emission obtained with the PPLN waveguide crystal at an injection current of 630 mA and the maximum output power is shown in Fig. 7.31. The measured bandwidth of 51 pm was near the resolution limit of the OSA. A a side mode suppression of more than 40 dB has been observed. At a crystal temperature of 125°C, the QPM wavelength for SHG was 487.8 nm. During the experiment, the bandwidth of the pump laser was monitored with an FPI with an *FSR* of 50 GHz. No sign of longitudinal multimode operation was observed. Thus, the pump laser bandwidth was well below the crystal acceptance bandwidths. With the PPKTP crystal, similar spectral bandwidths and side mode suppression ratios have been measured.

The temperature tuning behavior of the two crystals was very similar to the values obtained with the off-axis ECDL. However, with the DFB laser the tuning range was mainly limited by the tuning range of the pump laser.
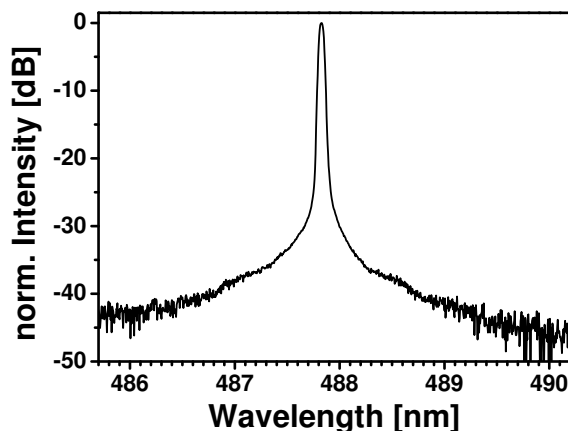
Figure 7.31: Spectrum of the generated blue light using the 10 mm long PPLN waveguide crystal measured with an OSA.

Summary

A compact and efficient laser system in the blue green spectrum based on a DFB ridge waveguide diode laser and nonlinear waveguide crystals was presented. By using the PPLN waveguide crystal, near diffraction limited, narrow bandwidth emission with a maximum output power of 159 mW could be generated at a wavelength of 488 nm. A record conversion efficiency of 52% inside the crystal was achieved. A normalized conversion efficiency of 290%/W·cm^2 was calculated. The overall wall plug efficiency was 7.4% at an injection current of 630 mA. Compared to the off-axis ECDL, a higher coupling efficiency was achieved and a slightly higher SHG output power could be realized. This is attributed to the excellent beam quality of the DFB diode laser and agrees with the investigations concerning the coupling efficiency made with the off-axis ECDL. At the chosen operating point, beam propagation factors of $M^2 < 1.1$ have been measured, which was slightly better than that of the off-axis ECDL.

The laser system could be operated stable for several hours at an output power of 150 mW without observing any photo-refractive effects or blue induced infrared absorption. However, the problem of the thermal management due to the different operating temperatures of crystal and diode remained. The PPLN waveguide had to be stabilized above $\vartheta = 100°C$ and the diode was stabilized at $\vartheta \approx 20°C$.

With the PPKTP waveguide crystal, a lower coupling efficiency due to the non AR coated facet was observed. The output power was only 66.7 mW with this crystal and the beam quality was slightly worse. However, for further integration into a compact device the PPKTP crystal is more promising because of the higher optical damage threshold and the lower requirements on the temperature controlling. KTP can be operated near room temperature and the temperature acceptance bandwidth is three times broader than for LN.

With the 40 mm long bulk crystal SHG output powers below 10 mW were achieved, but the results are not presented here.

The combination of a DFB or a distributed Bragg reflector (DBR) diode laser and a waveguide crystal has the potential for further miniaturization. Recently, Wiedmann et al. demonstrated a small scale device with a DBR ridge waveguide diode laser butt coupled to a PPLN waveguide. An SHG output power of up to 35 mW green light at 530 nm could be achieved [138]. Maiwald et al. [137] could demonstrate a miniaturized SHG device consisting of a DFB ridge waveguide diode laser lens coupled to a ridge waveguide PPLN crystal. Micro-optics have been used for coupling and collimation and were assembled on a heat sink with a footprint of 25 x 5 mm^2. With less than 1 W electrical power a maximum output power of 56 mW at 488 nm could be demonstrated with a power stability of 1%. The device had a combined thermal management for laser and crystal and can be used as a mobile sensor for raman spectroscopy.

In this work, a benchtop setup comprising an optical diode was realized. Thus, the footprint size was much larger than these integrated devices and even larger than the off-axis ECDL system since no optical isolator was used there. The output power of the system presented here was limited by the power incident at the crystal. This scheme can be used to realize compact integrated SHG devices. However, a challenging aspect for the miniaturization of a diode laser based SHG device utilizing nonlinear waveguide crystals is the long term stability of the laser to waveguide coupling.

7.5   Conclusion

In this chapter, three diode laser systems have been used for efficient frequency doubling
to the blue spectral range. For this purpose four nonlinear crystals exploiting the effect of
QPM have been utilized. Two bulk and two waveguide crystals have been characterized
and applied to SHG.

With the off-axis ECDL that was developed as a part of this thesis, SHG with all four
nonlinear crystals have been performed. More than 140 mW of generated light using the
10 mm long PPLN waveguide crystal and more than 55 mW using the 40 mm long PPLN
bulk crystals could be achieved with this pump laser system. With this pump laser, the beam
quality and the output power were the limiting factors for single pass SHG. With the bulk
crystals astigmatism and beam quality were secondary effects while the raw output power
had the highest impact on the conversion efficiency. In contrast, the opto-optical conversion
efficiency with the waveguide crystals was very susceptible to astigmatism as well as to the
pump laser beam quality. With the off-axis ECDL, the generated light was tunable over a
large range with all four crystals limited by the temperature operation range of the crystals.

With a TA-ECDL in a rear Littrow setup, more than 100 mW at 488 nm could be
generated with the 40 mm long bulk PPLN crystal. The light was tunable over the same
range as with the off-axis ECDL. However, the setup exhibited a lower conversion efficiency
than the off-axis ECDL system caused by an increased bandwidth and the degradation of the
beam quality at higher injection currents. The higher SHG powers were possible because
the TA-ECDL yielded more pump power than the off-axis ECDL. Furthermore, the setup
size was significantly larger and an optical diode had to be used.

By using a DFB diode laser and the 10 mm long PPLN waveguide crystal, more than
159 mW SHG output power at a wavelength of 488 nm were generated and a very high con-
version efficiency was achieved. The SHG output power was mainly limited by the power
of the DFB diode laser. With a lens coupling system, high laser to waveguide coupling ef-
ficiencies were feasible. The blue light was only tunable over a small range because of the
limited tuning range of the pump laser diode. Although the DFB diode laser can be operated
in a larger temperature range resulting in a broader tuning range, it will not be possible to
achieve tuning ranges comparable to the ECDL systems with diffraction gratings. However,
the DFB laser has the highest potential for further integration.

Table 7.5 gives an overview of the results achieved with the 10 mm PPLN waveguide
crystal and the 40 mm long bulk PPLN crystal.

pump laser	PPLN crystal	$P_{SHG,max}$	η_{opto}	η_{norm}	tuning range
off-axis ECDL	40 mm bulk	57 mW	6.7%	2%/W·cm	≈ 2 nm
TA-ECDL	40 mm bulk	105 mW	5%	<0.9%/W·cm	≈ 2 nm
off-axis ECDL	10 mm WG	142 mW	28%	270%/W·cm^2	≈ 5 nm
DFB laser	10 mm WG	159 mW	39%	290%/W·cm^2	< 1 nm

Table 7.5: Summary of the most important SHG results. WG - waveguide.

With the off-axis external cavity designed for the stabilization of the out-of-phase super-
mode of the stripe-array, highly efficient frequency doubling could be demonstrated. The
selection of this supermode and wavelength stabilization resulted in emission with a high
quality. Despite these improvements, the off-axis ECDL could not outperform the two state

of the art diode laser systems as pump laser for SHG in all cases. However, the coupling efficiency and the SHG output power with the waveguide was only slightly lower than with the DFB diode laser. The advantage of the stripe-array compared to the DFB laser is the large tuning range. Compared to the TA-ECDL, a lower SHG output power was achieved with the bulk crystal. But the normalized conversion efficiency was higher and SHG with a channel waveguide is possible with the off-axis ECDL system. While the DFB laser showed the best results with the waveguide, it can not reach the SHG power values of the off-axis ECDL and the TA-ECDL with the bulk crystal. The TA-ECDL is not suitable for SHG with the channel waveguide because the beam shaping is challenging and the coupling losses will be very high. In conclusion the off-axis ECDL is more versatile than the two other laser systems since very good results were achieved with all types of crystals.

Chapter 8

Off-axis ECDL based biphoton source

With the frequency doubled off-axis ECDL described in section 7.2, tunable visible radiation at a wavelength of 488 nm with high spectral purity and excellent transversal beam quality could be realized. This spectral range is of high interest for spectroscopic applications in the life sciences, because of the absorption bands of the green fluorescent proteins. However, the penetration depth of organic materials is much higher for longer wavelengths. Thus, two photon absorption using light with twice the wavelength is very interesting. Because of the random photon distribution, the two photon absorption rate is several magnitudes lower than the single photon absorption rate. To provide the high intensities necessary for two photon absorption, fs-pulsed lasers are used in most cases. However, the damage threshold of the organic material is usually low and therefore photo bleaching will occur.

By using entangled or squeezed light where pairs of photons are generated in a nonlinear process, two photon absorption with several magnitudes lower intensities might be possible possible. Such photon pairs can be generated by spontaneous parametric down-conversion (SPDC) and are essential for a number of experiments in quantum optics. In this process one photon will decay into a pair of photons. These photons are highly correlated in their temporal and spatial separation and under certain circumstances such a photon pair is called a biphoton. Especially the fields of quantum cryptography [139] and quantum teleportation [140] have attracted a lot of attention, including the general media. Furthermore, biphoton sources based on parametric down-conversion have been considered for several applications like quantum correlation metrology [141] or quantum spectroscopy [142].

A common way to generate biphotons by SPDC is to use birefringent crystals like beta barium borate [143, 144], which means, that the generated correlated photons are not emitted in the same transversal mode. However, since the introduction of periodically poled materials that use the effect of QPM for efficient parametric down-conversion and the availability of such crystals as waveguides, biphoton sources that deliver high flux rates in a single transversal mode have become possible. Several biphoton devices based on periodically poled bulk [145–148] and waveguide [148–152] crystals have been reported. A comparison between bulk and waveguide is given in [148].

Because of the low losses of optical fibers, many quantum communication devices are designed at the typical telecommunication wavelengths of 1.3 μm and 1.5 μm [149–151]. In other work, shorter wavelengths around 800 nm were investigated because of the higher sensitivity of the detectors [143–148]. To realize compact biphoton sources with a high electro-optical efficiency, diode lasers were applied for the pumping of the down-conversion process [145, 146, 150]. Normalized flux rates of up to $2.9 \cdot 10^{-6}$ photon pairs/s $\cdot$ mW [148] and conversion efficiencies of up to 10^{-6} [149] could be achieved.

Recently, promising results using down-converted light for entangled two-photon absorption have been reported [153, 154]. In most entanglement or correlation experiments, type-II phase matching is used to distinguish signal and idler by the polarization state. For quantum spectroscopy of large molecules and crystals it is preferable to have signal and idler in the same state of polarization, so that type-I or even type-0 phase matching should be considered [155]. This means that typ-0 QPM can be used to access the high nonlinearity of the d_{33} coefficient instead of the smaller d_{24} for type-II phase-matching.

In this chapter, a compact all solid state biphoton source is presented. This source was explicitly designed for quantum spectroscopic applications, like two photon absorption in large fluorescence markers with an excitation wavelength of 488 nm. It is based on the frequency doubled off-axis ECDL described in chapter 7.2.

8.1 Experimental setup and results

The biphoton source described here is based on the frequency doubled off-axis ECDL described in chapter 7.2 using the 10 mm long bulk PPLN crystal for SHG. A schematic drawing is depicted in Fig 8.1. The bulk crystal was temperature stabilized near room temperature (26°C) and two crossed cylindrical lenses L1 and L2 were used to create a symmetric focus inside the bulk crystal. A spherical lens L3 was used for collimation of the blue light and the infrared emission was separated from the generated blue light light by the use of a dichroic mirror and a 2 mm thick BG 18 filter. Behind the filter the blue light was measured to be diffraction limited with $M^2 < 1.2$ for both axes and was free of astigmatism. The emission wavelength was 487.4 nm and up to 17 mW of blue light could be obtained [1].

Because of the high sensitivity of the detectors and the high efficiency of the crystal a set of various NG filters (filters 1) had to be used behind the BG 18 filter for further attenuation of the blue pump light.
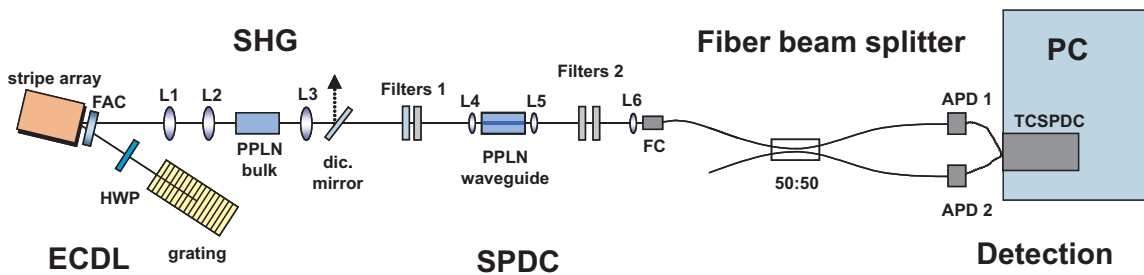
Figure 8.1: Experimental setup of the biphoton source. The frequency doubled off-axis ECDL was used to pump parametric down-conversion in the 10 mm PPLN waveguide crystal. Cylindrical lenses L1 and L2, round collimation lens L3, aspherical lenses L4, L5 and L6. Avalanche photo diodes (APD) connected to a time-correlated single-photon counting device (TCSPCD) have been used for detection.

To generate photon pairs by parametric down-conversion, the 10 mm long type-0 proton-exchanged PPLN waveguide crystal was used. The waveguide crystal was temperature stabilized around 112°C. An aspherical lens L4 with a focal length of 12 mm and

---

[1]A higher SHG output power was demonstrated in the previous chapter with the off-axis ECDL as pump source. However, not all crystals were available at the time of the experiment. The 40 mm long PPLN bulk crystal was property of *Sacher Lasertechnik*, the 10 mm waveguide PPLN crystal was used for the SPDC stage of the experiment and the 12 mm long PPKTP waveguide was not delivered, yet.

an AR coating in the visible was used for the coupling of the blue pump light into the wave-guide channel. The laser to waveguide coupling efficiency was better than 75%. A second aspherical lens L5 with a focal length of 7.5 mm and AR coating in the near infrared was used for the collimation of the down-converted light. A set of three *SCHOTT RG 850* short pass filters (filters 2) was used for blocking the blue pump light from the generated light.

The down-converted infrared light was coupled into a single mode fiber with an inte-grated 50:50 beam splitter at 980 nm (*THORLABS FC980-50B-FC*) that separates signal and idler into the two fiber branches. On the detector side two avalanche photo diodes (*PERKIN ELMER SPCM AQR-13*) with an efficiency of 15% at this wavelength and a time-correlated single photon counting device (*BECKER+HICKL*) have been used. Because of the use of a type-0 QPM crystal for parametric down-conversion, signal and idler have the same polarization.

External cavity diode laser with wavelength tunable SHG

The off-axis ECDL yielded up to 1 W of diffraction limited, tunable infrared light around a center wavelength of 976 nm. A bandwidth of 1.8 MHz and a tuning range of more than 35 nm (FWHM) could be achieved. At an injection current of 2.2 A a maximum output power of 17 mW of diffraction limited blue light was achieved. By changing the tempera-ture of the SHG crystal and simultaneously changing the ECDL emission wavelength, the blue light was tunable over several nanometers. The red curve in Fig. 8.2 shows the QPM wavelength for SHG as a function of the crystal temperature for the bulk PPLN crystal used for the generation of the blue light in the experimental setup.

To pre-estimate the optimal QPM temperature for degenerated down-conversion inside the waveguide crystal, this measurement was repeated using the waveguide crystal as SHG crystal (black curve in Fig. 8.2). The temperature coefficients for both crystals were mea-sured to be 0.04 nm/K. Because both crystals have a different poling period the absolute QPM wavelengths for efficient SHG are different at the same temperatures. The tunability of the down-converted light is discussed in more detail later in this section.
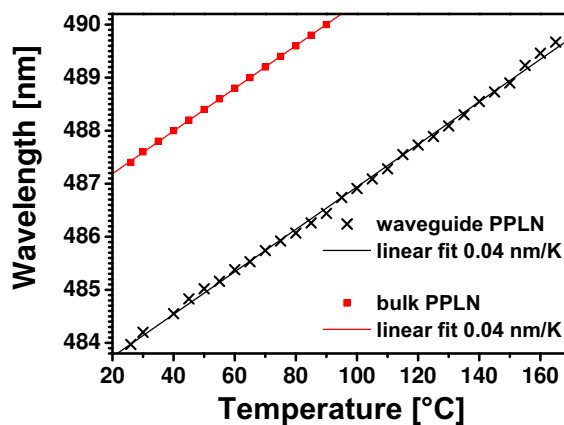
Figure 8.2: Wavelength for optimum phase-matching as a function of the crystal temperature for the 10 mm bulk PPLN crystal (squares) and the 10 mm waveguide PPLN crystal (crosses). The temperature coefficients were determined to be 0.04 nm/K for both the bulk and the waveguide material.

Photon correlation measurements

For best possible stability of the SHG process as well as the free space laser to waveguide coupling the off-axis ECDL was operated at a fixed injection current of 1.3 A. The temperatures of both crystals (T_{bulk} 26°C, $T_{waveguide} = 112$°C, $\lambda_{SHG} = 487.4$ nm) were held constant for the highest SHG conversion efficiency and the degenerated case of SPDC, respectively.
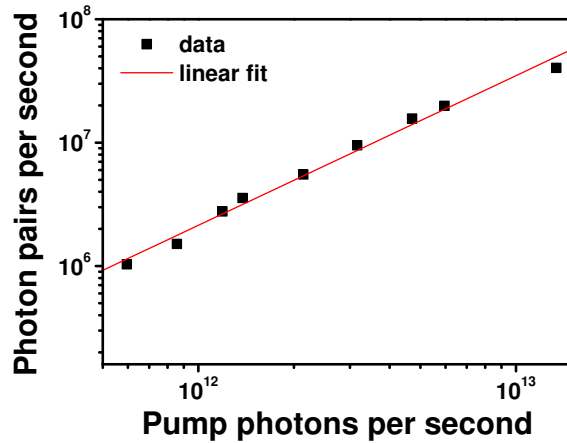
Figure 8.3: Flux-rate of the generated biphotons as a function of the incident number of photons coupled to the waveguide crystal.

In Fig. 8.3 the total number of generated photon pairs as a function of the incident pump photons is depicted. The incident number of photons has been varied by changing the transmission of the first batch of filters (filters 1 in Fig. 8.1). A flux rate of $4.0 \cdot 10^7$ generated photon pairs per second at $1.2 \cdot 10^{13}$ incident photons per second ($P = 5.4\,\mu W$) has been obtained. The highest SPDC conversion efficiency achieved was more than $8 \cdot 10^{-6}$. As expected, a linear function of the generated photons per second from the number of incident photons (or input power respectively) was observed. Because of the saturation of the detectors the maximum incident power coupled to the waveguide crystal was limited to $5.4\,\mu W$. Since the frequency doubled off-axis ECDL is capable of 3000 times higher output powers an estimated maximum number of 10^{10}–10^{11} photon pairs per second can be generated at the maximum SHG output power of the off-axis ECDL.
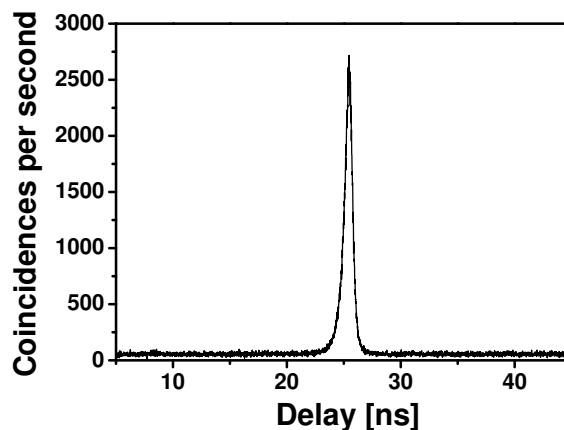
Figure 8.4: Coincidence counts measured at a blue light pump power of $2\,\mu W$ inside the waveguide crystal. The coincidence count rate was $4.5 \cdot 10^4/s$

A coincidence measurement at 2 μW pump power inside the waveguide is shown in Fig. 8.4. The measuring time was 10 s and a coincidence peak of 2690 and a coincidence count rate of $4.5 \cdot 10^4$ coincidences per second were determined. The data acquisition range was 50 ns with 4096 data points, the width of the coincidence curve was 0.769 ns (FWHM) and is limited by the electronics of the measurement system.

Spatial properties of the down-converted light

To investigate the transversal mode quality of the down-converted light an electron-multiplying CCD camera (ANDOR IXON EM+) with 512 x 512 pixels and a pixel size of 16 x 16 μm^2 was used. The generated light was collimated with the aspherical lens L5 and imaged onto the camera chip. Because of the high sensitivity of the camera, additional neutral density filters were used behind the PPLN waveguide crystal (filters 2 in Fig. 8.1).
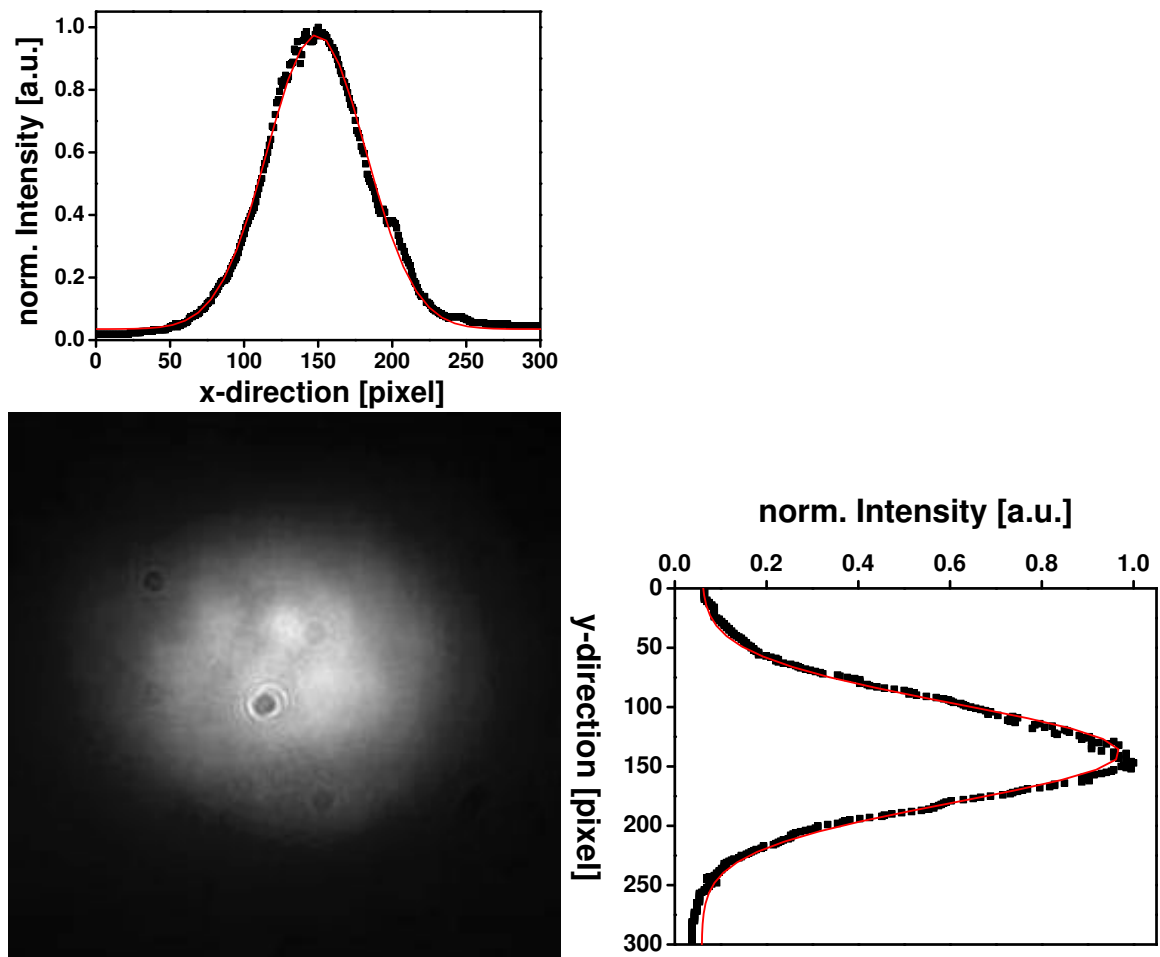
Figure 8.5: Intensity distribution of the down-converted light in front of the fiber coupler. A nearly Gaussian distribution was observed.

Fig. 8.5 shows the intensity distribution of the generated biphotons in front of the fiber coupler. The Gaussian fit through the data gives an overlap of 99.5% for the x-direction and 99.4% in y-direction. A slight ellipticity was observed which is caused by the different size of the waveguide in x- and y-direction.

Spectral investigation of the down-converted light

As stated before, the wavelength for QPM in a periodically poled material is a function of the temperature. Thus, the wavelength for QPM can be changed by adjusting the temperature of the material. Therefore the emission wavelength of the down-converted light, generated by the source is tunable in two ways: firstly the wavelength of the degenerated case is tunable, secondly the down-converted emission can be detuned from the degenerated case.

Tuning wavelength of the degenerated SPDC emission: The wavelength for the degenerated case of SPDC is tunable by tuning the emission wavelength of the frequency doubled off-axis ECDL (by changing the bulk crystal temperature and the grating angle simultaneously) and adjusting the temperature of the waveguide crystal to achieve the highest SPDC conversion efficiency.

Figure 8.6 shows the SPDC pump wavelength at maximum coincidence count rates as a function of the temperature. Two exemplarily selected SHG emission wavelengths ($\lambda_{\text{SHG1}} = 487.4$ nm, $\lambda_{\text{SHG2}} = 488.6$ nm) have been investigated. The blue crosses indicate the measured temperatures ($T_{\text{waveguide1}} = 112°C$, $T_{\text{waveguide2}} = 140°C$) of the waveguide crystal with the highest biphoton flux-rates. A third reference measurement was performed using a 488.0 nm argon ion laser ($T_{\text{waveguide3}} = 130°C$). The deviation of the determined values from the SHG QPM curve was negligible.
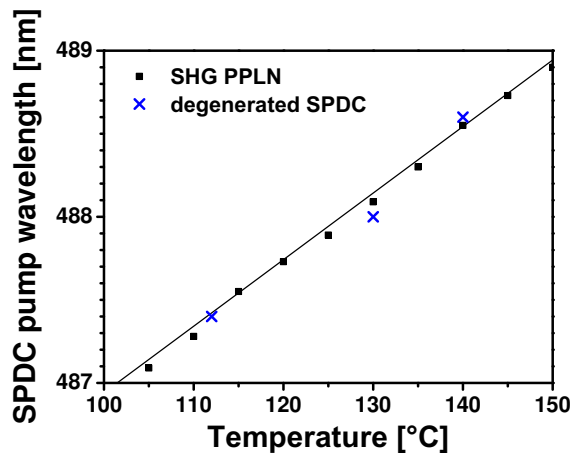
Figure 8.6: Pump wavelength for the biphoton count rate maximum as a function of the temperature of the waveguide crystal (crosses). For comparison the black curve shows the SHG wavelength of the waveguide PPLN crystal as a function of the temperature (squares).

(De-)Tuning the wavelength around the degenerated SPDC: The degenerated case is not necessarily the best for the investigation of entangled two-photon absorption. Since the ambition was to realize a biphoton source for quantum spectroscopy, the emission wavelength of the down-converted light should be tunable around degeneracy as well. This was possible when the (blue pump) wavelength emitted by the frequency doubled off-axis ECDL was fixed and the temperature of the waveguide crystal was changed, only.

For the spectral investigation of this "detuning" the fiber beam splitter (Fig. 8.1) was replaced by a single mode fiber which was attached to an OSA. Moreover, the diode injection current of the off-axis ECDL was increased to 2.2 A and the NG 4 filters have been

removed. The pump power behind the BG 18 filter was 12 mW which results in 9 mW incident into the waveguide. A coincidence measurement using a time-correlated single-photon counting device at this high output power was not possible because the avalanche photo diodes saturated. But an estimation results in a flux-rate of $6.3 \cdot 10^{10}$ photon pairs/s. While the temperature of the SHG crystal remained constant at 26°C (corresponding to λ_{SHG} = 487.4 nm), the temperature of the (SPDC) waveguide crystal was detuned from the degenerated case by a few °C.

Figure 8.7 (a-d) shows the evolution of the spectrum of the down-converted light for four different waveguide (SPDC) crystal temperatures from 114°C to 111°C while the bulk (SHG) crystal was operated at 26°C. At a temperature of 114°C (Fig. 8.7 (a)) two peaks around 975 nm are observed. One peak is located at 955 nm the other at 995 nm, each with a bandwidth of about 14 nm (FWHM). By decreasing the crystal temperature to 113°C the two peaks merge and the bandwidth is 30 nm (FWHM). For the degenerated case at 112°C shown in Fig. 8.7 (c) the bandwidth narrows to 18 nm (FWHM). By decreasing the temperature further to 111°C the spectrum broadens to 30 nm again (Fig. 8.7 (d)). By increasing the temperature to 115°C the distance between the two peaks was 55 nm centered around 975 nm. Above 115°C and below 111°C, no spectral signal could be detected out of the noise. This spectral behavior is a proof that down-conversion is present at high pump powers, as expected.

The normalized biphoton-flux rate as described in subsection 8.1 was $7 \cdot 10^{9}$ photon pairs/s·mW. Taking into account that this was measured at the degenerated case with a bandwidth of 18 nm (FWHM) this can be further normalized to $3.9 \cdot 10^{8}$ photon pairs/s·mW·nm, respectively. Another common way to characterize a light emitting source
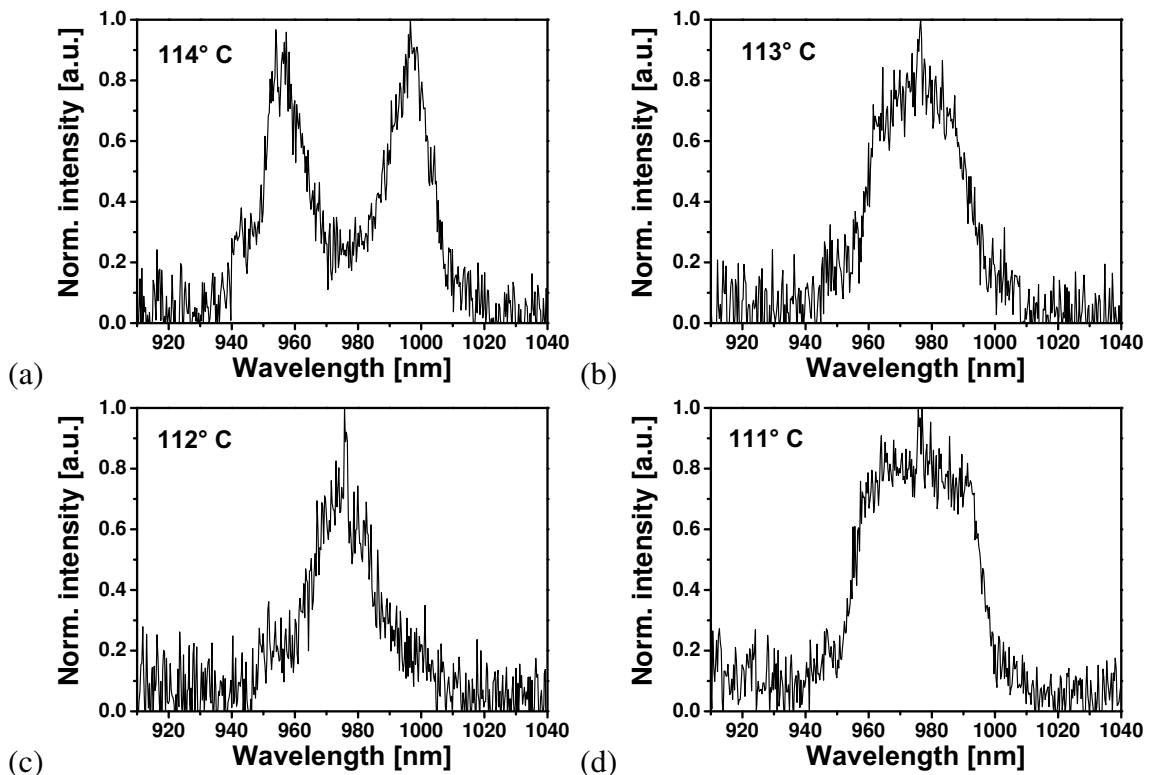
Figure 8.7: Spectra of the down-converted light coupled into a single mode fiber and measured with an optical spectrum analyzer for four different temperatures of the waveguide (SPDC) crystal. The wavelength of the pump light remained constant.

is the average number of photon pairs emitted per coherence time $\langle n \rangle = N \cdot \tau_c$, with $\tau_c = 0.44 \cdot \lambda^2 / (c \cdot \Delta\lambda)$. Considering a measured bandwidth of $\Delta\lambda = 18$ nm around a center wavelength of $\lambda = 974.8$ nm this gives a coherence time of $\tau_c = 7.76 \cdot 10^{-14}$ s. The number of generated photon pairs at 9 mW was estimated to be $6.3 \cdot 10^{10}$ photon pairs/s, which results in $\langle n \rangle = 0.0065$.

Influence of the detuning around the degenerated SPDC on the biphoton flux-rate:
The measured coincidence rate as a function of the crystal temperature is shown in Fig. 8.8 for a pump wavelength of $\lambda = 487.4$ nm. This measurement was performed under the same condition as described in subsection 8.1, at a low coupled blue power of 2 μW inside the waveguide, because at higher pump powers the detectors saturated.

The degenerated case with the highest biphoton flux rate of $4.5 \cdot 10^4$ coincidences/s was observed at a waveguide temperature of 112°C. For the broadest detected spectrum (at 115°C) the biphoton flux rate was a 4.5 times lower compared to the maximum, but still exceeded 10^4. Furthermore, even at a detuning of 5 nm from the peak emission the detected coincidence rate was measured to be above 10^3 photons per second.
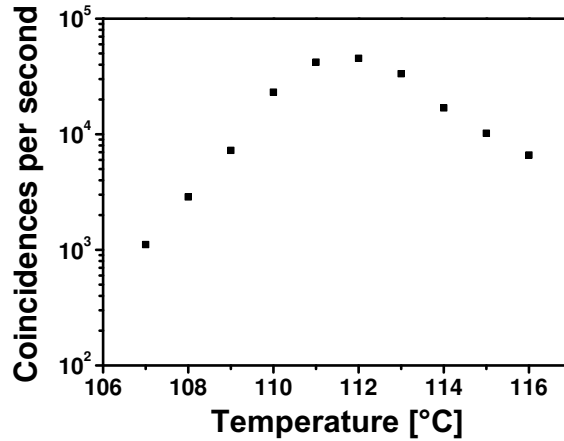
Figure 8.8: Measured coincidences per second as a function of the waveguide temperature at a coupled blue pump power of 2 μW. At a pump wavelength of 487.4 nm the degenerated case is reached at 112°C and the highest biphoton count rate of $4.5 \cdot 10^4$ coincidences/s was obtained.

8.2 Summary

A compact all solid state biphoton source based on a frequency doubled off-axis ECDL was realized. A high biphoton flux rate of more than 10^7 photon pairs per second was achieved with very low pump powers of a few μW. This was realized by coupling the blue light into the 10 mm waveguide PPLN crystal. The efficiency of the SPDC process was higher than $8 \cdot 10^{-6}$ and a linear function between input power and flux rate was observed. By assuming the process to remain linear, the maximum flux rate generated by the device is in the order of 10^{11} biphotons per second at a pump power >15 mW.

A potential application of the down-converted light at 976 nm is correlated two-photon spectroscopy of green fluorescent proteins [156]. Such an experiment was shown by Lee et al. [153]. In this experiment, a fs-laser with a duty cycle of $8.2 \cdot 10^{-5}$ was used and a flux-rate of $3 \cdot 10^5$ photon pairs/s have been sufficient to perform the entangled two-photon

absorption experiments. Considering this duty cycle, a rate of 10^{10} photon pairs/s should be high enough to realize correlated two photon absorption experiments with cw light.

Due to the tunability of the frequency doubled off-axis ECDL, the wavelength of the degenerated SPDC case could be tuned over several nanometers. Furthermore, it was possible to realize down-converted biphoton emission in the non-degenerated case by changing the waveguide crystal temperature. Detailed investigations of the spectral evolution and the influence of non-degeneration on the SPDC conversion efficiency showed promising results for the use of this device in quantum spectroscopy applications.

The non-classical light emitted by the source could be tuned regarding the center wavelength of the degenerated case and by the degree of degeneration. The correlated photons were emitted in the same transversal mode. The beam quality of the blue pump light was measured to be $M^2 < 1.1$ and the SPDC light showed a near Gaussian emission. This resulted in a high brightness of the biphoton emission. The bandwidth of the down-converted emission was measured to be 18 nm (FWHM). This is relatively narrow compared to pulsed biphoton sources as a result of the use of a narrow band cw pump laser.

Photo-refractive damage and blue induced infrared absorption were not observed during the experiments in any case. The pump power of the blue light was approximately one magnitude lower than during the SHG experiments as discussed in section 7.2.2. The generated normalized biphoton-flux rate of more than $7 \cdot 10^9$ photon pairs/s $\cdot$ mW (and $3.9 \cdot 10^8$ photon pairs/s $\cdot$ mW $\cdot$ nm, respectively) are among the highest values using diode lasers in an SPDC process in this spectral region.

Since the overall efficiency of the device was mainly limited by the efficiency of the bulk PPLN crystal used for the SHG, the use of a second waveguide crystal for the frequency doubling should improve the overall efficiency of the system by at least one order of magnitude.

However, in this experiment the frequency doubled off-axis ECDL could show its full potential. To pump SPDC in the waveguide crystal blue emission with a high wavelength stability and a large tuning range is demanded. For efficient coupling, the pump light has to be free of astigmatism with an excellent beam quality. The stripe-array yielded blue light with the required quality. The DFB laser has the advantage of very good beam quality, but has a limited tuning range. Furthermore, the best results with the DFB laser were achieved with the waveguide crystal which was used for the SPDC in this experiment. With the 10 mm bulk crystal only 4 mW of blue light could be generated. The TA-ECDL is a high power device and the coupling of the emission from this laser into a channel waveguide is very challenging. Since this is also the case for the frequency doubled radiation it can not be applied to this experiment. Thus, the external cavity enhanced stripe-array amplifier was the best choice in these circumstances.

Chapter 9

Summary and conclusion

A huge number of applications require coherent radiation in the visible spectral range. Since diode lasers are very compact and efficient light sources, there exists a great interest to cover these applications with diode laser emission. Despite modern band gap engineering not all wavelengths can be accessed with diode laser radiation, especially in the visible spectral range.

Broad area (BA) diode lasers are reliable high power light sources in the near-infrared spectrum. Frequency doubling of near-infrared radiation is a common way to generate emission in the visible spectral range, but BA lasers are not suitable as pump lasers for efficient frequency conversion because of their poor beam quality and spectral properties. For this purpose, tapered lasers and diode lasers with Bragg gratings are utilized. However, these new diode laser structures demand for additional manufacturing and assembling steps that makes their processing challenging and expensive.

An alternative to BA diode lasers is the stripe-array architecture. The emitting area of a stripe-array diode laser is comparable to a BA device and the manufacturing of these arrays requires only one additional process step. Such a stripe-array consists of several narrow striped emitters realized with close proximity. Due to the overlap of the fields of neighboring emitters or the presence of leaky waves, a strong coupling between the emitters exists. As a consequence, the emission of such an array is characterized by a so called supermode. Because of the lack of wavelength stabilization, mode competition between several supermodes can occur that leads to power fluctuations and poor beam quality.

One way to stabilize a specific supermode of an array is to operate it in an external cavity. In this work the emission properties of stripe-array amplifiers were studied theoretically and experimentally to realize a synchronization between the emitters. The aim was to achieve stable longitudinal and transversal single mode operation with high output powers giving a brightness sufficient for nonlinear frequency conversion.

Therefore it was necessary to investigate the physics that are responsible for the emission properties of the array. Based on mathematical simulations and experimental work, novel external cavity concepts have been developed to tailor the emission of such a stripe-array. The external cavity was designed to select a specific supermode and stabilize all emitters of the array at the same wavelength. This resulted in stable emission with a new level of brightness and brilliance compared to other BA and stripe-array diode laser systems and satisfied the requirements for nonlinear frequency conversion.

By using periodically poled crystals in a single pass setup it was possible to generate blue light with a very high opto-optical converzion efficiency. Furthermore, the blue light could be used to generate biphotons by parametric down-conversion.

9.1 Summary of contributions

In the first part of this thesis, the emission of a stripe-array amplifier with 40 emitters was investigated with the use of different external cavities. To predict the transversal supermode of the array that possesses the lowest threshold and highest stability, the stripe-array was simulated as a diode laser using a traveling wave model. The numerical simulations showed a strong tendency of this stripe-array to oscillate close to the out-of-phase supermode where neighboring emitters are coupled with a phase shift of π. However, due to the lack of wavelength stabilization, this supermode was not fully stable and higher order transversal modes were observed in the simulations. Thus, the free running stripe-array could not be used for the targeted applications, but the simulations were necessary for the design of an external cavity.

In chapter 4, the stripe-array amplifier and a BA amplifier were investigated at angular selective feedback by using two different resonator schemes. The resonator exploiting the spherical aberrations of a cylindrical lens as proposed by Raab et al. [64, 65] did not provide the necessary angular selectivity. A higher angular selectivity was realized with a plane mirror and asymmetric off-axis feedback. As predicted in the simulations, the stripe-array emission depended strongly on the feedback angle and operated preferably in the out-of-phase supermode. The BA amplifier did not show such a susceptibility to angular feedback and the transversal mode could not be stabilized, resulting in a poor beam quality. The investigations showed that the stripe-array could outperform the BA amplifier when stabilized with off-axis feedback. With the selection of the supermode of the stripe-array the beam quality could be improved drastically. However, the supermode could not be stabilized due to the longitudinal multi mode operation. Thus, it was necessary to use additional wavelength selective elements.

In chapter 5 two Littrow type external cavity diode lasers (ECDLs) have been investigated. First, an on-axis ECDL without angular selectivity was studied. Tunable, narrow bandwidth emission with an optical output power of up to 6.8 W was demonstrated [157]. Because of the lack of angular selectivity the beam quality was insufficient for nonlinear applications. In the next step, an off-axis ECDL was designed to select and stabilize a lateral supermode in combination with wavelength stabilization. By selecting the out-of-phase supermode, diffraction limited, narrow bandwidth of emission with an output power of 1 W could be obtained [75]. A brightness of $B = 62.5$ MW/cm^2-str, a bandwidth below 2 MHz and a tuning range of more than 30 nm were achieved. For the interpretation of the experimental results the numerical model was extended with a feedback term to model the external cavity. The calculations were in good agreement with the experimental data. Thus, in the first part of this thesis the emission of a stripe-array amplifier was improved successfully. This was feasible by extracting the physical characteristics of the array in theoretical and experimental investigations in a step wise process. As a result, the off-axis ECDL emission fulfilled the requirements necessary for nonlinear frequency conversion.

The second part of this work was dedicated to nonlinear frequency conversion. The off-axis ECDL was utilized as pump laser for single pass second harmonic generation (SHG) at a wavelength of 488 nm, as presented in chapter 7. With a 40 mm long bulk crystal, more than 50 mW blue light were generated. By using a 10 mm long periodically poled lithium niobate (PPLN) waveguide crystal more than 140 mW and an opto-optical conversion efficiency of 28% could be achieved [158]. As a benchmark for the off-axis ECDL, other state of the art high brilliance diode lasers have been used as pump lasers for SHG with the same nonlinear crystals. Although the off-axis ECDL did not outperform the two

other laser systems in all cases, it could compete under most circumstances and was the most versatile solution. However, compared to the free running chip the advantage made with the off-axis feedback was huge and completely new applications could be accessed.

Because of the improvement of the emission quality it was possible to realize a light source that can be used for experiments in quantum optics. In chapter 8, the blue light emitted by the frequency doubled off-axis ECDL was used to generate biphotons inside a 10 mm long PPLN waveguide crystal. A high biphoton flux rate of more than $7 \cdot 10^9$ photon pairs/s$\cdot$mW could be realized [159]. To my knowledge, this was the first time that a BA or stripe-array diode laser system was used as a pump laser for parametric down conversion. Here, the off-axis ECDL was the best choice as pump laser.

In conclusion the methods that have been developed in this work by experimental and theoretical investigations opened the door for the application of stripe-arrays to experiments in nonlinear optics allowing very high efficiencies. The work presented here consisted of several incremental steps that were taken logically and consecutively. The results obtained during this work were record values at the time of their publication.

9.2   Future directions

As in most experimental and scientific work, there are several parameters that can be improved in the future.

First of all, the semiconductor material and the array design can be optimized further. The vertical structure that was used here featured a waveguide with a thickness of 0.88 μm. Today, super large optical cavities are available with waveguide thicknesses of up to 8.5 μm [25].

The numerical model is a powerful tool that can be used to design an advanced stripe-array architecture. Parameters like the emitter size, the pitch between neighboring stripes and the number of individual emitters can be varied in the model. Furthermore, the off-axis ECDL was limited by thermal rollover and modeling of different feedback conditions can be performed to find the reasons for this limitation.

Concerning the frequency conversion experiments several improvements are possible. At the moment first experiments that aim at higher efficiencies by resonant SHG in an external ring resonator have been done using the off-axis stripe-array ECDL as pump laser [160]. So far, 130 mW were demonstrated by using a 10 mm long bulk PPLN in a miniaturized enhancement resonator. The SHG output powers achieved with the waveguide crystals were mainly limited by laser to waveguide coupling losses. A further improvement of the beam quality may lead to better coupling efficiencies and higher SHG output powers, but also other waveguide sizes and tapered input facets can be considered.

The electro-optical efficiency of the biphoton source was mainly limited by the conversion efficiency of the infrared light into the blue spectrum because only the 10 mm long bulk PPLN crystal was used. By using two waveguide crystals, a higher efficiency and a higher biphoton flux rate should be feasible.

List of acronyms

AlGaAs	aluminum gallium arsenide
AR	anti-reflection
BA	broad area
cw	continuous wave
DFB	distributed feedback
DBR	distributed Bragg reflector
ECDL	external cavity diode laser
FAC	fast axis collimator
FPI	Fabry Perot interferometer
FSR	free spectral range
FWHM	full with at half maximum
GaAs	gallium arsenide
HR	highly reflecting
HT	highly transmissive
InGaAs	indium gallium arsenide
KTP	potassium titanyl phosphate
LN	lithium niobate
LT	lithium tantalate
OSA	optical spectrum analyzer
PPKTP	periodically poled potassium titanyl phosphate
PPLN	periodically poled lithium niobate
PPLT	periodically poled lithium tantalate
QPM	quasi phase-matching
SAC	slow axis collimator
SHG	second harmonic generation
SPDC	spontaneous parametric down conversion
TA	tapered amplifier
TE	transverse-electric
TM	transverse-magnetic

Appendix A

Additional information

A.1 Second order susceptibility $\chi^{(2)}$

The susceptibility $\chi^{(n)}$ is a tensor of the rank (n+1). Thus, the second order susceptibility $\chi^{(2)}$ is a third rank tensor with 27 components. In the case of SHG, where two of the three participating fields are identical, the intrinsic permutation with $\chi^{(2)}_{ijk} = \chi^{(2)}_{ikj}$ can be performed. This results in the following notation:

$$
\begin{array}{ccccccc}
jk: & 11 & 22 & 33 & 23,32 & 31,13 & 12,21 \\
l: & 1 & 2 & 3 & 4 & 5 & 6
\end{array}
$$

Thus, the tensor $\chi^{(2)}_{ijk}$ can be simplified to a tensor $\mathbf{d}_{il}$ with only 18 independent components:

$$
\mathbf{d}_{il} = \varepsilon_0 \begin{pmatrix} d_{11} & d_{12} & d_{13} & d_{14} & d_{15} & d_{16} \\ d_{21} & d_{22} & d_{23} & d_{24} & d_{25} & d_{26} \\ d_{31} & d_{32} & d_{33} & d_{34} & d_{35} & d_{36} \end{pmatrix}, \tag{A.1}
$$

whereas $\chi^{(2)}_{ijk} = 2\mathbf{d}_{il}$.

Several general symmetry rules, like the Kleinman symmetry, or explicit symmetry rules for each crystal class can be used for a further simplification of this matrix. Moreover, certain tensor components vanish under specific circumstances. This is described in detail in the textbooks of Boyd [81] and Zernike [161]. Here only the two relevant tensors for the materials that have been used in this work will be given:

KTP has an orthorhombic crystal structure with the point group mm2 and its polarization for SHG reads:

$$
\begin{pmatrix} \mathbf{P}^{(2)}_x \\ \mathbf{P}^{(2)}_y \\ \mathbf{P}^{(2)}_z \end{pmatrix} = \varepsilon_0 \begin{pmatrix} 0 & 0 & 0 & 0 & d_{31} & 0 \\ 0 & 0 & 0 & d_{32} & 0 & 0 \\ d_{31} & d_{32} & d_{33} & 0 & 0 & 0 \end{pmatrix} \begin{pmatrix} \mathbf{E}^2_x \\ \mathbf{E}^2_y \\ \mathbf{E}^2_z \\ 2\mathbf{E}_y\mathbf{E}_z \\ 2\mathbf{E}_z\mathbf{E}_x \\ 2\mathbf{E}_x\mathbf{E}_y \end{pmatrix}. \tag{A.2}
$$

For a rhombohedral crystals with point group 3m (like lithium niobate) it reads:

$$
\begin{pmatrix} \mathbf{P}_x^{(2)} \\ \mathbf{P}_y^{(2)} \\ \mathbf{P}_z^{(2)} \end{pmatrix} = \varepsilon_0 \begin{pmatrix} 0 & 0 & 0 & 0 & d_{31} & -d_{22} \\ -d_{22} & d_{22} & 0 & d_{31} & 0 & 0 \\ d_{31} & d_{31} & d_{33} & 0 & 0 & 0 \end{pmatrix} \begin{pmatrix} \mathbf{E}_x^2 \\ \mathbf{E}_y^2 \\ \mathbf{E}_z^2 \\ 2\mathbf{E}_y\mathbf{E}_z \\ 2\mathbf{E}_z\mathbf{E}_x \\ 2\mathbf{E}_x\mathbf{E}_y \end{pmatrix}. \tag{A.3}
$$

Several consequences result from these matrices, like which scalar coefficient d_{eff} can be used with which participating fields. Furthermore, the possible phase-matching types are determined for a given crystal direction by this material dependent parameters.

A.2   Measurement devices

Power measurement: For power measurement in the infrared spectrum, two thermoelectric detectors from *Gentec* have been used: the PS-310 with a range from 2 mW to 3 W and a resolution of 100 μW and the PS-330 ranging from 6 mW to 40 W with a resolution of 300 μW. Both heads are specified with a rise time of 1-2 s and a precision of $\pm$ 2.5% and have been operated with the monitors Gentec Duo and Gentec TPM-300 CE.

For the low power measurements in the blue and infrared spectral range, the *Thorlabs* "Powermeter" with a silicon detector ranging from 400 nm to 1100 nm. The precision is $\pm$ 5 digits at a measuring range from 20 nW to 30 mW.

Measuring the beam propagation factor M^2**:**   The measurements of the far-field intensity distributions, the beam profiles and the caustics were performed with the linear scanning system *Beamscope-P5* from *Data Ray*. This device utilizes a "moving slit" technique that is conform with the ISO 11146 standard [17]. The moving slit is equipped with a measurement head with a detector that scans the beam profile perpendicular to the propagation direction. For our measurements, a silicon detector that is sensitive from 190 to 1150 nm was used. A single and a double slit with slit widths of 5 μm have been used. By using a double slit it is possible to measure both axes of the laser beam simultaneously. To obtain a beam caustic, the head is mounted on a precision translation stage and is moved along the propagation direction of the laser beam. To measure the beam parameter product, a focus has to be generated in the middle of the scanning path of the device. The scanning range should cover two Rayleigh length of the laser beam and a focusing lens without aberrations should be used.

Optical spectrum analyzer: The spectral measurements have been performed with the optical spectrum analyzer (OSA) AQ-6315Q manufactured by *Ando*. The aperture of the input fiber is imaged onto a detector behind a variable aperture. The OSA comprises movable gratings and the spectrum is scanned step by step. The resolution and the dynamic range depends on the scanning speed of the device. It has a measurement range from 350 nm to 1750 nm and a resolution of 50 pm. Furthermore, it is possible to perform several scans and use the internal mathematical analysis to virtually increase the dynamic range.

Fabry-Perot etalon: The free spectral range of an etalon and is given by:

$$FSR = \frac{c_0}{2 \cdot L \cdot n},$$

with the speed of ligh c the index of refraction n and the thickness of the etalon L. The finesse F depends on the reflectivities R of the surfaces and reads:

$$F = \frac{\pi \cdot \sqrt{R}}{1 - R}.$$

The resolution of the etalon is given by:

$$\Delta \nu = \frac{FSR}{F}$$

Here, an etalon made out of BK7 (n = 1.5) with a reflectivity of R = 85% and a thickness of d = 2 mm was used. The FSR was 50 GHz, the finesse F = 17.8 giving a resolution of $\Delta \nu \approx 3$ GHz. The interference pattern was imaged onto a CCD camera.

Furthermore, a scanning Fabry-Perot interferometer (*Burleigh*, FPI-SA-91) with an FSR of 8 GHz was used at *Sacher Lasertechnik* for the characterization of the off-axis ECDL and the DFB diode laser.

Bibliography

[1] T. H. Maiman, "Optical and Microwave-Optical Experiments in Ruby," Phys. Rev. Lett. **4**, 564–566 (1960).

[2] R. N. Hall, G. E. Fenner, J. D. Kingsley, T. J. Soltys, and R. O. Carlson, "Coherent Light Emission From GaAs Junctions," Phys. Rev. Lett. **9**, 366–368 (1962).

[3] M. Kanskar, T. Earles, T.J. Goodnough, E. Stiers, D. Botez, and L.J. Mawst, "73% CW power conversion efficiency at 50 W from 970 nm diode laser bars," Electron. Lett. **41**, 245 – 247 (2005).

[4] K. J. Paschke, S. Einfeldt, A. Ginolas, K. Häusler, P. Ressel, B. Sumpf, H. Wenzel, and G. Erbert, "15 - W Reliable Operation of 96 - μm Aperture Broad-Area Diode Lasers Emitting at 980 nm," in CLEO/QELS 2008 Conference Digest p. CMN4 (2008).

[5] H. Li, I. Chyr, X. Jin, F. Reinhardt, T. Towe, D. Brown, T. Nguyen, M. Berube, T. Truchan, D. Hu, R. Miller, R. Srinivasan, T. Crum, E. Wolak, R. Bullock, J. Mott, and J. Harrison, ">700W continuous-wave output power from single laser diode bar," Electron. Lett. **43**, 27–28 (2007).

[6] E. Lassila and R. Hernberg, "Bright diode laser light source," Appl. Opt. **45**, 3548–3552 (2006).

[7] C. J. Chang-Hasnain, J. Berger, D. R. Scifres, W. Streifer, J. R. Whinnery, and A. Dienes, "High power with high efficiency in a narrow single-lobed beam from a diode laser array in an external cavity," Appl.Phys. Lett. **50**, 1465–1467 (1987).

[8] S. Wolff, A. Rodionov, V. Sherstobitov, and H. Fouckhardt, "Fourier-optical transverse mode selection in external-cavity broad-area lasers: experimental and numerical results," IEEE J. Quantum Electron. **39**, 448–458 (2003).

[9] S. MacCormack and J. Feinberg, "High-brightness output from a laser-diode array coupled to a phase-conjugating mirror," Opt. Lett. **18**, 211 (1993).

[10] K. Iida, H. Horiuchi, O. Matoba, T. Omatsu, T. Shimura, and K. Kuroda, "Injection locking of a broad-area diode laser through a double phase-conjugate mirror," Opt. Commun. **146**, 6–10 (1998).

[11] L. Goldberg, D. Mehuys, and D. Hall, "3.3 W CW diffraction limited broad area semiconductor amplifier," Electron. Lett. **28**, 1082–1084 (1992).

[12] S. Masui, Y. Matsuyama, T. Yanamoto, T. Kozaki, S. Nagahama, and T. Mukai, "365 nm ultraviolet laser diodes composed of quaternary AlInGaN alloy," Jpn. J. Appl. Phys. **42**, LL1318 (2003).

[13] C. Lin, M. Grau, O. Dier, and M. C. Amann, "Low-threshold room-temperature cw operation of 2.24 - 3.04 μm GaInAsSb/AlGaAsSb quantum-well lasers," Appl. Phys. Lett. **84**, 5088 – 5090 (2004).

[14] K. Okamoto, T. Tanaka, and M. Kubota, "High-Efficiency Continuous-Wave Operation of Blue-Green Laser Diodes Based on Nonpolar m-Plane Gallium Nitride," Appl. Phys. Express **1**, 072 201 (2008).

[15] Y. Enya, Y. Yoshizumi, T. Kyono, K. Akita, M. Ueno, M. Adachi, T. Sumitomo, S. Tokuyama, T. Ikegami, K. Katayama, and T. Nakamura, "531 nm Green Lasing of InGaN Based Laser Diodes on Semi-Polar $\{20\bar{2}1\}$ Free-Standing GaN Substrates," Appl. Phys. Express **2**, 082 101 (2009).

[16] W. P. Risk, T. R. Gosnell, and A. V. Nurmikko, *Compact Blue-Green Lasers* (Cambridge Univ. Press, Cambridge, 2003).

[17] International Organization for Standardization, "Lasers and laser-related equipment - Test methods for laser beam parameters - Beam widths, divergence angle and beam propagation factor," ISO 11146 (2004).

[18] R. Diehl, ed., *High-power diode lasers - Fundamentals, technology, applications (Topics in applied physics, 78)* (Springer, Berlin, 2000).

[19] T. Numai, ed., *Fundamentals of Semiconductor Lasers (Springer series in optical sciences, 93)* (Springer, New York, 2004).

[20] G. Chen and C. L. Tien, "Facet heating of quantum well lasers," J. of Appl. Phys. **74**, 2167–2174 (1993).

[21] M. Ziegler, V. Talalaev, J. W. Tomm, T. Elsaesser, P. Ressel, B. Sumpf, and G. Erbert, "Surface recombination and facet heating in high-power diode lasers," Appl. Phys. Lett. **92**, 203 506 (2008).

[22] M. Mikulla, P. Chazan, A. Schmitt, S. Morgott, A. Wetzel, M. Walther, R. Kiefer, W. Pletschen, J. Braunstein, and G. Weimann, "High-brightness tapered semiconductor laser oscillators and amplifiers with low-modal gain epilayer-structures," IEEE Photon. Techn. Lett. **10**, 654–656 (1998).

[23] A. Knauer, G. Erbert, R. Staske, B. Sumpf, H. Wenzel, and M. Weyers, "High-power 808 - nm lasers with a super-large optical cavity," Semicond. Sci. Technol. **20**, 621 – 624 (2005).

[24] J. Lee, L. Mawst, and D. Botez, "Improved-performance, InGaAs/InGaAsP ($\lambda = 980$ nm) asymmetric broad-waveguide diode lasers via waveguide-core doping," Electron. Lett. **39**, 1250 – 1252 (2003).

[25] A. Pietrzak, H. Wenzel, G. Erbert, and G. Tränkle, "High-power laser diodes emitting light above 1100 nm with a small vertical divergence angle of 13°," Opt. Lett. **33**, 2188–2190 (2008).

[26] H. Wenzel, F. Bugge, M. Dallmer, F. Dittmar, J. Fricke, K.H. Hasler, and G. Erbert, "Fundamental-Lateral Mode Stabilized High-Power Ridge-Waveguide Lasers With a Low Beam Divergence," IEEE Photon. Techn. Lett. **20**, 214 − 216 (2008).

[27] M. Chi, B. Thestrup, and P. M. Petersen, "Self-injection locking of an extraordinarily wide broad-area diode laser with a 1000 - μm-wide emitter," Opt. Lett. **30**, 1147 − 1149 (2005).

[28] O. Hess, S. W. Koch, and J. V. Moloney, "Filamentation and Beam Propagation in Broad-Area Semiconductor Lasers," IEEE J. Quantum Electron. **31**, 35 − 43 (1995).

[29] I. Fischer, O. Hess, and W. Elsäßer and E. Gobel, "Complex Spatio-Temporal Dynamics in the Nearfield of a Broad-Area Semiconductor Laser," Europhys. Lett. **35**, 579 − 584 (1996).

[30] G. Bendeli, K. Komori, S. Arai, and Y. Suematsu, "A new structure for high-power TW-SLA," IEEE Photon. Tech. Lett. **3**, 42 − 44 (1991).

[31] J.N. Walpole, E. S. Kintzer, S.R. Chinn, C.A. Wang, and L.J. Missaggia, "High-power strained-layer InGaAs / AlGaAs tapered traveling wave amplifier," Appl. Phys. Lett. **61**, 740 − 742 (1992).

[32] M. Kelemen, J. Weber, G. Kaufel, G. Bihlmann, R. Moritz, M. Mikulla, and G. Weimann, "Tapered diode lasers at 976 nm with 8 W nearly diffraction limited output power," Electron. Lett. **41**, 1011 − 1013 (2005).

[33] C. Henry, "Theory of the linewidth of semiconductor lasers," IEEE J. Quantum Electron. **18**, 259–264 (1982).

[34] L. Ricci, M. Weidemuller, T. Esslinger, A. Hemmerich, C. Zimmermann, V. Vuletic, K. Konig, and T. Hansch, "A compact grating-stabilized diode laser system for atomic phyics," Opt. Commun. **117**, 541 − 549 (1995).

[35] C. J. Hawthorn, K. P. Weber, and R. E. Scholten, "Littrow configuration tunable external cavity diode laser with fixed direction output beam," Rev. Sci. Instrum. **72**, 4477 − 4479 (2001).

[36] A. Takamizawa, G. Yonozawa, H. Kosaka, and K. Edamatsu, "Littrow-type external-cavity diode laser with a triangular prism for suppression of the lateral shift of output beam," Rev. Sci. Instrum. **77**, 46 102 (2006).

[37] M. G. Littman and H. J. Metcalf, "Spectrally narrow pulsed dye laser without beam expander," Appl. Opt. **17**, 2224 − 2227 (1978).

[38] K. Liu and M. G. Littman, "Novel geometry for single-mode scanning of tunable lasers," Opt. Lett. **6**, 117 − 118 (1981).

[39] H. Kogelnik and C. V. Shank, "Coupled-wave theory of distributed feedback lasers," J. Appl. Phys. **43**, 2327 (1972).

[40] L. J. Mawst, H. Yang, M. Nesnidal, A. Al-Muhanna, D. Botez, T. A. Vang, F. D. Alvarez, and R. Johnson, "High-Power, Single-Mode, Al-Free InGaAs(P)/InGaP/GaAs Distributed Feedback Diode Lasers," J. Cryst. Growth **195**, 609 − 616 (1998).

[41] H. Wenzel, J. Fricke, A. Klehr, A. Knauer, and G. Erbert, "High-power 980 nm DFB RW lasers with a narrow vertical far field," Photon. Technol. Lett. **18**, 737 – 739 (2006).

[42] A. Schmitt, M. Mikulla, P. Chazan, M. Walther, R. Kiefer, J. Braunstein, and G. Weimann, "80 μm Wide InAIGaAs laser diodes with 44% wallplug efficiency at 7 W cw output power," CLEO/Europe **CThG3**, 268–268 (1998).

[43] N. W. Carlson, *Monolithic diode-laser arrays (Springer series in electronics and photonics, 33)* (Springer, Berlin, 1994).

[44] D. Botez and D. R. Scifres, eds., *Diode laser arrays* (Cambridge, Cambridge, 1994).

[45] K. Boucke, *Phasengekoppelte Arrays für Hochleistungsdiodenlaser mit hoher Strahlqualität* (PhD thesis, RWTH Aachen, 2000).

[46] K. Ebeling, ed., *Integrated optoelectronics* (Springer, Berlin, 1997).

[47] D. Botez, "Array-mode far-field patterns for phase-locked diode-laser array: Coupled-mode theory versus simple diffraction theory," IEEE J. Quantum Electron. **21**, 1752–1755 (1985).

[48] J. K. Butler, D. E. Ackley, and D. Botez, "Coupled-mode analysis of phase-locked injection laser arrays," Appl. Phys. Letters **44**, 293–295 (1984).

[49] M. Spreemann, M. Lichtner, M. Radziunas, U. Bandelow, and H. Wenzel, "Measurement and Simulation of Distributed-Feedback Tapered Master-Oscillator Power Amplifiers," IEEE J. Quantum Electron. **45**, 609–616 (2009).

[50] O. Hess and E. Schöll, "Spatio-temporal dynamics in twin-stripe semiconductor lasers," Phys. D **70**, 165–177 (1994).

[51] S. Balsamo, F. Sartori, and I. Montrosset, "Dynamic beam propagation method for flared semiconductor power amplifiers," IEEE J. Sel. Top. Quantum Electron. **2**, 378–384 (1996).

[52] U. Bendelow, M. Radziunas, J. Sieber, and M. Wolfrum, "Impact of gain dispersion on the spatio-temporal dynamics of multisection lasers," IEEE J. Quantum Electron. **37**, 183–188 (2001).

[53] H.-J. Wunsche, M. Radziunas, S. Bauer, O. Brox, and B. Sartorius, "Modeling of mode control and noise in self-pulsating PhaseCOMB lasers," IEEE J. Sel. Top. Quantum Electron. **9**, 857–864 (2003).

[54] M. Lichtner, M. Radziunas, and L. Recke, "Well-posedness, smooth dependence and centre manifold reduction for a semilinear hyperbolic system from laser dynamics," Math. Methods Appl. Sci. **30**, 857–864 (2007).

[55] M. Lichtner and M. Spreemann, "Parallel simulation of high power semiconductor lasers," Springer Lecture Notes in Computer Science (LNCS) **accepted** (2009).

[56] N. Stelmakh, "Harnessing Multimode Broad-Area Laser-Diode Emission Into a Single-Lobe Diffraction- Limited Spot," IEEE Photon. Tech. Lett. **19**, 1392–1394 (2007).

[57] F. Wang, A. Hermerschmidt, and H. J. Eichler, "High-power narrowed-bandwidth output of a broad-area multiple-stripe diode laser with photorefractive phase-conjugated injection," Opt. Commun. **209**, 391–395 (2002).

[58] L. Goldberg and J. Weller, "Narrow lobe emission of high power broad stripe laser in external resonator cavity," Electron. Lett. **25**, 112–114 (1989).

[59] L. Meng, P. Roos, and J. Carlsten, "High-efficiency continuous-wave Raman laser pumped by an injection-locked broad-area diode laser," IEEE J. Quantum Electron. **40**, 390–393 (2004).

[60] G. Abbas, S. Yang, V. Chan, and J. Fujimoto, "Injection behavior and modeling of 100 mW broad area diode lasers," IEEE J. Quantum Electron. **24**, 609–617 (1988).

[61] M. Chi, N.-S. Bøgh, B. Thestrup, and P. M. Petersen, "Improvement of the beam quality of a broad-area diode laser using double feedback from two external mirrors," Appl. Phys. Letters **85**, 1107–1109 (2004).

[62] B. Thestrup, M. Chi, B. Sass, and P. M. Petersen, "High brightness laser source based on polarization coupling of two diode lasers with asymmetric feedback," Appl. Phys. Lett. **82**(5), 680–682 (2003).

[63] R. Pillai and E. Garmire, "Paraxial-misalignment insensitive external-cavity semiconductor-laser array emitting near-diffraction limited single-lobed beam," IEEE J. Quantum Electron. **32**, 996–1008 (1996).

[64] V. Raab, D. Skoczowsky, and R. Menzel, "Tuning high-power laser diodes with as much as 0.38 W of power and $M^2 = 1.2$ over a range of 32 nm with 3-GHz bandwidth," Opt. Lett. **27**, 1995–1997 (2002).

[65] V. Raab and R. Menzel, "External resonator design for high-power laser diodes that yields 400mW of TEM_{00} power," Opt. Lett. **27**, 167–169 (2002).

[66] E. Samsøe, P. Andersen, S. Andersson-Engels, and P. Petersen, "Improvement of spatial and temporal coherence of a broad area laser diode using an external-cavity design with double grating feedback," Opt. Express **12**, 609–616 (2004).

[67] J. Chen, X. Wu, J. Ge, A. Hermerschmidt, and H. J. Eichler, Appl. Phys. Lett. **85**, 525–527 (2004).

[68] L. Lang, J. J. Lim, S. Sujecki, and E. C. Larkins, "Improvement of the beam quality of a broad-area diode laser using asymmetric feedback from an external cavity," Opt. Quantum Electron. (2009).

[69] R. Menzel, *Photonics, 2nd Edition* (Springer, Berlin, 2007).

[70] E. Ullner, *Kohärente Kopplung von Breitstreifen-Diodenlasern durch spezielle externe Resonatorkonzepte zur Erhöhung der Strahldichte* (Diploma thesis, University of Potsdam, 2000).

[71] A. Gourevitch, G. Venus, V. Smirnov, and L. Glebov, "Efficient pumping of Rb vapor by high-power volume Bragg diode laser," Opt. Lett. **32**, 2611–2613 (2007).

[72] F. Wang, A. Hermerschmidt, and H. J. Eichler, "Narrow-bandwidth high-power out-put of a laser diode array with a simple external cavity," Opt. Commun. **218**, 135 – 139 (2003).

[73] A. Gourevitch, G. Venus, V. Smirnov, D. A. Hostutler, and L. Glebov, "Continuous wave, 30 W laser-diode bar with 10 GHz linewidth for Rb laser pumping," Opt. Lett. **33**, 702–704 (2008).

[74] B. Liu, Y. Liu, and Y. Braiman, "Linewidth reduction of a broad-area laser diode array in a compound external cavity," Appl. Opt. **48**, 365–370 (2009).

[75] A. Jechow, V. Raab, R. Menzel, M. Cenkier, S. Stry, and J. Sacher, "1 W tunable near diffraction limited light from a broad area diode in an external cavity with a line width of 1.7 MHz," Opt. Commun. **277**, 161 – 165 (2007).

[76] G. R. Hadley, A. Owyoung, and J. P. Hohimer, "Modeling of injection-locking phe-nomena in diode-laser arrays," Opt. Lett. **11**, 144.

[77] J. E. Epler, J. N. Holonyak, R. D. Burnham, T. L. Paoli, R. L. Thornton, and M. M. Blouke, "Transverse modes of gain-guided coupled-stripe lasers: External cavity control of the emitter spacing," Appl. Phys. Letters **47**, 7–9 (1985).

[78] E. Samsøe, P. M. Petersen, S. Andersson-Engels, and P. E. Andersen, "Second-harmonic generation of 405-nm light using periodically poled $KTiOPO_4$ pumped by external-cavity laser diode with double grating feedback," Appl. Phys. B **80**, 861–864 (2005).

[79] M. Lobel, P. M. Petersen, and P. M. Johansen, "Tunable single-mode operation of a high-power laser-diode array by use of an external cavity with a grating and a photorefractive phase-conjugate mirror," J. Opt. Soc. Am. B **15**, 2000–2005 (1998).

[80] P. A. Franken, A. E. Hill, and C. W. Peters and G. Weinreich, "Generation of Optical Harmonics," Phys. Rev. Lett. **7**, 118 – 119 (1961).

[81] R. W. Boyd, *Nonlinear Optics, third edition* (Academic press, San Diego, 2008).

[82] J. A. Giordmaine, "Mixing of light beams in crystals," Phys. Rev. Lett. **8**, 19 – 20 (1962).

[83] J. A. Armstrong, N. Bloembergen, J. Ducuing, and P. S. Pershan, "Interactions be-tween light waves in a nonlinear dielectric," Phys. Rev. **127**, 1918 – 1939 (1962).

[84] M. M. Fejer, G. A. Magel, D. H. Jundt, and R. L. Byer, "Quasi-Phase-Matched Second Harmonic Generation: Tuning and Tolerances," IEEE J. Quantum. Electron. **28**, 2631 – 2654 (1992).

[85] D. S. Hum and M. M. Fejer, "Quasi-phasematching," C. R. Physique **8**, 180 – 198 (2007).

[86] N. Bloembergen and A. J. Sievers, "Nonlinear optical properties of periodic laminar structures," Appl. Phys. Lett. **17**, 483–485 (1970).

[87] Duan Feng, Nai-Ben Ming, Jing-Fen Hong, Yong-Shun Yang, Jin-Song Zhu, Zhen Yang, and Ye-Ning Wang, "Enhancement of second-harmonic generation in LiNbO$_3$ crystals with periodic laminar ferroelectric domains," Appl. Phys. Lett. **37**, 607 – 609 (1980).

[88] E. J. Lim, M. M. Fejer, and R. L. Byer, "Second-harmonic generation of green light in periodically poled planar lithium niobate waveguide," Electron. Lett. **25**, 174 – 175 (1989).

[89] M. Yamada, N. Nada, M. Saitoh, and K. Watanabe, "First-order quasi-phase matched LiNbO$_3$ waveguide periodically poled by applying an external field for efficient blue second-harmonic generation," Appl. Phys. Lett. **62**, 435 – 436 (1993).

[90] I. Shoji, T. Kondo, and R. Ito, "Second-order nonlinear susceptibilities of various dielectric and semiconductor materials," Opt. Quantum Electron. **34**, 797 – 833 (2002).

[91] S. Haidar, K. Miyamoto, and H. Ito, "Generation of tunable mid-IR (5.5-9.3 μm) from a 2-μm pumped ZnGeP2 optical parametric oscillator," Opt. Commun. **241**, 173 – 178 (2004).

[92] Y. L. Chen, W. G. Yan, J. Guo, S. L. Chen, and G. Y. Zhang, "Effect of Mg concentration on the domain reversal of Mg-doped LiNbO$_3$," Appl. Phys. Lett. **87**, 212 904 (2005).

[93] Y. Petit, B. Boulanger, P. Segonds, and T. Taira, "Angular quasi-phase-matching," Phys. Rev. A **76**, 063 817 (2007).

[94] K. Mizuuchi, T. Sugita, K. Yamamoto, T. Kawaguchi, T. Yoshino, and M. Imaeda, "Efficient 340-nm light generation by a ridge-type waveguide in a first-order periodically poled MgO:LiNbO$_3$," Opt. Lett. **28**, 1344 – 1346 (2003).

[95] F. Juvalta, M. Jazbinsek, P. Günter, and K. Kitamura, "Electro-optical properties of near-stoichiometric and congruent lithium tantalate at ultraviolet wavelengths," J. Opt. Soc. Am. B **23**, 276 – 281 (2006).

[96] J.-P. Meyn and M. M. Fejer, "Tunable ultraviolet radiation by second-harmonic generation in periodically poled lithium tantalate," Opt. Lett. **22**, 1214 – 1216 (1997).

[97] J.-P. Meyn, C. Laue, R. Knappe, R. Wallenstein, and M. M. Fejer, "Fabrication of periodically poled lithium tantalate for UV generation with diode lasers," Appl. Phys. B **73**, 111 – 114 (2001).

[98] K. Kitamura, Y. Furukawa, K. Niwa, V. Gopalan, and T. E. Mitchell, "Crystal growth and low coercive field 180 degrees domain switching characteristics of stoichiometric LiTaO$_3$," Appl. Phys. Lett. **71**, 3073 – 3075 (1998).

[99] H. Ishizuki and T. Taira, "Mg-doped congruent LiTaO3 crystal for large-aperture quasi-phase matching device," Opt. Express **16**(21), 16 963–16 970 (2008).

[100] A. J. Tracy, C. Lopez, A. Hankla, D. J. Bamford, D. J. Cook, and S. J. Sharpe, "Generation of high-average-power visible light in periodically poled nearly stoichiometric lithium tantalate," Appl. Opt. **48**(5), 964–968 (2009).

[101] G. Hansson, H. Karlsson, S. Wang, and F. Laurell, "Transmission Measurements in KTP and Isomorphic Compounds," Appl. Opt. **39**, 5058 – 5069 (2000).

[102] H. Vanherzeele and J. D. Bierlein, "Magnitude of the nonlinear-optical coefficients of KTiOPO$_4$," Opt. Lett. **17**, 982 – 984 (1992).

[103] J. Liu, C. Wang, C. Q. Wang, X. Meng, H. Zhang, L. Zhu, J. Wang, Z. Shao, and M. Jiang, "Diode end-pumped Q-switched high-power intracavity frequency-doubled Nd:GdVO$_4$ KTP green laser," Appl. Phys. B **72**, 171 – 174 (2001).

[104] J. D. Bierlein and H. Vanherzeele, "Potassium titanyl phosphate: properties and new applications," J. Opt. Soc. Am. B **6**, 622–633 (1989).

[105] F. J. Kontur, I. Dajani, Y. Lu, and R. J. Knize, "Frequency-doubling of a CW fiber laser using PPKTP, PPMgSLT, and PPMgLN," Opt. Express **15**, 12 882 – 12 889 (2007).

[106] X. Mu and Y. J. Ding, "Investigation of damage mechanisms of KTiOPO$_4$ crystals by use of a continuous-wave argon laser," Appl. Opt. **39**, 3099 – 3103 (2000).

[107] J. L. Jackel, C. E. Rice, and J. J. Veselka, "Proton exchange for high index waveguides in LiNbO$_3$," Appl. Phys. Lett. **41**, 607 – 608 (1982).

[108] W. B. Spillman, Jr., N. A. Sanford, and R. A. Soref, "Optical waveguides in LiTaO$_3$ formed by proton exchange," Opt. Lett. **8**, 497 – 498 (1983).

[109] Y. N. Korkishko, V. A. Fedorov, T. M. Morozova, F. Caccavale, F. Gonella, and F. Segato, "Reverse proton exchange for buried waveguides in LiNbO$_3$," J. Opt. Soc. Am. A **15**, 1838 – 1842 (1998).

[110] J. D. Bierlein, A. Ferretti, L. H. Brixner, and W. Y. Hsu, "Fabrication and characterization of optical waveguides in KTiOPO$_4$," Appl. Phys. Lett. **50**, 1216 (1987).

[111] M. B. Oron, D. Eger, M. Katz, A. Bruner, A. Englander, Y. Tzuk, and R. Lavi, "Frequency conversion efficiency limitation in periodically poled KTP crystals and waveguides," Proc. SPIE **3936**, 186 (2000).

[112] S. W. Kwon, W. S. Yang, H. M. Lee, W. K. Kim, H.-Y. Lee, W. J. Jeong, M. K. Song, and D. H. Yoon, "The ridge waveguide fabrication with periodically poled MgO-doped lithium niobate for green laser," Appl. Surf. Science **254**, 1101 – 1104 (2007).

[113] M. Iwai, T. Yoshino, S. Yamaguchi, M. Imaeda, N. Pavel, I. Shoji, and T. Taira, "High-power blue generation from a periodically poled MgO:LiNbO$_3$ ridge-type waveguide by frequency-doubling of a diode end-pumped Nd:Y$_3$Al$_5$O$_{12}$ laser," Appl. Phys. Lett. **83**, 3659 – 3661 (2003).

[114] S. Kurimura, Y. Kato, M. Maruyama, Y. Usui, and H. Nakajima, "Quasi-phase-matched adhered ridge waveguide in LiNbO$_3$," Appl. Phys. Lett. **89**, 123 (2006).

[115] A. M. Glass, "The photorefractive effect," Opt. Eng. **17**, 470 – 479 (1978).

[116] F. Laurell and G. Arvidsson, "Frequency doubling in Ti:MgO:LiNbO3 channel waveguides," J. Opt. Soc. Am. B **5**, 292–299 (1988).

[117] Y. Furukawa, K. Kitamura, S. Takekawa, A. Miyamoto, M. Terao, and N. Suda, "Photorefraction in LiNbO$_3$ as a function of [Li]/[Nb] and MgO concentrations," Appl. Phys. Lett. **77**, 2494 – 2496 (2000).

[118] M. Asobe, O. Tadanaga, T. Yanagawa, H. Itoh, and H. Suzuki, "Reducing photorefractive effect in periodically poled ZnO- and MgO-doped LiNbO$_3$ wavelength converters," Appl. Phys. Lett. **78**, 3163 (2001).

[119] Y. Furukawa, K. Kitamura, A. Alexandrovski, R. K. Route, M. M. Fejer, and G. Foulon, "Green-induced infrared absorption in MgO doped LiNbO$_3$," Appl. Phys. Lett. **78**, 1970 – 1972 (2001).

[120] H. Mabuchi, E. S. Polzik, and H. J. Kimble, "Blue-light-induced infrared absorption in KNbO$_3$," J. Opt. Soc. Am. B **11**, 2023 – 2029 (1994).

[121] G. D. Boyd and D. A. Kleinman, "Parametric Interaction of Focused Gaussian Light Beams," J. Appl. Phys. **39**, 3597 (1968).

[122] G. Blume, M. Uebernickel, C. Fiebig, K. Paschke, A. Ginolas, B. Eppich, R. Güther, and G. Erbert, "Rayleigh length dependent SHG conversion at 488nm using a monolithic DBR tapered diode laser," Proc. SPIE **6875**, 68 751C (2008).

[123] R. Güther, G. Blume, M. Uebernickel, C. Fiebig, K. Paschke, A. Ginolas, B. Eppich, and G. Erbert, "Generation of second harmonic with non-diffraction limited radiation," Proc. DGaO **109**, 45 (2008).

[124] G. D. Miller, R. G. Batchko, W. M. Tulloch, D. R. Weise, M. M. Fejer, and R. L. Byer, "42%-efficient single-pass cw second-harmonic generation in periodically poled lithium niobate," Opt. Lett. **22**, 1834 – 1836 (1997).

[125] J. L. Chilla, S. D. Butterworth, A. Zeitschel, J. P. Charles, A. L. Caprara, M. K. Reed, and L. Spinelli, "High power optically pumped semiconductor lasers," Proc. SPIE **5332**, 143 – 150 (2004).

[126] G. K. Samanta, S. C. Kumar, M. Mathew, C. Canalias, V. Pasiskevicius, F. Laurell, and M. Ebrahim-Zadeh, "High-power, continuous-wave, second-harmonic generation at 532 nm in periodically poled KTiOPO$_4$," Opt. Lett. **33**, 2955 – 2957 (2008).

[127] H. D. Edmonds and A. W. Smith, "Second-harmonic generation with the GaAs laser," IEEE J. Quant. Electron. **6**, 356 (1970).

[128] D. E. Zelmon, D. L. Small, and D. Jundt, "Infrared corrected Sellmeier coefficients for congruently grown lithium niobate and 5 mol.% magnesium oxide –doped lithium niobate," J. Opt. Soc. Am. B **14**, 3319–3322 (1997).

[129] A. Jechow, D. Skoczowsky, and R. Menzel, "100 mW high efficient single pass SHG at 488 nm of a single broad area laser diode with external cavity using a PPLN waveguide crystal," Opt. Express **15**, 6976 – 6981 (2007).

[130] K. Paschke, B. Sumpf, F. Dittmar, G. Erbert, R. Staske, H. Wenzel, and G. Tränkle, "Nearly diffraction limited 980 - nm tapered diode lasers with an output power of 7.7 W," IEEE J. Sel. Top. Quantum Electron. **11**, 1223 – 1227 (2005).

[131] C. Fiebig, G. Blume, C. Kaspari, D. Feise, J. Fricke, M. Matalla, W. John, H. Wenzel, K. Paschke, and G. Erbert, "12 W high-brightness single-frequency DBR tapered diode laser," Electron. Lett. **44**, 1253 – 1255 (2008).

[132] K. Paschke, C. Dzionk, J. Fricke, A. Ginolas, A. Knauer, M. Maiwald, P. Ressel, S. Schwertfeger, and G. Erbert, "High-power hybrid integrated master-oscillator power-amplifier on micro-optical bench at 980-nm," CLEO/Europe and IQEC 2007 Conference Digest p. CB33 (2007).

[133] P. Friedmann, J. Gilly, S. Moritz, R. Ostendorf, and M. T. Kelemen, "5 W frequency stabilized 976 nm tapered diode lasers," Proc. SPIE **6876**, 68 761J (2008).

[134] M. Chi, O. B. Jensen, J. Holm, C. Pedersen, P. E. Andersen, G. Erbert, B. Sumpf, and P. M. Petersen, "Tunable high-power narrow-linewidth semiconductor laser based on an external-cavity tapered amplifier," Opt. Express **13**, 10 589 – 10 596 (2005).

[135] M. Maiwald, S. Schwertfeger, R. Güther, B. Sumpf, K. Paschke, C. Dzionk, G. Erbert, and G. Tränkle, "600 mW optical output power at 488 nm by use of a high-power hybrid laser diode system and a periodically poled $MgO:LiNbO_3$ bulk crystal," Opt. Lett. **31**, 802 – 804 (2006).

[136] O. B. Jensen, P. E. Andersen, B. Sumpf, K.-H. Hasler, G. Erbert, and P. M. Petersen, "1.5 W green light generation by single-pass second harmonic generation of a single-frequency tapered diode laser," Opt. Express **17**, 6532–6539 (2009).

[137] M. Maiwald, D. Jedrzejczyk, A. Sahm, K. Paschke, R. Güther, B. Sumpf, G. Erbert, and G. Tränkle, "Second-harmonic-generation microsystem light source at 488 nm for Raman spectroscopy," Opt. Lett. **34**, 217 – 219 (2009).

[138] J. Wiedmann, O. Brox, T. Tekin, F. Scholz, T. Büttner, S. Marx, G. Lang, H. Schröder, A. Klehr, and G. Erbert, "Compact green laser source using butt-coupling between multi-section DFB-laser and SHG waveguide crystal," Electron. Lett. **44**, 1463 – 1464 (2008).

[139] N. Gisin, G. Ribordy, W. Tittel, and H. Zbinden, "Quantum cryptography," Rev. Mod. Phys. **74**, 145 – 195 (2002).

[140] D. Bouwmeester, J. W. Pan, K. Mattle, M. Eibl, H. Weinfurter, and A. Zeilinger, "Experimental quantum teleportation," Nature (London) **390**, 575 – 579 (1997).

[141] A. Migdall, "Correlated-photon metrology without absolute standards," Phys. Today **52**, 41 – 46 (1999).

[142] A. Yabushita and T. Kobayashi, "Spectroscopy by frequency entangled photon pairs," Phys. Rev. A **69**, 0138 061 – 0138 064 (2004).

[143] P. Trojek, C. Schmid, M. Bourennane, H. Weinfurter, and C. Kurtsiefer, "Compact source of polarization-entangled photon pairs," Opt. Express **12**, 276 – 281 (2004).

[144] J. Volz, C. Kurtsiefer, and H. Weinfurter, "Compact all-solid-state source of polarization-entangled photon pairs," Appl. Phys. Lett. **79**, 869 – 871 (2001).

[145] C. E. Kuklewicz, M. Fiorentino, G. Messin, F. N. C. Wong, and J. H. Shapiro, "High-flux source of polarization-entangled photons from a periodically poled KTiOPO$_4$ parametric down-converter," Phys. Rev. A **69**, 013 807 (2004).

[146] B. S. Shi, G. C. G. C. Zhai and, Y. K. Jiang, and A. Tomita, "Efficient generation of a photon pair in a bulk periodically poled potassium titanyl phosphate," Opt. Commun. **278**, 363 – 367 (2007).

[147] M. Fiorentino, S. M. Spillane, R. G. Beausoleil, T. D. Roberts, P. Battle, and M. W. Munro, "Spontaneous parametric down-conversion in periodically poled KTP waveguides and bulk crystals," Opt. Express **15**, 7479 – 7488 (2007).

[148] A. Fedrizzi, T. Herbst, A. Poppe, T. Jennewein, and A. Zeilinger, "A wavelength-tunable fiber-coupled source of narrowband entangled photons," Opt. Express **15**, 15 377 – 15 386 (2007).

[149] S. Tanzilli, H. Reidmatten, W. Tittle, H. Zbinden, P. Baldi, M. D. Micheli, D. B. Ostrowsky, and N. Gisin, "PPLN waveguide for quantum communication," Eur. Phys. J. D **18**, 155 – 160 (2002).

[150] T. Honjo, H. Takesue, and K. Inoue, "Generation of energy-time entangled photon pairs in 1.5 - μm band with periodically poled lithium niobate waveguide," Opt. Express **15**, 1679 – 1683 (2007).

[151] G. Fujii, N. Namekata, M. Motoya, S. Kurimura, and S. Inoue, "Bright narrowband source of photon pairs at optical telecommunication wavelengths using a type-II periodically poled lithium niobate waveguide," Opt. Express **15**, 12 769 – 12 776 (2007).

[152] K. Yoshino, T. Aoki, and A. Furusawa, "Generation of continuous-wave broadband entangled beams using periodically-poled lithium niobate waveguides," Appl. Phys. Lett. **90**, 041 111 (2007).

[153] D. Lee and T. G. III, "Entangled Photon Absorption in an Organic Porphyrin Dendrimer," J. Phys. Chem. B **110**, 25 582 25 585 (2006).

[154] T. Pittman, "Development of a Parametric Down-Conversion Source for Two-Photon Absorption Experiments," Proc. of SPIE **6710**, 67 100B (2007).

[155] A. Kalachev, D. Kalashnikov, A. Kalinkin, T. Mitrofanova, A. Shkalikov, and V. Samartsev, "Biphoton spectroscopy of YAG:Er3+ crystal," Laser Phys. Lett. **4**, 722 – 725 (2007).

[156] W. Akemann, C. D. Raj, and T. Knöpfel, "Functional Characterization of Permuted Enhanced Green Fluorescent Proteins Comprising Varying Linker Peptides," Photochem. and Photobiol. **74**, 356363 (2001).

[157] A. Jechow, V. Raab, and R. Menzel, "Tunable 6.8 W narrow bandwidth emission from a single-stripe continuous-wave broad-area laser diode in a simple external cavity," Appl. Opt. **47**, 1447 – 1450 (2008).

[158] A. Jechow and R. Menzel, "Efficient blue light generation by frequency doubling of a broad-area diode laser in a compact external cavity," Appl. Phys. B **89**, 507 – 511 (2007).

[159] A. Jechow, A. Heuer, and R. Menzel, "High brightness, tunable biphoton source at 976 nm for quantum spectroscopy," Opt. Express **16**, 13 439–13 449 (2008).

[160] A. Jechow, D. Skoczowsky, and R. Menzel, "Monolithic SHG Ring Resonator Passively Coupled to an External Cavity Enhanced Broad Area Laser Diode," in CLEO/QELS 2009 Conference Digest p. CThZ5 (2009).

[161] F. Zernike and J. E. Midwinter, *Applied Nonlinear Optics* (Wiley, New York, 1973).

Publications

Articles in peer reviewed Journals

J-01 A. Jechow, K. Paschke, G. Erbert and R. Menzel, "Blue-green light generation using high brilliance edge emitting diode lasers," Laser and Photonics Reviews, published online DOI: 10.1002/lpor.200900023

J-02 D. Skoczowsky, A. Jechow, R. Menzel, K. Paschke and G. Erbert, "Second harmonic generation using a semiconductor tapered amplifier in a coupled ring resonator geometry," Optics Letters, accepted for publication

J-03 A. Jechow, M. Lichtner, R. Menzel, M. Radziunas, D. Skoczowsky, A. G. Vladimirov "Stripe-array diode-laser in an off-axis external cavity: Theory and experiment," Optics Express 22, 19599-19604 (2009)

J-04 D. Skoczowsky, A. Jechow, H. Stürmer, T. Poßner, J. Sacher and R. Menzel, "Quasi monolithic ring resonator for efficient frequency doubling of an external cavity diode laser," Applied Physics B, published online DOI:10.1007/s00340-009-3802-7

J-05 A. Jechow, A. Heuer, and R. Menzel, "High brightness, tunable biphoton source at 976 nm for quantum spectroscopy," Optics Express 16, 13439-13449 (2008)

J-06 A. Jechow, V. Raab and R. Menzel, "Tunable 6.8 W narrow bandwidth emission from a single-stripe continuous-wave broad-area laser diode in a simple external cavity," Applied Optics 47, 1447-1450 (2008)

J-07 A. Jechow and R. Menzel, "Efficient blue light generation by frequency doubling of a broad-area diode laser in a compact external cavity," Applied Physics B 89, 507-511 (2007)

J-08 A. Jechow, M. Schedel, S. Stry, J. Sacher and R. Menzel, "Highly efficient single-pass frequency doubling of a continuous-wave distributed feedback laser diode using a PPLN waveguide crystal at 488 nm," Optics Letters 32, 3035-3037 (2007)

J-09 D. Skoczowsky, A. Heuer, A. Jechow and R. Menzel, "Generation of 25 ps pulses by self induced mode locking of a single broad area diode laser with 300mW average output power," Optics Communications 279, 341-345 (2007)

J-10 A. Jechow, V. Raab, R. Menzel, M. Cenkier, S. Stry and J. Sacher, "1 W tunable near diffraction limited light from a broad area laser diode in an external cavity with a line width of 1.7 MHz," Optics Communications 277, 161-165 (2007)

J-11 A. Jechow, D. Skoczowsky and R. Menzel, "100 mW high efficient single pass SHG at 488 nm of a single broad area laser diode with external cavity using a PPLN waveguide crystal," Optics Express 15, 6976-6981 (2007)

J-12 A. Jechow, V. Raab and R. Menzel, "Tunable diffraction-limited light at 488 nm by single-pass frequency doubling of a broad area diode laser," Applied Optics 46, 943-946 (2007)

J-13 A. Jechow, V. Raab and R. Menzel, "High cw power using an external cavity for spectral beam combining of diode laser-bar emission," Applied Optics 45, 3545 - 3547 (2006)

International Conferences

C-01 A. Jechow and R. Menzel, "Highly efficient visible light generation at 488 nm using high brilliance laser diodes and periodically poled materials," OSA topical meeting NLO, Honolulu, USA 16.07.2009

C-02 A. Jechow, A. Heuer and R. Menzel, "High brightness, tunable diode laser based continuous-wave biphoton source for two photon absorption at 976 nm," OSA topical meeting NLO, Honolulu, USA 14.07.2009

C-03 A. Jechow, A. Heuer and R. Menzel, "Tunable diode laser based biphoton source for quantum spectroscopy," CLEO Europe/ IQEC, Munich, 17.06.2009

C-04 D. Skoczowsky, A. Jechow and R. Menzel, "Quasi monolithic ring resonator for efficient SHG of 488 nm," CLEO Europe/ IQEC, Munich, 16.06.2009

C-05 A. Jechow, D. Skoczowsky and R. Menzel, "Monolithic SHG ring resonator passively coupled to an external cavity enhanced broad area laser diode," CLEO/QELS, Baltimore, USA, 04.06.2009

C-06 D. Skoczowsky, A. Jechow, H. Stürmer, T. Poßner, S. Stry, J. Sacher, and R. Menzel, "Monolithic ring resonator with PPLN crystal for efficient cw SHG of 976 nm emitted by a diode laser," Photonics West 2009, San José, USA, 28.01.2009

C-07 A. Jechow, S. McNeil, C. Kaleva, D. Skoczowsky and R. Menzel, "Highly efficient single-pass blue-light generation at 488 nm using a PPKTP waveguide crystal and high-brightness diode lasers," Photonics West 2009, San José, USA, 27.01.2009

C-08 A. Jechow, D. Skoczowsky, A. Heuer and R. Menzel, "High brilliance external cavity enhanced broad area laser for efficient frequency doubling," European Semiconductor Laser Workshop, Eindhoven, Netherlands, 19.09.2008

C-09 A. Jechow, A. Heuer and R. Menzel, "Highly efficient tunable blue light generation using an external cavity enhanced gain guided broad area laser diode," ISLC, Sorrento, Italy, 16.09.2008

C-10 A. Jechow, R. Menzel, "142 mW Tunable Blue Light Generation at 488 nm by Single-Pass SHG of an External Cavity Enhanced Broad-Area Laser Diode," CLEO/QELS, San José, USA, 05.05.2008

C-11 A. Jechow, A. Heuer, R. Menzel, "52%-efficient single-pass SHG in a PPLN waveguide by frequency doubling of a cw-DFB RW laser diode," CLEO/QELS, San José, USA, 05.05.2008

C-12 A. Jechow, A. Heuer, M. Kelemen, R. Menzel, "Highly efficient tunable blue light generation by SHG of an external cavity enhanced broad area laser diode using a PPLN waveguide," Photonics Europe, Strasbourg, France, 07.04.2008

C-13 A. Jechow, S. Stry, J. Sacher, R. Menzel, "Single pass SHG of a high power DFB RW laser with more than 50% conversion efficiency using a PPLN waveguide crystal," Photonics Europe, Strasbourg, France, 07.04.2008

C-14 A. Jechow, A. Heuer, D. Skoczowsky, R. Menzel, "Highly efficient blue light generation with high brightness semiconductor lasers," Laser Optics Berlin, 17.03.2008

C-15 A. Jechow, D. Skoczowsky, R. Menzel, S. Stry, J. Sacher, "159 mW blue light by single pass second harmonic generation with 52% conversion efficiency using a PPLN waveguide crystal and a cw DFB laser," Photonics West 2008, San José, USA, 24.01.2008

C-16 A. Jechow, D. Skoczowsky, R. Menzel, M. Kelemen, "Highly-efficient single pass SHG of an external cavity enhanced broad area laser diode using a PPLN waveguide crystal," Photonics West 2008, San José, USA, 21.01.2008

C-17 A. Jechow, D. Skoczowsky, A. Heuer and R. Menzel, "Highly efficient single pass second harmonic generation of a broad area laser diode in an external cavity using a PPLN waveguide crystal," CLEO Europe/ IQEC 2007, Munich, 21.06.2007

C-18 A. Jechow and R. Menzel, "23-mW tunable diffraction limited light at 488 nm by frequency doubling of a broad-area diode laser using PPLN," Photonics West 2007, San José, USA, 24.01.2007

C-19 V. Raab, A. Jechow, and R. Menzel "V-shaped external cavity for tunable 1 W diffraction limited cw-power at 976-nm," Photonics West 2006, San José, USA 24.01.2006

C-20 A. Jechow, V. Raab, R. Menzel "6.8 W cw-output power from a 976-nm external cavity diode laser with narrow linewidth and 40-nm tuning range," Photonics West 2006, San José, USA, 24.01.2006

C-21 V. Raab, A. Jechow, R. Menzel, M. Cenkier, S. Stry, J. Sacher, M. Kelemen, and M. Mikulla "High brightness high brilliance tunable broad area diode laser with 1 W of near diffraction limited light," IQEC/ CLEO Pacific Rim, Tokyo, 13.07.2005

C-22 V. Raab, A. Jechow, and R. Menzel, "Spectral beam combining of 25 diode lasers to get 10 W cw emission," IQEC/CLEO Pacific Rim, Tokyo, 12.07.2005

C-23 M. Cenkier, S. Stry, J. Sacher, A. Jechow, V. Raab and R. Menzel, "High brilliance phase coupled broad area diode lasers in a compact external cavity with longitudinal and spatial singlemode operation and 500 mW power," CLEO-Europe/EQEC, Munich, 14.06.2005

C-24 A. Jechow, V. Raab, R. Menzel, M. Cenkier, S. Stry, J. Sacher, M.T. Kelemen, and M. Mikulla, "Tunable cw-diode laser for 940 to 990 nm with over 700 mW of near-diffraction limited light," CLEO-Europe/EQEC, Munich, 14.06.2005

C-25 A. Jechow, V. Raab, R. Menzel, "10-W cw-emission with an $M^2 < 14$ from a lambda-multiplexed array of 25 broad area diode lasers," Photonics West 2005, San José, 27.01.2005

C-26 R. Menzel, V. Raab, A. Jechow, and D. Skoczowsky "High brightness laser diodes with external cavities," ICONO/LAT 2005, St. Petersburg, 11.05.2005

Acknowledgment

A comprehensive scientific investigation is barely the work of a single person. Thus, I have to thank several colleagues, family and friends for their support.

First of all, I have to thank my supervisor Prof. Dr. Ralf Menzel for his trust and for applying the right amount of pressure to keep me focused and leaving me the necessary freedom to develop my own ideas.

The department of photonics in Potsdam provided a friendly atmosphere, a great team and very good facilities for my research. I have to thank all group members, but I have to point out several individuals who contributed most to my work: I am grateful to Dr. Volker Raab, who introduced me to the field of laser physics during my diploma and master thesis. Without his passion I would not have chosen this path. In the same manner I have to thank Danilo Skoczowsky for his patience and reliability. We shared the lab and office and became a great team because we complement one another. Michael Seefeldt helped me with LaTeX and reviewed this text carefully. Axel Heuer is the "maid of all work" at our department but although he is busy all the time he doesn't know the word "no".

Furthermore, I have to thank several people for their cooperation: Marc Kelemen of *m2k Laser, Freiburg* for sharing a lot of knowledge about stripe-arrays and for allowing me to use their facilities for the experiments with the tapered amplifier, Joachim Sacher of *Sacher Lasertechnik, Marburg* for providing the DFB laser and the 40 mm bulk PPLN crystal, Karin Wu and Ming-Hsien Chou of *HCPhotonics, Taiwan* for keeping their promise of manufacturing an advanced PPLN waveguide crystal, Phil Battle and Shirley McNeil from *AdVR inc, Montana, USA* for providing the PPKTP waveguide crystal.

Additionally, I have to thank Mindaugas Radziunas, Mark Lichtner and the whole Laser-dynamics group at the *WIAS Berlin* for their cooperation and the help with the numerical simulations.

I thank all my friends and my band mates of *desilence* and *Dew Scented* for giving me a life besides physics and my mother in law for her excellent medical support.

I have to express endless gratitude to my family. My parents always supported me with love and deep understanding during my entire life. They never tried to slow down my curiosity.

My last words and therefore my biggest and deepest thank are reserved for my wife Konstanze. Her love and trust pushed me forward, she kept me grounded. Without her, I would not have come this far. I love you Konny!

Andreas Jechow
Potsdam, 03. September 2009

Erklärung

Hiermit versichere ich, dass ich die vorliegende Arbeit selbstständig und unter ausschließlicher Verwendung der angegebenen Quellen und Hilfsmittel verfasst habe. Die Arbeit wurde an keiner anderen Hochschule oder Universität eingereicht.

Potsdam 03. September 2009

Diode lasers are compact and efficient light sources but despite modern bad gap engineering not all wavelengths have been realized, yet. Thus, nonlinear frequency conversion is necessary to cover the huge range of applications that require coherent radiation in the visible spectral range.

In this work, stripe-array diode lasers have been studied comprehensively. Such a stripe-array consists of several narrow striped emitters with an emitting area comparable to a broad area diode laser. The aim was to achieve stable longitudinal and transversal single mode operation with high output powers giving a brightness sufficient for efficient nonlinear frequency conversion.

The physical effects that are the origin of the emission characteristics of the stripe array were investigated theoretically and experimentally. Numerical models could be verified and extended. Novel external cavity designs for the selection and stabilization of a specific array mode have been developed. Highly efficient second harmonic generation as well as the generation of biphotons by parametric down-conversion could be demonstrated.